Revista Brasileira de Ciências Mecânicas

Journal of the Brazilian Society of Mechanical Sciences

3

PUBLICAÇÃO DA ABCM - ASSOCIAÇÃO BRASILEIRA DE CIÊNCIAS MECÂNICAS

VOL. XIX - No.3 - SEPTEMBER 1997 ISSN 0100-7386

REVISTA BRASILEIRA DE CIÊNCIAS MECÂNICAS
JOURNAL OF THE BRAZILIAN SOCIETY OF MECHANICAL SCIENCES
Vol. 1, Nº 1 (1979)-
Rio de Janeiro: Associação Brasileira de Ciências Mecânicas
Trimestral
Inclui referências bibliográficas.
1. Mecânica
ISSN-0100-7386

A REVISTA BRASILEIRA DE CIÊNCIAS MECÂNICA publica trabalhos que cobrem os vários aspectos da ciência e da tecnologia em Engenharia Mecânica, incluindo interfaces com as Engenharias Civil, Elétrica, Química, Naval, Nuclear, Aeroespacial Alimentos, Agrícola, Petróleo, Materiais, etc., bem como aplicações da Física e da Matemática à Mecânica.

INDEXED by Applied Mechanics Reviews and Engineering Information, Inc..

Publicação da / Published by
ASSOCIAÇÃO BRASILEIRA DE CIÊNCIAS MECÂNICAS
THE BRAZILIAN SOCIETY OF MECHANICAL SCIENCES

Secretária da ABCM : **Ana Lúcia Fróes de Souza**
Avenida Rio Branco, 124 18º Andar
20040-001 Rio de Janeiro RJ
Tel.: (021) 221-0438/Fax: (021) 222-7128

Presidente: **Carlos Alberto de Almeida**
Vice-Presidente: **Arthur Palmeira Ripper Neto**
Secretário Geral: **Hans Ingo Weber**
Diretor de Patrimônio: **Felipe Bastos de F. Rachid**
Secretário: **Paulo Batista Gonçalves**

Secretária da RBCM: **Maria de Fátima Afonso de Souza**
UNICAMP - FEM - C.P. 6122
13083-970 Campinas SP
Tel.: (019) 239-8353/Fax: (019) 239-3722

JOURNAL OF THE BRAZILIAN SOCIETY OF MECHANICAL SCIENCES
REVISTA BRASILEIRA DE CIÊNCIAS MECÂNICAS

REVISTA FINANCIADA COM RECURSOS DO
Programa de Apoio a Publicações Científicas
MCT CNPq FINEP

RBCM - J. of the Braz. Soc. Mechanical Sciences
Vol. XIX - No.3 - 1997 - pp. 322-331

ISSN 0100-7386
Printed in Brazil

Two-Phase Flow Imaging by Electrical Capacitance Tomography: Numerical Simulation for Image Reconstruction Algorithm Development

Luiz Felipe Mendes de Moura
UNICAMP - Universidade Estadual de Campinas
Faculdade de Engenharia Mecânica
Departamento de Engenharia Técnica e de Fluídos
13083-970 Campinas, SP Brasil

Francisco Antonio Belo
Universidade Federal da Paraíba
Centro de Tecnologia
58059-900 João Pessoa, PB Brasil

Abstract

This paper describes a capacitance system for tomographic imaging of two-phase flows. Numerical simulations based on the finite element method provided the capacitance values between the electrode pairs for different spatial flow distribution. A linear back projection algorithm was used to reconstruct the cross section image of the two-phase flow from the capacitance values. Some reconstructed flow images (stratified, annular and droplets) obtained using this algorithm are presented and discussed. Further efforts are undertaken to improve the filtering technique applied to the back projection algorithm. Limitations and possible future improvements of this technique are discussed.

Keywords: *Two-Phase Flow, Tomography, Image Reconstruction Algorithm, Numerical Simulation.*

Introduction

The problem of determining the effective transport properties of multiphase systems has attracted the attention of many researchers. There are no exact analytical predictions of the effective properties of random multiphase systems for arbitrary phase properties and volume fractions, even for some simple problems (Kin and Torquato, 1990). Description of the interfacial structures and its time evolution, as well as the gradients which control the transfer of mass, momentum, and energy at these phase boundaries represent a challenge for the future of two-phase flow analysis. Light scattering, chemical, photographic, ultrasonic and electrical measurement methods have been proposed and/or used to investigate the interfacial area concentration. These methods are limited and answer only part of the problem. Measurement of the interfacial velocity itself is extremely difficult in most two-phase systems and has not been used for direct determination of the interfacial area concentration (Lin et al., 1991). The tomographic technique may be applied to multiphase flow in order to overcome the measurement limitations discussed above. Some industrial applications of this technique are discussed by Dickin et al. (1992), Huang et al. (1992) and McKee et al. (1993).

Tomography is normally known as a radiological technique for obtaining clear X-ray images of deep internal structures by focusing on a specific plane within a body. Barber et al. (1983) and Seager et al. (1987) presented a method to produce tomographic images using electrical resistivity, which might have applications in medical diagnosis. Research and development of electrical impedance computed tomography has been undertaken in geological area (Dynes and Litle, 1981), also by using an electrical resistivity technique. In the traditional computed tomographic technique, sensors are high energy X-rays with straight ray paths which are independent of the medium being examined. In contrast, the current paths and equipotential surfaces of the electrical impedance tomography are functions of an unknown impedance distribution (Yorkey et al., 1987).

Some studies applying tomography to the investigation of multiphase flows (MacCuaig et al., 1985) have used Gamma-rays to obtain three-dimensional density maps of laboratory scale fluidized beds. The X-ray computed tomography techniques have been applied to fluidized bed density imaging (Banholzer et al., 1987) and to multiphase flow (Vinegar and Wellington, 1986). Hussein and Meneley (1986) applied neutron tomography to two-phase flows. Plaskowski et al. (1987) described the application of

Manuscript received: November 1995. Technical Editor: Carlos Alberto Carrasco Altemani

the ultrasonic technique to multiphase flow imaging. Process engineering studies involving impedance tomography include capacitive transducers imaging of oil-gas flows (Huang et al., 1992), fluidized beds (Fasching and Smith Jr., 1991), and capacitive and resistive imaging of dense-phase pneumatic conveying (McKee et al., 1993). Geraets and Borst (1988) showed the advantage of the capacitive transducers over the resistive ones.

Two-phase flow impedance tomographic methods are actually sequential hardware processes, where all electrode pairs are scanned by only a single transducer. In a parallel tomography system (Belo, 1995), each electrode has its own intrinsically stray-immune capacitance transducer. Then, when an electrode is excited with the input signal, all other electrodes are ready for output signal measurements. This parallel system, associated with a high frequency transducer, allows faster data acquisition and better imaging resolution.

Different methods of image reconstruction for electrical impedance tomography systems have been proposed. Yorkey et al. (1987) examined some image reconstruction methods including the perturbation method used by Kim et al. (1983), the equipotential lines method used by Barber et al (1983) and the variational method developed by Kohn and Vogelius (1987). The main problem in image reconstruction is that the electrical field sensitivity distribution depends on the phase distribution. Actually, the most used image reconstruction method for capacitive tomography systems is the back projection algorithm described by Herman (1979). This method can be improved either by filtering (Huang et al., 1992) or by calibration (Fasching and Smith, 1991).

Figure 1 shows schematically the principal steps of the electrical capacitance tomography system and the back projection algorithm used for image reconstruction. The back projection algorithm is based on the solution of two problems, the forward problem and the inverse problem. The forward problem is based on the determination of the electrical field inside the tomography sensor as a function of the sensor geometry and the phase distribution. Usually the forward problem is solved by a finite element method to obtain the capacitance values between the different electrode pairs. By changing the phase distribution inside the sensor, the capacitance sensitivity distribution of the tomography system may be obtained. The inverse problem consists in the determination of the spatial phase distribution inside the tomography sensor, that is the flow image, from the capacitance measurements. Due to the limited number of capacitance measurements, the image may only be reconstructed by using some approximate method. In the back projection algorithm, the reconstructed image is obtained from the capacitance measurements and the capacitance sensitivity distribution.

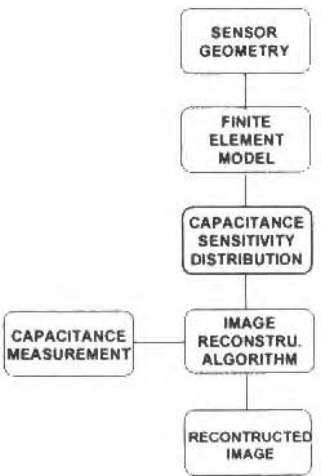

Fig. 1 Flow Chart of the Electrical Capacitance Tomography System

In this work the linear back projection algorithm is described. Some numerical simulations using the finite element method were performed to obtain the theoretical capacitance values, instead of the capacitance measurements, for different two-phase flow patterns. The two-phase flow images were then

reconstructed by using the linear back projection algorithm. The improvement of the image resolution was obtained through a filtering technique.

Finite Element Model

In this study the capacitance between different electrode pairs is obtained numerically by using a two-dimensional finite element model. The electrostatic field problem can be represented by the following Laplace's equation:

$$\nabla.\left[\varepsilon_0 \varepsilon(x,y)\nabla\phi(x,y)\right]=0 \tag{1}$$

where $\phi(x,y)$ and $\varepsilon(x,y)$ are, respectively, the two-dimensional electrostatic potential and the dielectric constant distributions and ε_0 is the free-space dielectric constant.

The boundary conditions imposed by the measurement technique, when the electrode i is the source electrode (i=1,n), are:

$$\psi_i=\begin{cases} V_c\ , & (x,y)\in\Gamma_i \\ 0\ , & (x,y)\notin\Gamma_i \end{cases} \tag{2}$$

where Γ_i represents the spatial locations of the n electrodes around the external surface of the sensor and V_c is the potential applied to the source electrode. Figure 2 shows a capacitance sensor with 8 electrodes around a glass pipe.

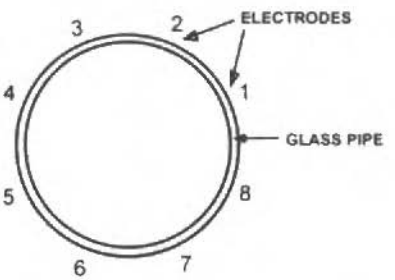

Fig. 2 Schematic Representation of an 8-Electrode Capacitive Sensor

As it was mentioned before the forward problem is based on the determination of the capacitance values for a known distribution of the dielectric constant, that is for a given distribution for the gas ($\varepsilon_g=1$) and the liquid ($\varepsilon_l=80$) components. For an 8-electrode sensor, there are 28 independent capacitance values for all possible combinations of electrode pairs. The first step in dealing with the problem is the solution of Eq. (1) in order to obtain the distribution of $\phi(x,y)$. Since the flow distribution is usually very irregular, there is no analytical solution to Eq. (1). Therefore a numerical method, like a finite element method, must be used.

In this work the commercial finite element computer code ANSYS was used to solve the electrical field inside the capacitance sensor. The region shown in Fig. 2 is divided into P (P=968) three-nodes triangular elements corresponding to Q (Q=529) nodes. The finite element mesh is shown in Fig. 3.

After solving node electric potentials, the capacitance between each electrode pair i-j can be determined by performing numerically the following integration:

$$C_{i,j}=\frac{\varepsilon_0}{V_c}\int_{(x,y)\in\Gamma_j}\varepsilon(x,y)\nabla\phi_i(x,y).d\Gamma_j \tag{3}$$

where $\varphi_i(x, y)$ is the two-dimensional electrostatic potential distribution when electrode i is the source electrode.

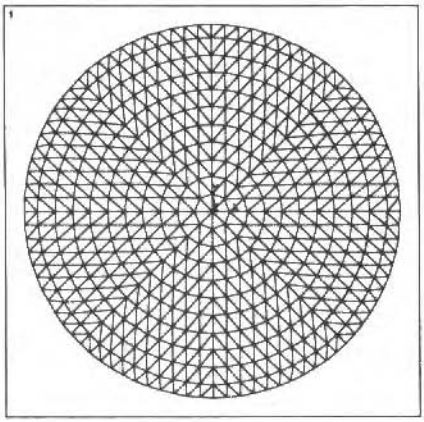

Fig. 3 Finite Element Mesh for the Capacitance Sensor

Capacitance Sensitivity Distribution

The finite element model previously described is used to calculate the capacitance sensitivity distribution needed for the image reconstruction algorithm (see Fig. 1). The input data required for the finite element calculations are presented in Table 1.

Table 1 Input Data for the Finite Element Calculations

Data	Description	Value
R1	Internal pipe radius	46.5 mm
R2	External pipe radius	50.0 mm
θ	Electrode angle	45°
ε_g	Gas dielectric constant	1
ε_l	Liquid dielectric constant	80
ε_p	Pipe dielectric constant	4

The capacitance sensitivity of the kth in-pipe element (a finite element inside the pipe) can be determined by assigning to this element the dielectric constant of the liquid and to all others in-pipe elements the dielectric constant of the gas. In the present model there are 800 in-pipe finite elements and 168 finite elements representing the pipe wall. The capacitance sensitivity distribution for the electrode pair i-j is defined as:

$$S_{i,j}(k) = \frac{\mu(k)\left[C_{i,j}(k) - C_{i,j}^{g}\right]}{C_{i,j}^{l} - C_{i,j}^{g}} \tag{4}$$

where $C_{i,j}(k)$ is the capacitance when the kth in-pipe element has the dielectric constant of the liquid and all others in-pipe elements have the dielectric constant of the gas, $C_{i,j}^{g}$ and $C_{i,j}^{s}$ are respectively the capacitance when the pipe is filled with gas and with liquid and $\mu(k)$ is the area correction factor related to the kth in-pipe element. The area correction factor is the kth element area divided by the mean element area (total area divided by the number of elements).

Due to the sensor symmetry, only four capacitance sensitivity distributions need to be calculated. They are $S_{1,2}$ (sensitivity distribution of an adjacent electrode pair), $S_{1,3}$ (that of an electrode pair separated by one electrode), $S_{1,4}$ (that of an electrode pair separated by two electrodes) and $S_{1,5}$ (that of a diagonally separated electrode pair). This can significantly reduce the computational time, since the other 24 sensitivity distributions can be obtained by a simple transformation (the centre of the pipe being the centre of rotation) of the type:

$$S_{m,n} = R\left(S_{i,j}; \gamma\right) \tag{5}$$

where $R(;)$ is an operator representing the aforementioned transformation. It other words $S_{m,n}$ can be obtained by rotating $S_{i,j}$ anticlockwise by γ degrees. Table 2 presents the capacitance sensitivities associated to Eq. (5).

Table 2 - List of the Other 24 Sensitivity Distributions as a Function of the 4 Typical Ones and the Corresponding Rotational Angle.

$S_{i,j}$	45^0	90^0	135^0	180^0	225^0	270^0	315^0
$S_{1,2}$	$S_{2,3}$	$S_{3,4}$	$S_{4,5}$	$S_{5,6}$	$S_{6,7}$	$S_{7,8}$	$S_{1,8}$
$S_{1,3}$	$S_{2,4}$	$S_{3,5}$	$S_{4,6}$	$S_{5,7}$	$S_{6,8}$	$S_{1,7}$	$S_{2,8}$
$S_{1,4}$	$S_{2,5}$	$S_{3,6}$	$S_{4,7}$	$S_{5,8}$	$S_{1,6}$	$S_{2,7}$	$S_{3,8}$
$S_{1,5}$	$S_{2,6}$	$S_{3,7}$	$S_{4,8}$				

The four typical sensitivities distributions $S_{1,2}$ to $S_{1,5}$ are shown in the Fig. 4. It can be observed that the capacitance sensitivity is higher near the pipe wall than in the middle of the pipe. In some areas the sensitivity exhibits positive response, whereas in others it is negative or zero.

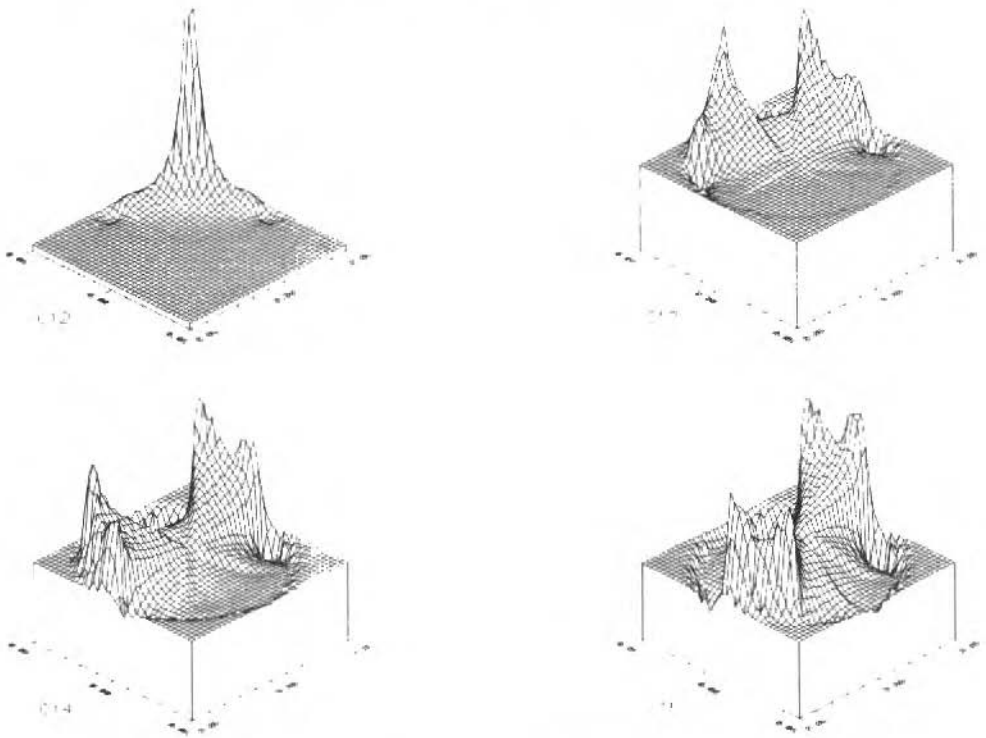

Fig. 4 Capacitance Sensitivity Distributions for the Four Typical Electrode Pairs

Simulation of the Capacitance Measurements

The finite element model is used to simulate various gas-liquid distributions in the capacitance sensor. The corresponding responses of the sensor, namely, the 28 capacitance data, are then determined to supply the flow data for the image reconstruction algorithm. Different flow regimes, such as stratified flow, annular flow, bubbly flow and droplet flow can be produced by assigning the corresponding values of the dielectric constant to each of the in-pipe elements. Flows of different liquid concentration (β), and different number and size of bubbles or droplets can be generated. Three flow distributions were studied in this work: stratified flow (β =0.50), annular flow (β =0.36) and droplet flow (β =0.08). Fig. 5 shows the corresponding 28 normalised capacitance, defined as:

$$\lambda_{i,j} = \frac{C^m_{i,j} - C^g_{i,j}}{C^l_{i,j} - C^g_{i,j}} \tag{6}$$

where $C^m_{i,j}$ is the capacitance measurement for the gas-liquid distribution.

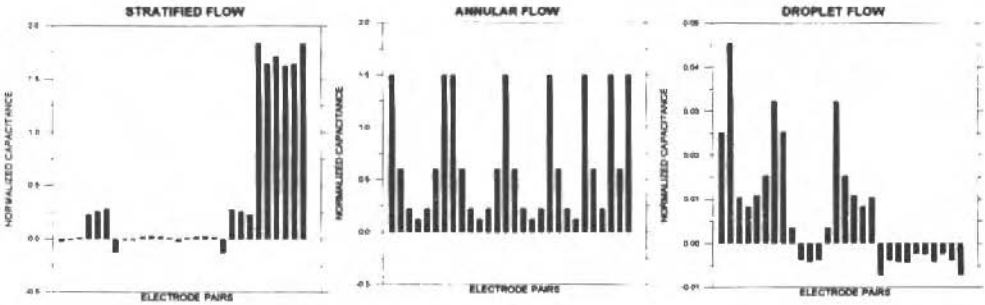

Fig. 5 Normalized Capacitance Data for Different Flow Regimes

For a linear system (for example, X-ray tomography) the normalised data should fall within the interval [0,1]. But for a non-linear system values of $\lambda_{i,j}$ either negative (under-shooting) or greater than one (over-shooting) could occur. The magnitude of the over-shooting is, in general, larger than that of the under-shooting. This non-linearity in the capacitance data is due to the effects of the distribution of the dielectric constant. The presence of the pipe wall and the gas-liquid mixture will redistribute the electric flux lines in the sensor. This redistribution may cause some electrodes to absorb more (or less) electric flux lines compared to the case where the pipe is filled with liquid (or gas), resulting in over-shooting (or under-shooting) effects.

Image Reconstruction Algorithm

As it is shown in Fig. 1, the two-phase imaging system is based on the image reconstruction algorithm. A reconstructed flow image is obtained from the capacitance measurements, by using the capacitance sensitivity distribution. The inverse problem is to determine the distribution of the dielectric constants of the gas-liquid mixture from the measured capacitance values, that is, to find the inverse of Eq. (3). It should be pointed out that there is no analytical solution to such an inverse problem.

To solve the inverse problem for capacitance tomography, some approximate methods are needed. Note that the number of unknown parameters in the system (the 800 image pixels) is greater than the number of known parameters (the 28 capacitance measurements). Thus the system is underdetermined. Some *prior* knowledge of the system, such as the capacitance sensitivity distribution, should be supplied to solve the problem.

An image reconstruction algorithm based on a simple back projection method was used for the capacitance tomography (Xie et al., 1989). The reconstructed image may be represented by pixel gray-

level used to approximate the dielectric constant distribution. The gray-level is determined from the following equations:

$$G(k) = W(k) \sum_{i=1}^{N-1} \sum_{j=i+1}^{N} \lambda_{ij} S_{ij}(k) \tag{7}$$

where

$$W(k) = \left(\sum_{i=1}^{N-1} \sum_{j=i+1}^{N} S_{ij}(k) \right)^{-1} \tag{8}$$

Note that $W(k)$ is the weighting factor used to compensate for the effects of non-uniform sensitivity distribution on the values of pixel gray level. The plot of $W(k)$ for the proposed capacitance sensor is shown in Fig. 6.

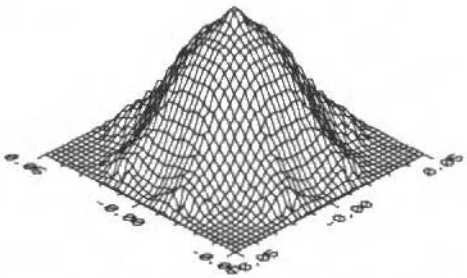

Fig. 6 Distribution of the Weighting Factors for Pixels

For a linear system, the image gray-level should fall within the interval $0 \le G(k) \le 1$. Since a capacitance tomography system exhibits non-linearity, both λ_{ij} and $G(k)$ may show overshooting (larger than 1) or undershooting (smaller than 0) values. The images reconstructed by the back projection method are always dominated by artifacts arising from elements of low gray levels. Therefore, some processing on $G(k)$ is needed before the gray-level image is displayed. Overshooting in $G(k)$ is eliminated by using the following truncation operation in Eq. (7):

$$\lambda_{ij} = 1 \quad \text{if} \quad \lambda_{ij} > 1 \tag{9}$$

A threshold operation is used to eliminate undershooting. It has been observed that the level of thresholding depend upon the flow (dielectric constant) distribution and the liquid concentration. To establish a suitable threshold level some knowledge of the flow pattern should be introduced, such as the liquid concentration, ρ_m, obtained from the capacitance measurements. A procedure for controlling the degree of thresholding on the basis of the estimated β_m is described below.

As the system is designed to reconstruct only a two-component flow image, the grey levels after thresholding $G_t(k)$ have only two values, say 0 and 1, thus:

$$G_t(k) = \begin{cases} 0 & \text{if } G(k) < t \\ 1 & \text{if } G(k) \ge t \end{cases} \tag{10}$$

where $(0 \le t \le 1)$ is the threshold level.

The concentration β_t estimated from the post-thresholding pixel elements $G_t(k)$ is given by:

$$\beta_t = \frac{1}{m}\sum_{k=1}^{m} G_t(k) \qquad (11)$$

where $m=800$ is the number of pixel elements.

When the absolute value of the difference between the concentration estimated from the capacitance measurements β_m and the post-thresholding estimate β_t is smaller than a chosen small value the thresholding procedure is completed.

To illustrate the effectiveness of this algorithm, Fig. 7c shows the reconstructed image of a stratified flow (β=0.50) using the normalized capacitance data shown in Fig. 5 and a threshold level t=0.07. The reconstructed image with filtering resembles closely the flow model shown in Fig. 7a. The image reconstructed without the threshold operation is presented in Fig. 7b, showing poor fidelity in comparison with Fig. 7c.

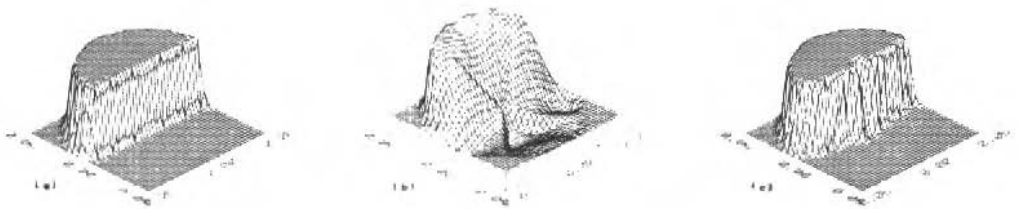

Fig. 7 Image Reconstruction of Stratified Flow. (a) Finite Element Flow Phantom, (b) Reconstructed Flow Without Filtering, (c) Reconstructed Flow With Threshold Filtering (t=0.07)

Figure 8c shows the reconstructed image of an annular flow (β =0.36) using the normalised capacitance data shown in Fig. 5 and a threshold level t=0.85. Again, the reconstructed image with filtering resembles closely the flow model shown in Fig. 8a. The image reconstructed without the threshold operation is shown in Fig. 8b. It should be noted the poor fidelity of this image in comparison with Fig. 8c.

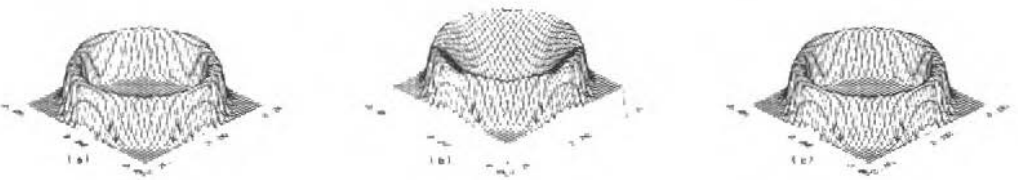

Fig. 8 Image Reconstruction of Annular Flow. (a) Finite Element Flow Phantom, (b) Reconstructed Flow Without Filtering, (c) Reconstructed Flow With Threshold Filtering (t=0.85)

Figure 9c shows the reconstructed image of a droplet flow (β =0.08) using the normalised capacitance data shown in Fig. 5 and a threshold level t=0.035. The reconstructed image without filtering (shown in Fig. 9b) is dominated by low gray-level artifacts. After threshold filtering, the reconstructed image is shown in Fig. 9c. In this case, even though the liquid concentration is correct, the droplets distribution in the reconstructed image are not predicted accurately. This distortion may be explained by the non-uniform sensitivity distribution inside the sensor. The region rear the wall has a higher sensitivity then a region in the centre of the sensor. Then, in the reconstructed image, the droplets have their position shifted toward the wall.

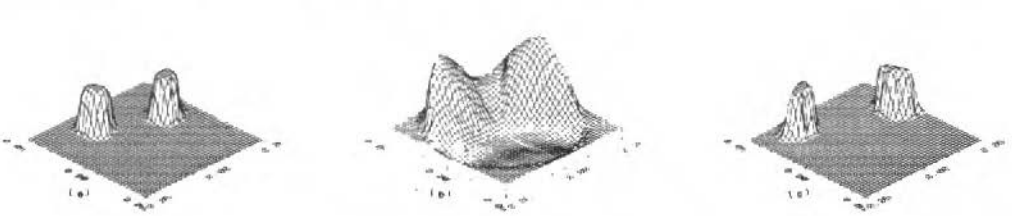

Fig. 9 Image Reconstruction of Droplet Flow. (a) Finite Element Flow Phantom, (b) Reconstructed Flow Without Filtering, (c) Reconstructed Flow With Threshold Filtering (t=0.035)

Conclusion

A useful image reconstruction method for two-phase flow capacitance tomography systems has been developed. This method is based on the fact that the phase distribution, or the dielectric constant distribution, may be approximated within the sensor by using only boundary capacitance measurements. The finite element method was used to solve the forward or direct problem. Using a sufficient large number of elements (968 in the present case), the numerical solution of the electrical potential field converges to the exact solution. The inverse problem was solved using a linear back projection algorithm. The poor spatial resolution of this method may be attributed to both the non-linear relationship between the capacitance and the dielectric constant and the limited number of independent capacitance measurements. The proposed threshold filtering technique should improve the image reconstruction results. A great computational effort was necessary for the solution of the forward problem and the sensitivity distribution determination. Once this function is known for a given sensor geometry and fluid dielectric properties, the computational effort needed to reconstruct the flow image is sufficiently reduced so that an on-line monitoring of the two-phase flow distribution might be possible.

References

Barber, D. C., Brown, B. H., and Freeston, I. L., 1983, "Imaging Spatial Distributions of Resistivity Using Applied Potential Tomography", Elec. Lett., Vol. 19, pp. 933-935.

Banholzer, W. F., Spiro, C. L., Kosky, P. G., and Maylotte, D. H., 1987, "Direct Imaging of Time-Averaged Flow Patterns in a Fluidized Reactor Using X-Ray Computed Tomography", Ind. Eng. Chem. Res., Vol. 26, pp. 763-767.

Belo, F. A., 1995, "Application of Electronic Analysis to the Study of Multiphase Flow" (in Portuguese), PhD Thesis - Faculdade de Engenharia Mecânica, Universidade Estadual de Campinas, Brasil

Dickin, F. J., Hoyle, B. S., Hunt, A., Huang, S. M., Ilyas, O., Lenn, C., Waterfall, R. C., Williams, R. A., Xie, C. G., and Beck, M.S., 1992, "Tomographic Imaging of Industrial Process Equipment: Techniques and Application", IEE Proceeding-G, Vol. 139, No. 1, pp. 72-82.

Dynes, K. A., and Litle, R. J., 1981, "Analysis of Electrical Conductivity Imaging", Geophysics, Vol. 46, pp. 1025-1036,.

Fasching, G. E., and Smith Jr., N. S., 1991, "A capacitive System for Three-Dimensional Imaging of Fluidized Beds, Rev. Sci. Instrum., Vol. 62, No. 9

Geraets, J. J. M., and Borst, J. C., 1988, "A Capacitance Sensor for Two-Phase Void Fraction Measurement and Flow Pattern Identification", Int. J. Multiphase Flow, Vol. 14, No. 3, pp. 305-320.

Herman, G. T. (ed.), 1979, "Image Reconstruction from Projections: Implementation and Applications", Topics in Applied Physics, Vol. 32, Berlin Springer.

Huang, S. M., Xie, C. G., Salkeld, J. A., Plaskowski, A., Thorn, R., Williams, R. A., Hunt, A., and Beck, M. S., 1992, "Process Tomography for Identification, Design and Measurement in Industrial Systems, Powder Technology, Vol. 69, pp. 85 -92.

Hussein, E. M. A., and Meneley, D. A., 1986, "Single Exposure Neutron Tomography of Two-Phase Flow", Int. J. Multiphase Flow, Vol. 12, pp. 1-34.

Kim, Y., Webster, J. G., and Tompkins, W. J., 1983, "Electrical Impedance Imaging of Thorax, J. Microwave Power", Vol. 18, pp. 245-257.

Kin, I. C., and Torquato, S., 1990, "Determination of the Effective Conductivity of Heterogeneous Media by Brownian Simulation", J. Appl. Phys., Vol. 68, No. 8.

Kohn, R. V. and Vogelius, M., 1987, "Relaxation of a Variational Method for Impedance Computed Tomography", Comm. Pure Appl. Math., Vol. 40, pp. 745-777.

Lin, J. T., Ovacik, L., Jones, O. C., Newell, J. C., Cheney, M., and Suzuki, H., 1991, "Use of Electrical Impedance Imaging in Two-Phase, Gas-Liquid Flows", ANS National Heat Transfer Conference, USA.

MacCuaig, N, Seville, J. P. K., Gilboy, W. B., and Clift, R., Appl. Opt., Vol. 24, p. 4083, 1985.

McKee, S. L., Williams, R. A., Dyakowski, T., and Bell, T. A., 1993, "Industrial Application of Electrical Tomography to Conveying Processes", Trans. Inst. Chem. Eng., Vol. 71.

Plaskowski, K., Beck, M.S., and Krawaczynski, J. S., 1987, "Flow Imaging for Multi-Component Flow Measurement", Trans. Inst. Meas. Control, Vol. 9, No. 2, pp. 108-112.

Seagar, A. D., Barber, D. C., and Brown, B. H., 1987, "Electrical Impedance Imaging", IEE Proc. 134, Pt. A, No. 2, pp. 201-210.

Vinegar, H. J., and Wellington, S. L., 1986, "Tomographic Imaging of Three-Phase Flow Experiments", Rev. Sci. Instrum., Vol. 58, pp. 96-107.

Xie, C. G., Plaskowski, A., and Beck, M. S., 1989, "8-Electrode Capacitance System for two-Component Flow Identification. Part 1: Tomographic Flow Imaging", IEE Proceedings-G, Vol. 136, No. 4, pp. 173-183.

Yorkey, T J., Webster, J. G., and Tompkins, W. J., 1987, "Comparing Reconstruction Algorithms for Electrical Impedance Tomography", IEEE Transactions on Biomedical Engineering, Vol. BME-34, No. 1, pp. 843-852.

RBCM - J. of the Braz. Soc. Mechanical Sciences
Vol. XIX - No.3 - 1997 - pp. 332-340

ISSN 0100-7386
Printed in Brazil

A Numerical Model for Thin Airfoils in Unsteady Motion

Paulo Afonso de Oliveira Soviero
Luis G.M. Lavagna
ITA - Instituto Tecnológico de Aeronáutica
12228-900 São José dos Campos, SP Brasil

Abstract

A numerical model based on normal dipole panels with constant strength distributions is proposed in order to solve the linearized unsteady motion of the thin airfoil in incompressible inviscid flow. The direct relationship between vortices and normal dipole panels with constant strength distributions is employed, with the specific aim of simplifying the numerical implementation of circulation conservation, force calculation and vortex shedding. The suggested method is fast and general. Classical unsteady thin airfoil problems are solved by the present model and the results are shown to compare well with analytical results.
***Keywords**. Thin Airfoils, Unsteady Flow, Normal Dipole Panels.*

Introduction

Notwithstanding the relative simplicity of the unsteady motion of a thin airfoil in incompressible inviscid flows, a large amount of work has been done since the early classical studies carried by Theodorsen (1935), von Kármán (1938), Küssner, Sears and Wagner (Bisplinghoff, Ashley, Halfman, 1955). Extentions of these classical analytical studies are intensively employed nowadays in engineering calculations, as cited in McCune, Lam and Scott (1990), where Wagner's integral equation is modified in order to allow for large amplitude airfoil motion, wake deformation and roll-up.

Basically the classical works can be classified into four admittance functions as follows (Yates Jr., 1985): Theodorsen function, C(k), for an airfoil oscillating in an uniform freestream, where k is the reduced frequency parameter; Sears function for a stationary airfoil in an oscillating gust field; Wagner function, $\Phi(s)$, for step changes in angle of attack or forward speed, and Küssner function, $\Psi(s)$, for an airfoil penetrating a sharp-edge gust. In the last two cases, the symbol s stands for distance in semichords traveled by the airfoil after the step change in angle of attack or gust entrance. In fact, Wagner's and Theodorsen's functions, just as Sears' and Küssner's functions, are related by means of Laplace transformations (Garrick, 1957).

Nomenclature

c	= airfoil chord	U_∞	= undisturbed flow velocity	$\delta\phi$	= velocity potential difference
C(k)	= Theodorsen function	X,Y,Z	= cartesian coordinates	Σ	= bound vortex intensity
f	= nondimensional aerodynamic force	Z_a	= transversal displacement of the chordline	$\Phi(s)$	= Wagner function
j	= unitary vector along Y	*	= vector product	ϕ	= perturbation velocity potential
k	= reduced frequency $\omega\, c / (2\, U_\infty)$	Γ	= vortex intensity	Ψ	= Küssner function
n	= unitary vector normal to the airfoil	Δt	= time step	ω	= angular frequency of harmonic oscillation
s	= distance in semichords	ΔX	= panel lenght	j	= panel number
t	= time	δC_p	= pressure coefficient difference	m	= time step
U_t	= total velocity				

The effect of the thickness of airfoils in small-amplitude, simple harmonic motion has been studied by Van De Vooren and Van De Vel (1964) using airfoil circle conformal mapping techniques. It is well known that for both steady and unsteady flows, the thickness will increase the lift coefficient of airfoils while viscosity, on the contrary, will decrease it. This fact, although fortuitous, justifies at least in part the study of thin airfoils. In the sixties, Giesing (1968) solves the problem of the unsteady airfoil in

Manuscript received: August 1996. Technical Editor: Carlos Alberto Carrasco Altemani

nonlinear potential flow by the very general panel method of Hess and Smith (1966). In the work of Giesing, the so called nonlinear effects are due to airfoil thickness, amplitude of motion, frequency of oscillation, gust magnitude and wake deformation. It should be stressed, however, that, strictly speaking, the only nonlinearity in the problem arises from the wake, that is, to find the wake shape involves a nonlinear process. The nonlinear effect relative to airfoil thickness comes indeed from boundary conditions.

Aside nonlinear effects, it is argued by Basu and Hancock (1978) that two Kutta conditions are required in order to obtain a satisfactory solution of the problem in hand. However, for general unsteady motions it is possible to obtain numerical solutions by imposing either the condition of finite velocities about the trailing edge or the condition of zero loading about the trailing edge. The main difference between Giesing and Basu and Hancock solutions for the Wagner problem is the fact that the former does not satisfy the zero loading condition (Basu, Hancock, 1978)). It is worth to point out that the two Kutta conditions referred above are satisfied by cusped trailing edge profile problems with nonlinear boundary conditions or thin airfoils in unsteady flow. Since the amplitude of motion for airfoils are realistically bounded by stall phenomena and nonlinearities due to profile thickness and wake shape are limited and well behaved in nature (Giesing, 1968), (Katz, Weihs, 1978b, 1981), at least for a single element airfoil (Rokhsaz, Selberg, Eversman, 1991), a numerical tackling of thin airfoil in unsteady motion becomes interesting due to its high versatility in dealing with many kinds of unsteady boundary conditions and low computational cost.

The main objective of the present work is to propose a simple and efficient numerical method to handle the problem of a thin airfoil in arbitrary motion. Additionally, the modeling may also be applied to airfoils with chordwise flexibility or compliant mean camber line. The basic limitation of the proposed procedure is the two-dimensional potential linearized theory; on the other hand, only fundamental concepts of fluid mechanics like free and bound vortices are employed. The direct relationship between vortices and normal dipole panels with constant strength distributions is emphasized and is the base of the suggested numerical model. Lift force, pitch moment and the leading edge suction force are obtained, from aerodynamic basic principles. The method can be applied in a straightforward manner to oscillating-wing propulsion studies as it is established in De Laurier and Winfield (1990) and, with minors reference frame modifications, as done in Katz and Plotkin (1991), regarding free vortex wake shape, boundary conditions and Bernoulli equation, to foils in a large amplitude curved path (Katz, Weihs, 1978a).

Analysis

Mathematical Model

Consider a two-dimensional thin airfoil moving along the negative X-axis in an incompressible inviscid fluid. Pitching and heaving motion, as well as chordwise flexibility or a compliant mean camber line can cause displacements of points on the airfoil from its average trajectory. The undisturbed flow velocity and reference length (airfoil chord) are made unitary and an arbitrary perturbation velocity, compatible with the linearization hypothesis, may be superimposed on the undisturbed flow in order to simulate gust profiles. For an irrotational flow the nondimensional perturbation velocity potential, ϕ, is described by the following system of equations,

$$\frac{\partial^2 \phi}{\partial X^2} + \frac{\partial^2 \phi}{\partial Z^2} = 0 \tag{1}$$

$$\frac{\partial \phi}{\partial Z} = \frac{\partial Z_a}{\partial t} + \frac{\partial Z_a}{\partial X} \qquad 0 \le X \le 1 \tag{2a}$$

$$\nabla \phi \to 0 \ as \ |X|, |Z| \to \infty \tag{2b}$$

where Za represents the instantaneous small transversal displacement of the chordline, and the Z-axis points upwards; the chordline spans over the X-axis from 0 to 1. Equation (1) expresses mass conservation. Overlooking any possibility of lag in the adjustment of the flow at the trailing edge, X=1, the Kutta hypothesis of finite, continuous velocities and pressure is applied (Bisplinghoff, Ashley, Halfman, 1955), (Katz, Weihs, 1981). Having solved Eq. (1) for ϕ, the pressure coefficient jump, δCp, on airfoil and wake is obtained with the help of the linearized Bernoulli equation,

$$\delta C_p = -2\left[\frac{\partial \delta\phi}{\partial X} + \frac{\partial \delta\phi}{\partial t}\right] \tag{3}$$

where $\delta\phi$ stands for the velocity potential difference between upper and lower sides. To assure pressure continuity over trailing edge and wake Eq. (3) is written as:

$$\frac{D\delta\phi}{Dt} = \frac{\partial \delta\phi}{\partial X} + \frac{\partial \delta\phi}{\partial t} = 0 \tag{4}$$

where D/Dt denotes the substantial derivative. Equation (4) guarantees that $\delta\phi$ at every point in the wake remains constant if displaced with the undisturbed flow velocity. This property, in fact a linearized version of Kelvin's theorem, will be employed in the proposed numerical model in order to assure Kutta and free wake conditions in the limits of linearized theory.

Numerical Model

The numerical model here proposed is somewhat similar to but not the same as the "marching-vortex" concept. It is taken into account three concepts well-known from the aerodymamicists; first the impulsive generation of vortices in perfect fluid; second the relationship between a vortex pair and the potential jump along the line that joins them and third the numerical solution of a thin airfoil by normal dipole panel singularity. The first two concepts are presented and discussed in von Kármán and Burgers (1976). The last one the reader can find it in Katz and Plotkin (19991). The motion begins from an impulsive start with the subsequent generation of a vortex wake modeled by a sequence of discrete vortices shed at equal time intervals. In this work the wake is convected downstream with free flow velocity, however, a nonlinear wake shape may be obtained by calculating the velocity on each free vortex. The steady state motion, if it exists, is obtained asymptotically. The sequence of events of the numerical procedure is summarized in Fig. 1 and its steps are described below.

At time t=0 the airfoil chord is divided in a convenient number of small and equally spaced panels, three in Fig. 1. Over each panel an unknown constant strength normal dipole distribution is assumed. At $t=0^+$, on each panel central point, the boundary conditions are exactly satisfied by a classical panel method solution of the Neumann problem. This impulsive motion produces a constant strength normal dipole distribution, $\delta\phi^0_j$, where subscript and superscript indicate the panel number and initial time step respectively. Due to the equivalence between a constant strength normal dipole panel and a counter rotating vortex pair placed at its edges, whose intensities are $\delta\phi^0_j$ $\Gamma^0_j = \pm\,\delta\phi^0_j$, the constant strength normal dipole distribution of each panel can be transformed into bound vortices. For the leading and trailing edges, $\Sigma^0_1=\Gamma^0_1$ and $\Sigma^0_4= -\Gamma^0_3$ respectively, while for inner adjacent panel edges the bound vortices intensities are $\Sigma^0_j =\Gamma^0_j - \Gamma^0_{j-1}$. During the elapsed time interval Δt , the trailing edge bound vortex becomes free and is shed with undisturbed flow velocity. At the next time $t=\Delta t^+$ a new constant strength normal dipole distribution is superimposed over the discretized airfoil in order to enforce again boundary conditions. After replacement of the normal dipole panels by their equivalent counter rotating vortex pairs, the bounded leading and trailing edges vortices are, now for the time step 1, $\Sigma^1_1 = \Sigma^0_1 + \Gamma^1_1$ and $\Sigma^1_4 = -\Gamma^1_3$ respectively, while for the inner adjacent panel edges the bound vortices intensities will be $\Sigma^1_j = \Sigma^0_j + (\Gamma^1_j - \Gamma^1_{j-1})$. The newly created vortex at the trailing edge is shed, during time interval Δt, as was the older one. This procedure generates a free wake in the form of a row of adjacent discrete vortices.

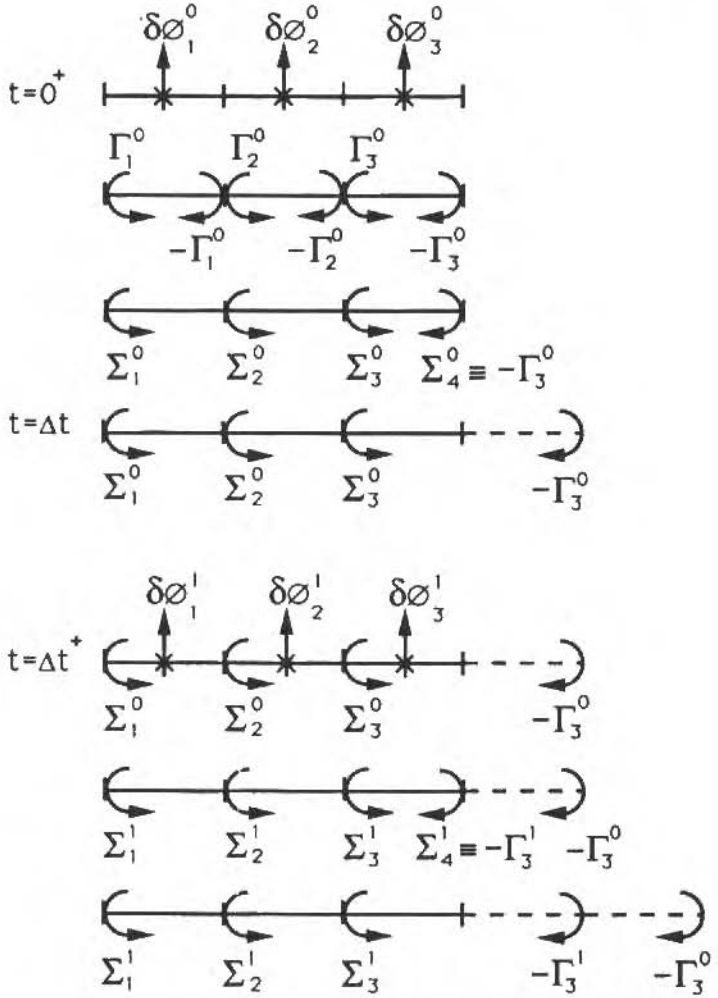

Fig. 1 Numerical Model - Sequence of Events

The numerical scheme is generalized for a time step m and chord discretization of n panels as:

$$\sum_{j}^{m} = \Sigma_{j}^{m-1} + \Gamma_{j}^{m} \tag{5a}$$

$$\sum_{n+1}^{m} = -\Gamma_{n}^{m} \tag{5b}$$

$$\sum_{j}^{m} = \Sigma_{j}^{m-1} + \left(\Gamma_{j}^{m} - \Gamma_{j-1}^{m}\right) \tag{5c}$$

for leading edge, trailing edge and inner adjacent panels, respectively. It should be noted that Kelvin's theorem is automatically satisfied by the above described numerical scheme. This is so because after each time step the boundary conditions are again satisfied, through the panel method solution, by constant strength dipole panels which are transformed in counter rotating vortex pairs. Thus, the global velocity circulation around airfoil and wake remains constant and equal to zero.

To obtain the force on the airfoil at time step m the total velocity, $\mathbf{U}_t$, is cala lated at each panel edge, except for the trailing edge. Taking into account all bound vortices at each panel edge, Σ^m_k, with direction perpendicular to the two-dimensional flow plane the nondimensional force, $\mathbf{f}^m_k$, at the k panel and m time step is expressed as:

$$\mathbf{f}_k^m = 2\mathbf{U}_t * \sum_k^m j + 2\frac{\partial}{\partial t}\left(\delta\phi\right)_k^m \Delta Xn \qquad (6)$$

In Equation (6) **j** is a unit vector along Y, **n** is a unit vector normal to the airfoil camberline, symbol * denotes vector product and ΔX is the panel length. Summing up all panel forces, the lift and suction force coefficients may be calculated by usual force decomposition, that is, normal to the undisturbed flow and parallel to the profile chord respectively. The first term on the right hand side of Eq. (6) is a numerical version of the Kutta-Joukowski theorem, whose demonstration, as it is applied in the present work, is discussed in von Kármán and Burgers (1976). The second term comes from unsteadiness and is evaluated at each panel central point. Care must be exercised in order to proper evaluate pitching moment, since the first force on the right hand side of Eq. (6) has as its application point the panel edge whereas the second one is applied at panel's center point. Further in order to account for the fact that bound vortices lie at the panel's first quarter point, a proper shifting of the pitching moment axis must be made. The new position is $\Delta X/4$ to the left.

In what concerns the suction force coefficient two remarks should be made. First, in spite of the fact that each panel gets subjected to an elementary suction force, the sum of all these elementary forces has the leading edge as its point of application. Secondly, it can be observed that, within the limits of linearized theory, the leading edge suction is of the "flat plate" type, since this force may be obtained from the coefficient of the first term in a bound vorticity Fourier series development as proposed by Glauert (Schlichting, Trukenbrodt, 1979).

Comparison with Exact Solutions

Numerical solutions to the four classical problems (as referred in the Introduction) are now compared to analytical results. Since mathematical modeling and boundary conditions are the same for both methods, eventual disagreements can be attributed to the singularity distribution or chord and time discretization. In the present numerical calculations, panel singularity distributions, time integration and derivatives are all of first order. Concerning chord and time discretization it is pointed out that they are not completely free, as for gust problems for example, where airfoil chord must be suitably discretized. The same point of view is extended to time discretization, that is, since the undisturbed flow velocity and chord discretization define a reference minimum time step for transient problems, $\Delta t = \Delta X/U_\infty$, then, from linearity and for unitary undisturbed flow velocity time step, Δt should be equal to ΔX. However, for some problems, small variations in time step were made in order to obtain better results. It has been also observed that the second term on the right hand side of Eq. (6) is very sensitive to the value of the time step, in transient problems.

As a first example the time history of the circulatory lift, suction and drag forces for a flat plate starting impulsively from rest at small angle of attack are compared in Figs. 2 and 3 with their respective analytical counterparts. Calculations with coarse and fine chord discretizations, five and twenty one equal panel elements respectively, are shown. A time step of $\Delta t = 1.2\ \Delta X$ has been employed, resulting in better agreement with analytical data than for time $\Delta t = \Delta X$, specially for the fine discretization. The time step influence is more pronounced at the beginning of the motion. The nondimensional lift curve shown in Fig. 2 is in fact Wagner's function, $\Phi(s)$, while the drag curve in Fig. 3 is obtained analytically by $\Phi(s) - \Phi^2(s)$ as reported in Garrick (1957). Nevertheless, from a numerical point of view, the three forces referred above result from calculations employing Eq. (6), and conveniently decomposed afterwards.

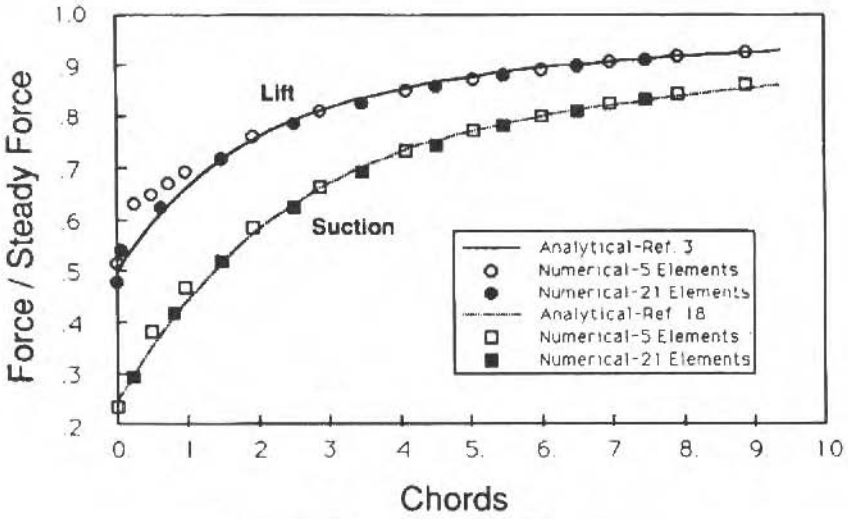

Fig. 2 Wagner's function and suction force coefficient
$\Delta t = 1.2\,\Delta X$

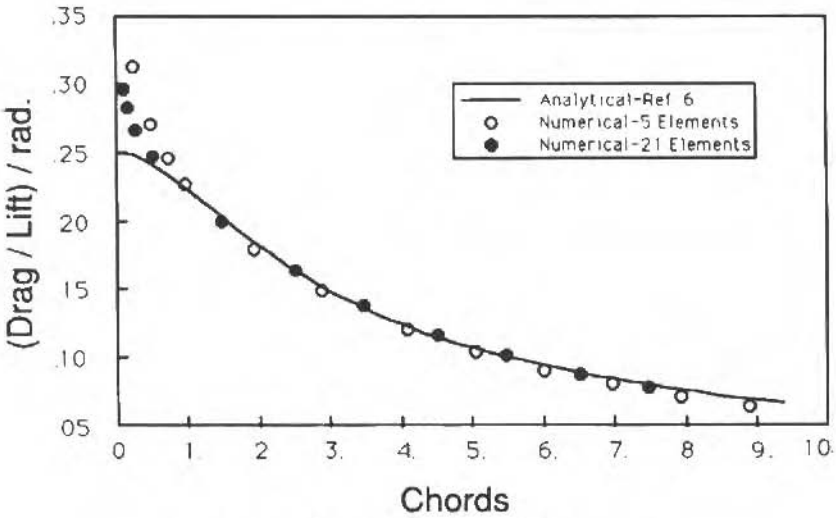

Fig. 3 Drag Coefficient for Wagner's Problem
$\Delta t = 1.2\,\Delta X$

The flat plate lift after penetration into a normal sharp gust is presented in Fig. 4, again for coarse and fine discretizations. As can be seen, the agreement with Küssner's function, $\Psi(s)$, is good, even for a chord discretization of five elements. However, the two solutions deviate when the gust front is passing by the trailing edge. This anomalous behavior is also present in the numerical solutions of Giesing (1968) and Basu and Hancock (1978). Nevertheless, for the fine discretization Küssner's function overshoot is negligible small. Unlike Wagner's problem, in the present calculations the gust front proceeds gradually from a control point to another at each time step increment, and is in agreement with theoretical results starting at the first instant of time.

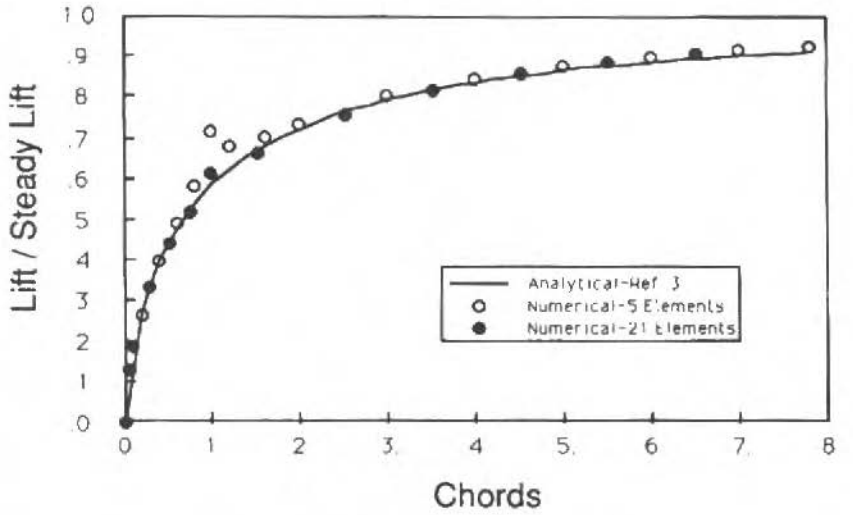

Fig. 4 Küssner's Function $\Delta t = \Delta X$

The flat plate lift for a sinusoidal gust (the Sears' problem), with amplitude 0.2 times the undisturbed flow velocity is presented in Fig. 5. Except at the beginning of run, where the free vortex wake is finite, numerical results are quite good (for fine discretization and after a displacement of one chord length). It should be remaided that in the analytical model the vortex wake is infinite in length. The periodic boundary conditions introduce another reference of time related to the wave length of the periodic gust. In the present work, for $k = 0.5$, the referred wave length is greater than the chord allowing one to use a time step $\Delta t = \Delta X$. Small variations of Δt do not affect the results significantly.

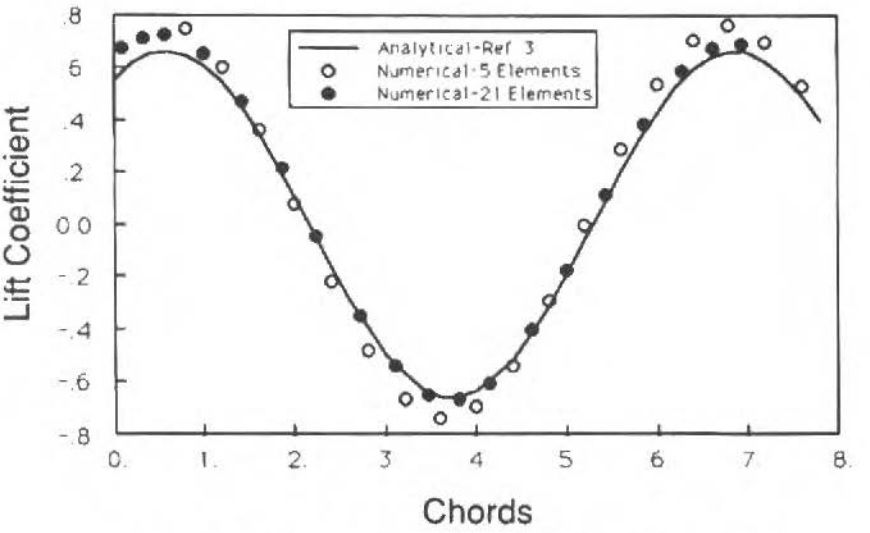

Fig. 5 Lift Coefficient for a Sinusoidal Gust - Sears' Problem. $\Delta t = \Delta X$, $k = 0.5$, gust amplitude is .20 times undisturbed flow velocity.

Finally, in Fig. 6, lift, pitching moment and suction force coefficients are presented for the same case studied in DeLaurier and Winfield (1990). The flat plate undergoes oscillatory midchord plunging and pitching for $k = 0.5$. Pitching angle and plunging amplitudes are 0.1 radians and 0.5 per chord

length respectively. As in Sears' problem, the wave length of the periodic oscillation is great enough to allow a time step $\Delta t = \Delta X$. The same remark can be made concerning finiteness of the free vortex wake at the beginning of numerical calculations.

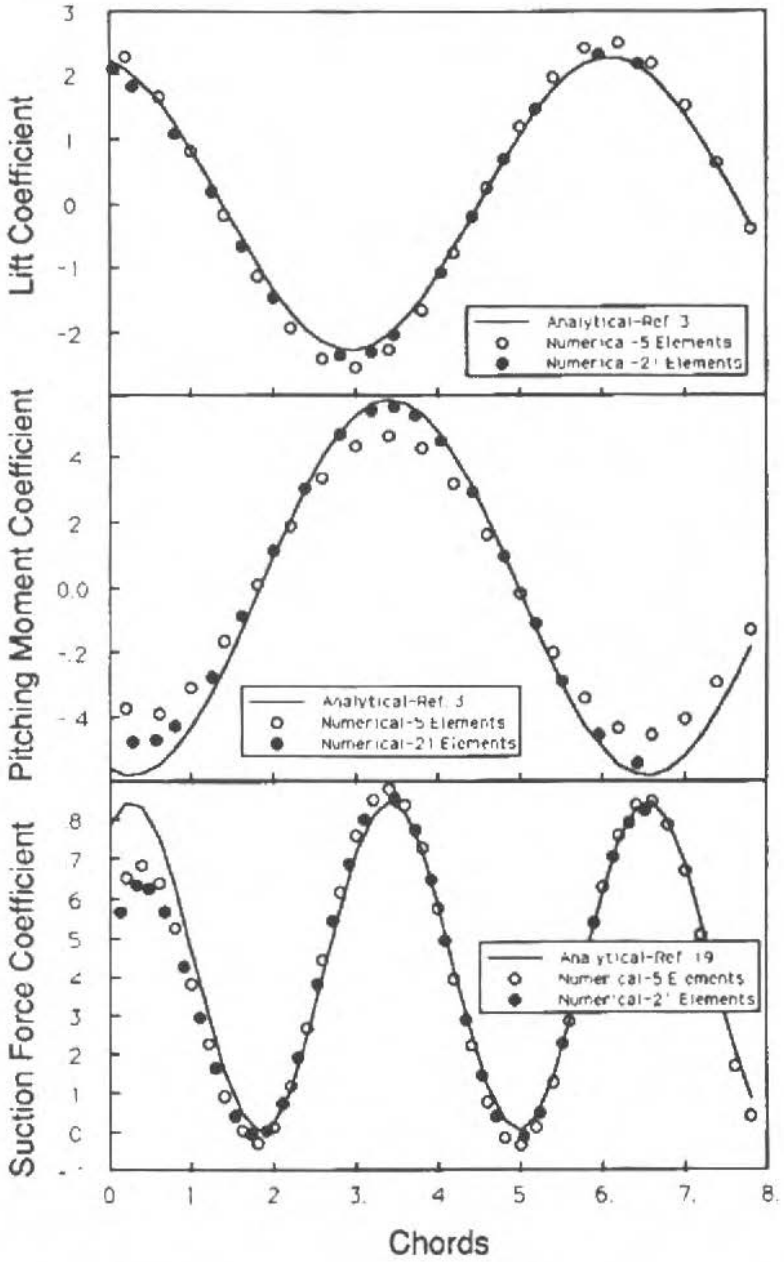

Fig. 6 Lift, Pitching Moment and Suction Force Coefficients for Plunging (h) and Midchord Pitching (α) Motions $\Delta t = \Delta X$, $k = 0.5$, $h = 0.5 \sin(\omega t + \pi/2)$, $\alpha = 0.1 \sin(\omega t)$

Final Remarks

This work may be considered as an extension of the simple lumped vortex method to the two-dimensional flow case. The main advantage of this generalization is the possibility to study gust problems or deformable surfaces. The present numerical model treats all problems as initial value ones, then, for periodic motions, a minimum number of time steps must be considered in order to guarantee that the transient effects die out. From a numerical point of view, due to the constant strength dipole employed to solve the Neumann problem, the enforcements of circulation conservation, Kutta condition and vortex shedding are simpler to establish in relation to other equivalent models. Finally, the importance of the time step chosen, especially in transient or periodic high frequency problems, is properly evidenced.

References

Basu, B.C., and Hancock, G. J., 1978, "The Unsteady Motion of a Two-Dimensional Airfoil in Incompressible Inviscid Flow", Journal of Fluid Mechanics, Vol. 87, pp. 159-178.

Bisplinghoff, R.L., Ashley, H., and Halfman, R.L., 1955, "Aeroelasticity", Addison-Wesley Publ. Co., Reading, MA.

DeLaurier, J., and Winfield, J., 1990, "Simple Marching-Vortex Model for Two-Dimensional Unsteady Aerodynamics", Journal of Aircraft, Vol. 27, pp. 376-378.

Garrick, I.E., 1936. "Propulsion of a Flapping and Oscillating Airfoil", NACA Report No. 567.

Garrick, I.E., 1957, "Nonsteady Wing Characteristics", in High Speed Aerodynamics and Jet Propulsion, Vol. VII, Section F, Princeton University Press, Princeton, NJ.

Giesing, J.P., 1968, "Nonlinear Two-Dimensional Unsteady Potential Flow with Lift", Journal of Aircraft, Vol. 5, pp. 135-143.

Hess, J.L., and Smith, A.M.O., 1966, "Calculation of Potential Flow about Arbitrary Bodies", in Progress in Aeronautical Sciences, Vol. 8, Pergamon Press, Oxford.

Katz, J., and Weihs, D., 1978a, "Hydrodynamic Propulsion by Large Amplitude Oscillation of an Airfoil with Chordwise Flexibility", Journal of Fluid Mechanics, Vol. 88, pp. 485-497.

Katz, J., and Weihs, D., 1978b, "Behavior of Vortex Wakes from Oscillating Airfoils", Journal of Aircraft, Vol. 15, pp. 861-863.

Katz, J., and Weihs, D., 1981, "Wake Rollup and Kutta Condition for Airfoils Oscillating at High Frequency", AIAA Journal, Vol. 19, pp. 1604-1606.

Katz, J., and Plotkin, A., 1991, "Low-Speed Aerodynamics: From Wing Theory to Panel Method", McGraw-Hill Inc., New York, NY.

McCune, J.E., Lam, C.-M.G., and Scott, M.T., 1990, "Nonlinear Aerodynamics of Dimensional Airfoils in Severe Maneuver", AIAA Journal, Vol. 28, pp. 385-393.

Rokhsaz, K., Selberg, B.P., and Eversman, W., 1991, "Effects of Thickness on Unsteady Aerodynamics of Closely Coupled Oscillating Airfoils", Journal of Aircraft, Vol. 28, pp. 312-319.

Schlichting, H., and Truckenbrodt, E., 1979, "Aerodynamics of the Airplane", McGraw-Hill Inc., New York, NY.

Theodorsen, T., 1935, "General Theory of Aerodynamic Instability and the Mechanism of Flutter", NACA Report No. 496.

Van De Vooren, A.I., and Van De Vel, H., 1964, "Unsteady Profile Theory in Incompressible Flow", Archiwum Mechaniki Stosowanej, Vol. 3, pp. 709-735.

von Kármán, T., and Sears, W.R., 1938, "Airfoil Theory for Non-Uniform Motion", Journal of Aeronautical Sciences, Vol. 5, pp. 379-390.

von Kármán, T., and Burgers, J.M., 1976, "General Aerodynamic Theory of Perfect Fluids", in Aerodynamic Theory: A General Review of Progress, Vol. II, Peter Smith, Gloucester.

Yates Jr., E.C., 1985, "Unsteady Subsonic and Supersonic Flows-Historical Review; State of the Art", in Computational Methods in Potential Aerodynamics, Springer-Verlag, Berlin.

RBCM - J. of the Braz. Soc. Mechanical Sciences
Vol. XIX - No 3 - 1997 - pp. 341-356

ISSN 0100-7386
Printed in Brazil

A Numerical Inviscid Vortex Model Applied to Parallel Blade-Vortex Interaction

Gustavo Farias Fonseca
Gustavo César Rachid Bodstein
Miguel Hiroo Hirata
Universidade Federal do Rio de Janeiro
COPPE - Programa de Engenharia Mecânica - C.P. 68503
21945-970 Rio de Janeiro, RJ Brazil

Abstract

In this paper a numerical inviscid vortex method is applied to the unsteady, two-dimensional and incompressible flow that occurs during a parallel blade-vortex interaction. We use a vorticity-panel method, where the airfoil bound vorticity is modeled as a discrete distribution of vortices having strength continuously and linearly distributed over the airfoil surface. The impermeability condition is satisfied on the airfoil surface, whereas the no-slip condition is not. The generation of the wake vorticity is accomplished with the equation of conservation of circulation and the application of the Kutta condition, which imposes the continuity of the pressure field at the airfoil trailing edge. The vortices shed into the flow to form the airfoil wake are convected downstream with the mean flow using a Lagrangian time-marching scheme. The main vortex that interacts with the airfoil is modeled as a potential vortex. The numerical results are compared to the experimental data of Straus et al. (1990), showing good agreement for the entire flow, except when the vortex is close enough to the trailing edge so that separation occurs.

Keywords: *Aerodynamics, Airfoil, Blade-Vortex Interaction, Vortex Methods, Wakes.*

Nomenclature

A = influence matrix of the panel method
c = airfoil chord
C = airfoil contour of integration, or constant in Eq. (33)
C_L = lift coefficient per unit span
C_m = pitching moment coefficient per unit span
C_p = pressure coefficient
h = smallest distance between the airfoil and the vortex
K = interaction parameter
K_a = apparent interaction parameter
l = coordinate system along the airfoil contour
L = lift per unit span
M = pitching moment per unit span
N = number of panels
P = path of integration in Eq. (13)
p = pressure
S = surface of integration
t = time
U = freestream speed
Δt = time step
$\Delta\Gamma$ = variation of circulation in a time step
Γ = vortex strength or circulation
ϕ = velocity potential
ε = numerical error
θ = local angle between x-direction and $\vec{n}$
ρ = fluid density
γ = bound vortex strength or vorticity in the boundary layer
$\vec{u}$ = velocity vector with coordinates (u,v)
$\vec{x}$ = position vector with coordinates (x,y)
$\vec{\omega}$ = vorticity vector with coordinates (0,0,ω)
$\vec{e}_z$ = unit vector in the z-direction
$\vec{n}$ = local unit normal vector

Subscripts:
a = airfoil
i,j = summation indices
k = wake vortices
lte = lower trailing edge
M = at time t_M
o = at t=0
ute = upper trailing edge
v = main vortex
w = wake
∞ = far upstream
ϕ = irrotational component
ω = rotational component

Supercripts:
e = exact
n = numerical
$'$ = evaluated on the surface of integration S or contour C

Introduction

Unsteady flows over airfoils occurs very often in aerodynamics. One commonly encountered situation is the flow around a helicopter rotor, known as Blade/Vortex Interaction (BVI), where the

Manuscript received: August 1996. Technical Editor: Angela Ourivio Nieckele

vorticity generated on a blade's surface is shed from its edges to form a thin wake, which rolls up into finite-cored vortex filaments, the tip (or trailing) vortices. Under certain operating conditions, a tip vortex generated on a rotor blade impinges at an angle on the next approaching blade, producing an interaction that depends on the angle between the vortex's axis and the blade's axis. When the vortex's axis is perpendicular to the blade's axis the flow is nominally steady and three-dimensional. When the vortex's axis is parallel to the blade's axis the flow is unsteady and two-dimensional. In any case, the interaction causes noise, vibration and a strong influence on the blade's aerodynamic performance. We will consider here the aerodynamics aspects of the parallel BVI case, since this interaction affects the flow around the entire blade and causes a strong noise effect (George, 1978).

Numerous studies of unsteady separated flows over airfoils and the numerical simulation of wakes have been published. Numerical work has been done for incompressible flows around airfoils under stall conditions, where the models use formulations with different degrees of sophistication, ranging from (source-based) inviscid methods (Simões, 1993) to (vortex-in-cell) viscous methods (Giannakidis, 1996). More specifically, the parallel BVI phenomenon have been simulated using finite-difference schemes that accounts for compressibility effects. Representative papers of this class are the ones by Rai (1987) and Srinivasan and McCroskey(1989). Panaras (1987), Poling et al. (1989), Lee and Smith (1991), Chacaltana et al. (1995) and others have applied discrete vortex methods coupled with complex variable theory or panel methods to analyze the case where the parallel BVI flow is incompressible. Recent review articles on unsteady incompressible flow over airfoils and the numerical simulation of wakes and BVI have been written by McCune and Tavares (1993) and Mook and Dong (1994). On the other hand, most of the experiments carried out so far deal with noise measurements instead of the aerodynamics of the BVI. A very detailed set of mean pressure measurements on the surface of a NACA 0012 airfoil were performed by Straus et al. (1990), where the evolution of the lift and pitching moment coefficients with time were presented.

The objective of this paper is to apply a numerical, inviscid, vortex method to simulate the unsteady, two-dimensional and incompressible flow that occurs during a parallel blade-vortex interaction. We use a panel method to discretize the airfoil bound vorticity, where each panel has a linear and piecewise-continuous distribution of vorticity. The impermeability condition is enforced on the airfoil contour, but the no-slip condition is not. We impose the Kutta condition through the continuity of the pressure field at the airfoil trailing edge, which, combined with the condition that the circulation in the whole flow must be conserved, provides a model for the vorticity generation at the trailing edge. The vortices shed into the flow to form the airfoil wake are modeled as potential vortices. The main vortex that interacts with the airfoil is also modeled as a potential vortex. All the vortices in the flow are convected with the mean flow using a first-order Lagrangian time-marching scheme. The results of the computations are compared to the experimental data of Straus et al. (1990). The next two sections describe the mathematical and the numerical models, respectively. In the last section we present and discuss the results.

Mathematical Model

Our mathematical model considers the main vortex, that interacts with the blade, to be a 2-D potential point vortex with constant strength Γ (clockwise rotation is considered positive) and position $(x_v(t),y_v(t))$, which moves in a uniform flow with freestream speed U_∞. The blade is modeled as a 2-D airfoil that has chord length c. Figure 1 shows the flow geometry and the cartesian coordinate system used.

We assume the flow to be unsteady, incompressible, and inviscid. The flow is also assumed to be rotational due to the vorticity contained in the main vortex, in the airfoil boundary layer, and in the airfoil wake. For such flow the velocity field $\vec{u} = (u,v)$ must satisfy the continuity equation

$$\nabla \cdot \vec{u} = 0 \qquad (1)$$

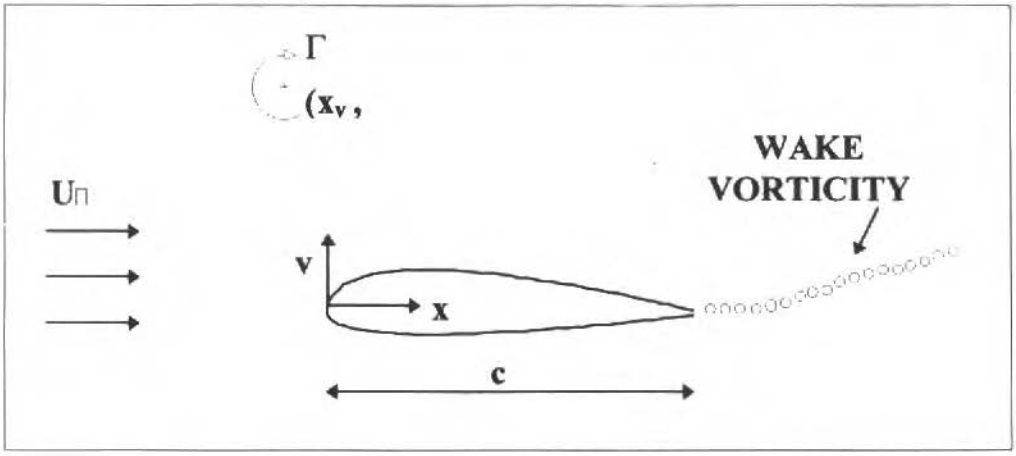

Fig. 1 Schematic Drawing of the Flow Geometry

and the boundary conditions

$$\vec{u} \to \vec{U}_\infty \qquad \text{at infinity} \tag{2a}$$

$$\vec{u} \cdot \vec{n} = 0 \qquad \text{on the airfoil surface} \tag{2b}$$

where $\vec{n}$ is the local unit normal vector on the airfoil surface pointing into the fluid region.

The total vorticity $\vec{\omega}$ in the flow is defined as

$$\vec{\omega} = \nabla \times \vec{u} \tag{3}$$

Following Batchelor (1967), the velocity field in Eqs. (1), (2) and (3) can be decomposed into a potential flow component, $\vec{u}_\phi$, and a rotational flow component, $\vec{u}_\omega$, according to

$$\vec{u} = \vec{u}_\phi + \vec{u}_\omega \tag{4}$$

The rotational flow component satisfies the following equations

$$\nabla \cdot \vec{u}_\omega = 0, \quad \nabla \times \vec{u}_\omega = \vec{\omega} \tag{5}$$

this component vanishes at infinity and has a non-zero normal component on the airfoil surface. As it will be seen in Eq. (10), this component will be canceled out by part of the potential contribution to the velocity field, so that Eq. (2b) is satisfied. Inversion of Eqs. (5) allows us to write $\vec{u}_\omega$ in terms of $\vec{\omega}$ for 2-D flows as

$$\vec{u}_{\omega}(\vec{x},t) = \frac{1}{2\pi} \int_{S_{\omega}} \frac{\vec{\omega}(\vec{x}_0,t) \times (\vec{x} - \vec{x}')}{\left|\vec{x} - \vec{x}'\right|^2} dS(\vec{x}') \tag{6}$$

where $\vec{x}$ is the position vector of a point in the flow and $\vec{x}'$ is the position vector of a point on the surface of integration S_ω with non-zero vorticity.

The potential flow component satisfies

$$\nabla \cdot \vec{u}_{\phi} = 0, \quad \nabla \times \vec{u}_{\phi} = \vec{0} \tag{7}$$

and can be broken up into

$$\vec{u}_{\phi} = \vec{u}_a + \vec{U}_{\infty} \tag{8}$$

where both, the component due to the perturbation caused by the airfoil, $\vec{u}_a$, and the freestream component, $\vec{U}_{\infty}$, satisfy Eqs. (7). The freestream component automatically satisfies Eq. (2a), whereas the airfoil component vanishes at infinity. Equations (7) define a potential flow with $\vec{u}_a = \nabla\phi$, where the (scalar) velocity potential ϕ is a solution to Laplace's equation

$$\nabla^2 \phi = 0 \tag{9}$$

The velocity field u_a is determined uniquely by specified values of its normal component on the airfoil surface, which ensures that the impermeability condition (Eq. (2b)) is satisfied and couples the velocity components through the equation

$$\vec{u}_a \cdot \vec{n} = \nabla\phi \cdot \vec{n} = -\vec{U}_{\infty} \cdot \vec{n} - \vec{u}_{\omega} \cdot \vec{n} \tag{10}$$

The flow assumptions simplify the momentum equations to the Euler equations. The curl of the Euler equations produces the inviscid vorticity transport equation for the vorticity field, which is given by

$$\frac{D\omega}{Dt} \equiv \frac{\partial\omega}{\partial t} + \vec{u} \cdot \nabla\omega = 0 \tag{11}$$

In a two-dimensional flow the vorticity vector has only one non-zero component, namely the component normal to plane of the flow. As a consequence, Eq. (11) turns out to be a scalar equation, and the term responsible for the stretching and tilting of the vortex lines is identically zero. It should also be noted that Eq. (11) implies that the vorticity of each fluid particle is constant with time, and that

the total circulation in the flow is conserved. This allows us to use a Lagrangian time-marching scheme to convect each fluid particle with non-zero vorticity according to

$$\frac{d\vec{x}}{dt} = \vec{u}(\vec{x}(t),t) \tag{12}$$

where $\vec{x}$ is the particle position and $\vec{u}$ is the velocity induced by the entire flow at the particle position, excluding the velocity induced by the particle itself.

Integration of the Euler equations gives rise to the unsteady Bernoulli equation, which can be written in terms of the pressure coefficient C_p as

$$C_p \equiv \frac{p - p_\infty}{1/2\,\rho U_\infty^2} = 1 - |\vec{u}|^2 - 2\frac{\partial \phi}{\partial t} = 1 - |\vec{u}|^2 - 2\frac{d}{dt}\int_P \vec{u}\cdot d\vec{l} \tag{13}$$

being p the static pressure at any point in the flow, p_∞ the upstream static pressure, and ρ the fluid density. The integral in Eq. (13) used to evaluate the velocity potential is carried out along any path P taken from a point far upstream from the leading edge of the airfoil to a point on the airfoil surface. Integrating Eq. (13) on the entire airfoil surface allows us to obtain the lift and pitching moment coefficients per unit span, C_L and C_m respectively, according to

$$C_l \equiv \frac{L}{(1/2)\rho U_\infty^2 c} = -\oint_C C_p \sin\theta dl \tag{14a}$$

$$C_m \equiv \frac{M}{(1/2)\rho U_\infty^2 c} = -\oint_C C_p x \sin\theta dl + \oint_C C_p y \cos\theta dl \tag{14b}$$

In the equations above C is the airfoil contour, θ is the angle between the local direction normal to the airfoil surface and the x-direction, and l is a coordinate along the airfoil surface. The moment is considered positive in the clockwise direction and is calculated about the leading edge.

Applying Kelvin's theorem of conservation of circulation to the flow, we can write

$$\Gamma_v + \Gamma_a(t) + \Gamma_w(t) = \Gamma_o \tag{15}$$

In Eq. (15) $\Gamma_o \equiv \Gamma(t=0) = \Gamma_v = constant$, which is the initial condition used in the computations. The circulations around the main vortex Γ_v, the airfoil Γ_a, and the wake Γ_w are given by

$$\Gamma_v = \frac{\Gamma}{U_\infty c}, \qquad \Gamma_a = \oint_{airfoil} \vec{u}\cdot d\vec{l}, \qquad \Gamma_w = \int_{wake} \vec{\omega}_w \cdot \vec{n}_s dS \tag{16a,b,c}$$

where n_s is a unit vector perpendicular to the plane of the flow. The circulation around the airfoil (or the bound vortex circulation) owing to the vorticity in the airfoil boundary layer is determined by

solving the boundary-value problem comprised of Eqs. (9), (10) and the so-called unsteady Kutta condition. The latter condition requires that the pressures on the lower and upper surfaces of the airfoil be equal at the trailing edge. With the aid of Eq. (13), the Kutta condition may be expressed as

$$\frac{d\Gamma_a}{dt} = \frac{1}{2}(u_{lte}^2 - u_{ute}^2) \tag{17}$$

where u_{lte} and u_{ute} are the tangential lower and upper velocity components on the airfoil surface at the trailing edge, respectively, and $\Gamma_a = (\phi_{ute} - \phi_{lte})$. Equations (15) and (17) furnish a model for the vorticity generation at the airfoil trailing edge. The reader is referred to Giesing (1969), Basu and Hancock (1978), and Mook and Dong (1994) for more detailed discussions about the Kutta condition.

Numerical Model

In our numerical model presented below all the variables are normalized by U_∞ and c. The main vortex is treated as a 2-D point vortex with zero core area and infinite vorticity, such that the dimensionless vortex strength Γ_v is finite. We discretize the airfoil wake also using 2-D point vortices, each of strength Γ_k. Thus, the rotational velocity field $\vec{u}_\omega$ possesses a component due to the main vortex, $\vec{u}_v$, and a component due to the wake, $\vec{u}_w$, that is

$$\vec{u}_\omega = \vec{u}_v + \vec{u}_w \tag{18}$$

Integration of Eq. (6) yields

$$\vec{u}_v(\vec{x},t) = -\frac{\Gamma_v}{2\pi}\vec{e}_z \times \frac{\vec{x} - \vec{x}_v(t)}{|\vec{x} - \vec{x}_v(t)|^2} \tag{19}$$

for the main vortex, and

$$\vec{u}_w(\vec{x},t) = -\sum_{k=1}^{M-1}\frac{\Gamma_k}{2\pi}\vec{e}_z \times \frac{\vec{x} - \vec{x}_k(t)}{|\vec{x} - \vec{x}_k(t)|^2} + \vec{u}_{\Delta\Gamma_w} \tag{20}$$

for the wake, where M is the number of time-steps, $\vec{x}_k$ is the position of the wake vortex Γ_k and $\vec{e}_z$ is a unit vector perpendicular to the plane of the flow that forms a right-hand system with the base vectors in the plane of the flow. The first term on the right-hand side of Eq. (20) is the induced velocity of the (M-1) vortices present in the wake at time t_M, whereas the second term on the right-hand side is the velocity induced by the vorticity shed by the airfoil at time t_M with strength $\Delta\Gamma_w$. The total vorticity in the wake Γ_w is obtained by applying Stokes' theorem to Eq. (16c) and discretizing it as follows

$$\Gamma_w = \sum_{k=1}^{M-1}\Gamma_k + \Delta\Gamma_w \tag{21}$$

In order to determine the airfoil perturbation velocity component $\vec{u}_a$ we must solve the boundary-value problem comprised by Eqs. (9), (10) and (17). For this purpose, we adopt a scheme based on the one proposed by Vezza and Galbraith (1985a), who applied it to unsteady airfoil flows involving a step-change in incidence, sinusoidal oscillations, and ramp motions, but not to BVI-type flows. A potential flow solution is constructed based on a vorticity-panel method, where the vorticity in the boundary layer makes up the bound vorticity on the airfoil surface. Rewriting Eq. (6), the velocity induced by the airfoil boundary layer is given by

$$\vec{u}_a(\vec{x},t) = -\frac{1}{2\pi}\vec{e}_z \times \oint_C \frac{\gamma[l(\vec{x}'),t](\vec{x}-\vec{x}')}{\left|\vec{x}-\vec{x}'\right|^2} dl(\vec{x}') \tag{22}$$

where γ is the local circulation strength (per unit length) in the boundary layer, C is the airfoil contour and l is the distance along C measured from the lower trailing edge. It can be shown (Mook and Dong, 1994) that, under the boundary layer assumptions, integration of the boundary-layer vorticity $\vec{\gamma}\vec{e}_z$ over the boundary-layer thickness δ, in the limit as δ goes to zero, yields

$$\gamma(l,t) = u(l,t) \tag{23}$$

where u(l,t) is the tangential velocity at time t and position l on the airfoil surface. Therefore, the thin boundary layer is approximated as a bound vorticity distribution, with local strength γ.

Although we can determine ϕ from Eq. (22) so that $\vec{u}_a = \nabla\phi$ and Eq. (9) is satisfied, we can work directly with $\vec{u}_a$. First the airfoil contour is discretized into N small panels, each of them containing a linear vorticity distribution that is piecewise continuous at each one of the N+1 panel endpoints (nodes). The line integral in Eq. (22) is evaluated so that we can write the component of $\vec{u}_a$ normal to the midpoint (control point) of the ith panel as

$$\vec{u}_a(\vec{x},t)\cdot\vec{n} = \sum_{j=1}^{N+1} A_{ij}\gamma_j \tag{24}$$

In Equation (24) the summation is carried out over the panel nodes, and the A_{ij}'s are the influence coefficients, which are functions of the airfoil geometry. These coefficients can be found in Mook and Dong (1994) or Katz and Plotkin (1991).

With the aid of Eq. (23), the Kutta condition (Eq. (17)) is discretized as follows

$$\Delta\Gamma_a \equiv \Gamma_a(t_M) - \Gamma_a(t_{M-1}) = \frac{1}{2}\Delta t(\gamma_{lte}^2 - \gamma_{ute}^2) = (\gamma_{lte} - \gamma_{ute})\left[\frac{(\gamma_{lte} + \gamma_{ute})}{2}\Delta t\right] \tag{25}$$

where Δt is the dimensionless time-step and $\Gamma_a(t)$ is calculated from a numerical integration of Eq. (16b). Equation (15) for the conservation of circulation requires that the amount of shed vorticity $\Delta\Gamma_w$ that adds up to the wake at time t_M is

$$\Delta\Gamma_w = -\Delta\Gamma_a \tag{26}$$

Based on Eqs. (25) and (26), the vorticity shed at the trailing edge is modeled as an extra panel, whose strength per unit length $(\gamma_{lte} - \gamma_{ute})$ is considered constant. Thus, the extra panel strength takes the form

$$\Delta\Gamma_w = (\gamma_1 + \gamma_{N+1})\Delta_M \tag{27}$$

where $\gamma_{lte} = -\gamma_1$ and $\gamma_{ute} = \gamma_{N+1}$. In Equation (27) the length of the extra panel Δ_M is given by the term in square brackets that appears in Eq. (25), that is

$$\Delta_M = \frac{\gamma_{N+1} - \gamma_1}{2}\Delta t \tag{28}$$

where the extra panel inclination θ_M is determined by ensuring that the shed vorticity leaves the trailing edge along a local streamline, i.e.,

$$\theta_M = tan^{-1}\left(\frac{v_{wM}}{u_{wM}}\right) \tag{29}$$

The angle θ_M is positive in the counterclockwise direction, measured with respect to the x-axis of a local cartesian coordinate system placed at the trailing edge; the velocity components u_{wM} and v_{wM} are calculated at the panel control point.

As one can see from Eq. (23), the tangential velocity on the airfoil surface is non-zero and equal to the local bound vortex circulation. The model, therefore, does not satisfy the no-slip condition. We must, however, impose the impermeability condition on the airfoil in order to determine the bound circulation distribution $\gamma(l,t)$. With the aid of Eqs. (18), (19), (20) and (24) we can write Eq. (10) for the ith control point as follows

$$\sum_{j=1}^{N+1} A_{ij}\gamma_j + (\gamma_1 + \gamma_{N+1})A_{wi} = -\vec{U}_\infty \cdot \vec{n} + \frac{\Gamma_v}{2\pi}\left[\vec{e}_z \times \frac{\vec{x} - \vec{x}_v(t)}{|\vec{x} - \vec{x}_v(t)|^2}\right] \cdot \vec{n} + \sum_{k=1}^{M-1}\frac{\Gamma_k}{2\pi}\left[\vec{e}_z \times \frac{\vec{x} - \vec{x}_k(t)}{|\vec{x} - \vec{x}_k(t)|^2}\right] \cdot \vec{n} \tag{30}$$

where A_{wi} is the influence coefficient of the wake extra panel.

Our algorithm then consists of applying Eq. (30) to the N airfoil control points, which generates an underdetermined linear algebraic system comprised of N equations and N+1 unknown γ_i's. In order to render the system determined we include three more equations, namely Eqs. (27), (28) and (29), which adds two more unknowns, Δ_M and θ_M. In practice, the computations are performed so that Δ_M and

θ_M are first guessed, yielding a system with N+1 equations and N+1 unknowns. After the solution is obtained, Eqs. (28) and (29) are used again to recalculate the values of A_M and θ_M, and so on. This procedure is repeated until both variables converge up to a tolerance of 0.1%. As soon as the computation at time t_M converges the pressure distribution and the lift and pitching moment coefficients on the airfoil are calculated. The main vortex and the (M-1) wake vortices are then convected using a first-order (Lagrangian) time-marching scheme, obtained from a discretization of Eq. (12) in the form

$$\vec{x}_{M+1} = \vec{x}_M + \vec{u}_M \Delta t \tag{31}$$

Finally, the wake extra panel is transformed into a point vortex with strength $\Delta\Gamma_w$ and convected using Eq. (31). The dimensionless computational time t_M is then incremented by Δt (also dimensionless) and the entire procedure is repeated until a pre-specified non-dimensional time is reached.

The loads on the airfoil are computed from equations (14), which take the form

$$C_L = \oint_C \gamma^2(l,t)\sin\theta(l)dl + 2\frac{d}{dt}\oint_C \sin\theta(l)\int_0^l \gamma(\xi,t)d\xi dl \tag{32a}$$

$$C_M = \oint_C \gamma^2(l,t)x(l)\sin\theta(l)dl - \oint_C \gamma^2(l,t)y(l)\cos\theta(l)dl$$

$$+2\frac{d}{dt}\oint_C x(l)\sin\theta(l)\int_0^l \gamma(\xi,t)d\xi dl - 2\frac{d}{dt}\oint_C y(l)\cos\theta(l)\int_0^l \gamma(\xi,t)d\xi dl \tag{32b}$$

The lower limit of integration in the innermost integrals is at the airfoil trailing-edge, and l is a surface point. Equations (32) are integrated using a standard numerical procedure (Press et al., 1989).

Results and Conclusions

We begin our discussion section presenting some convergence results obtained using the approach of Moran (1984) as a basis. Our algorithm is asymptotically first order in the time-step Δt and second order in the number of panels N. This implies that the numerical error varies linearly with Δt and quadratically with 1/N. Assuming that other parameters have a weak influence on the absolute numerical error ε, defined in terms of Γ_w, we can write the following mathematical relation

$$\varepsilon \equiv \left|\Gamma_w^n - \Gamma_w^e\right| = C\Delta t\left(\frac{1}{N}\right)^2 \tag{33}$$

where the superscripts "n" and "e" refer to numerical and exact, respectively. In the absence of an analytical solution that allows us to obtain the exact value of Γ_w^e, we used Eq. (33) to estimate the values of Γ_w^e and C. An algebraic system of two equations for the two unknowns Γ_w^e and C can be formed for any two sets of dimensionless parameters $(\Gamma_{w,i}^n, \Delta t_i, N_i)$, where $\Gamma_{w,i}^n$ is computed in run i for given $(\Delta t_i, N_i)$, i=1,2. Two batches of numerical runs were thus carried out to estimate Γ_w^e and C; the results of the first batch are shown in Fig. 2a as a plot of ε in terms of Δt for $N = 200$, and the results of the second batch are shown in Fig. 2b as a plot of ε in terms of N for $\Delta t = 0.00625$. Only sets of parameters (corresponding to pairs of points in Fig. 2) that yielded approximately the same values of Γ_w^e and C were used to compute average values, resulting in $\Gamma_w^e = 0.038679$ and $C = 29$. Note that the points in Fig. 2a follow approximately a straight line with slope 1 in a log-log plot, whereas the points in Fig. 2b have a slope approximately equal to 2, in accordance with Eq. (33). This equation therefore provides a good control over the numerical errors involved in the model, and, therefore, any discrepancy that appears when our numerical results are compared to experimental data are due to the model itself, and not due to discretization and/or round-off errors. All the runs presented in Fig. 2 were performed for $\Gamma_v = -0.15$. The numerical results that we use to compare with experiments were obtained for $\Delta t = 0.01$ and $N = 200$, which provide relative errors ε_r $(\equiv \varepsilon / \Gamma_w^e)$ lower than 0.06% (computed using Eq. (33)).

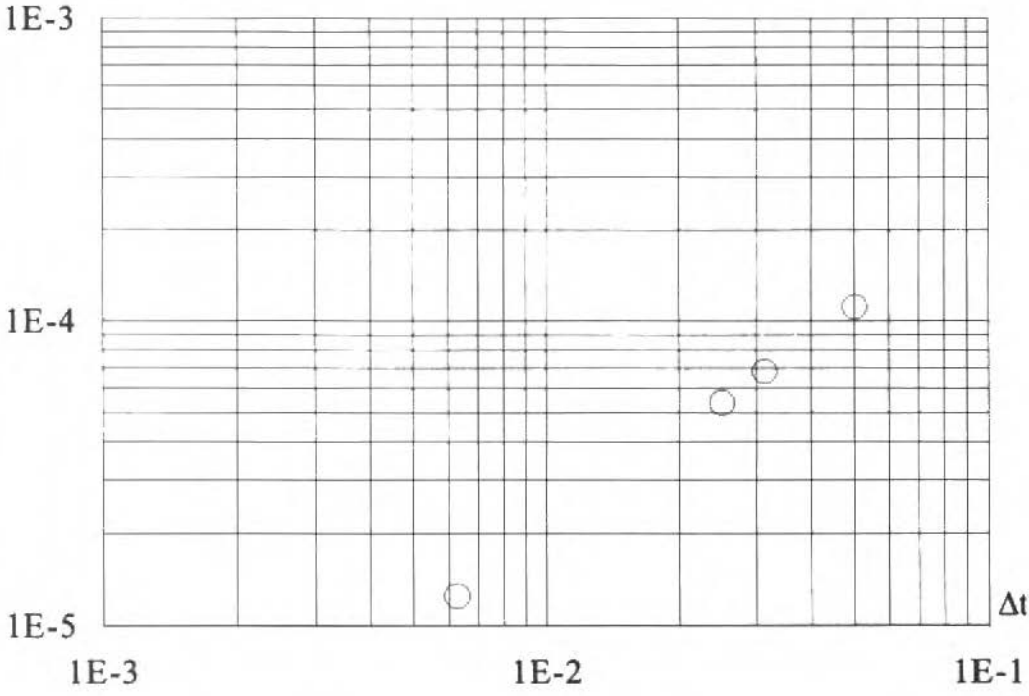

Error Dependence on Δt ; Fixed $N = 200$

Fig. 2a Convergence Test

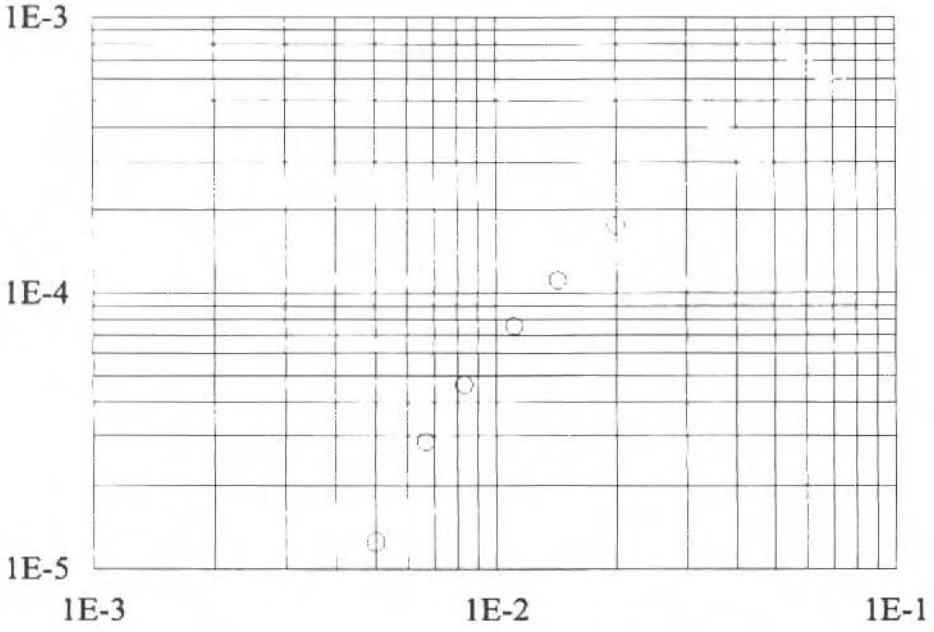

Error Dependence on $1/N$; Fixed $\Delta t = 0.00625$

Fig. 2b Convergence Test

Turning our attention back to the BVI analysis, we now present the numerical results of our model compared to the experimental results of Straus et al. (1990) obtained for a NACA 0012 airfoil set at zero angle of attack. In the cases discussed below the vortex was released at $x_{vo} = -3.33$ and $y_{vo} = 0.24$ for $\Gamma_v = -0.15$, and $x_{vo} = -3.33$ and $y_{vo} = 0.19$ for $\Gamma_v = 0.16$, which are the positions where the vortex was generated in each case studied experimentally by Straus et al. The subscript "o" above denotes values at t=0.

We first look into our numerical results for the path taken by the vortex during the interaction. As the vortex approaches the airfoil, the interaction causes the vortex to be displaced from its straight upstream trajectory, so that it follows a streamline (Fig. 3). When the vortex rotates in the counterclockwise direction $(\Gamma_v = -0.15)$ the minimum distance h between the vortex and the airfoil upper surface is 24% of the airfoil chord, whereas h is $0.13c$ for $\Gamma_v = 0.16$. If we define, based on physical intuition, a dimensionless quantity, called Interaction Parameter and denoted by K, according to

$$K \equiv \frac{\Gamma}{U_\infty h} = \frac{\Gamma_v}{h_v} \tag{34}$$

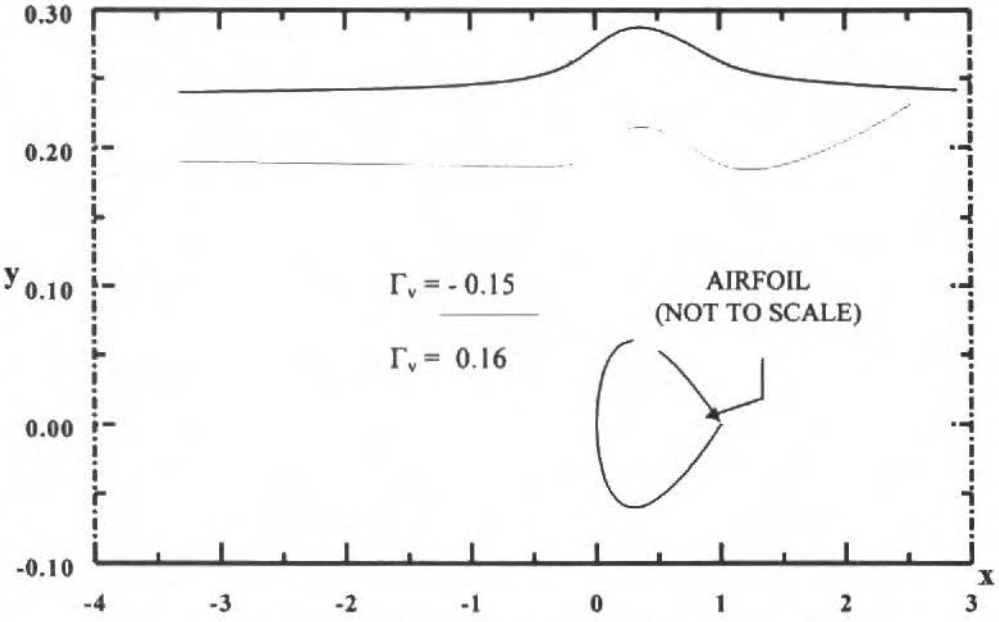

Fig. 3 Vortex Path Above the Airfoil

where $h_v = h/c$, Eq. (34) tells us that the interaction becomes strong for high values of Γ_v and/or low values of h_v. Using the results of Fig. 3, we calculate $K = -0.63$ for $\Gamma_v = -0.15$ and $K = 1.23$ for $\Gamma_v = 0.16$, where the latter corresponds to the strongest interaction case. Although the interaction quantity K is the one that actually measures the degree of interaction between the airfoil and the vortex, its definition according to Eq. (34) implies that the problem must be solved before K can be determined. We can alternatively define a second dimensionless parameter, which can be called "Apparent Interaction Parameter" and denoted by K_a, as follows

$$K_a \equiv \frac{\Gamma_v}{y_{vo}} \tag{35}$$

where y_{vo} is the dimensionless distance in the y-direction between the vortex and the airfoil at t=0. The parameter K_a has the advantage over K that it can be calculated a priori, without the need to solve the problem. For the cases above, $K_a = -0.63$ for $\Gamma_v = -0.15$ and $K_a = 0.84$ for $\Gamma_v = 0.16$. Again, it is clear that the case where the vortex rotates in the clockwise direction corresponds to the strongest interaction case.

The results for the temporal variation of the airfoil lift coefficient C_L, as the vortex passes over the blade, are presented in Fig. 4 for the two values of the vortex strength. For $\Gamma_v = -0.15$, the vortex induces a counterclockwise rotating flow that produces a local positive angle of attack on the airfoil, creating positive lift. At the beginning of the motion the airfoil experiences a small positive lift coefficient, which increases, as the vortex approaches the airfoil, up to a maximum value in the vicinity of the airfoil leading edge. When the vortex is above the airfoil, the local angle of attack is still positive in the trailing-edge region, but it becomes negative in the leading-edge region. The lift coefficient then starts to decrease at a relatively high rate of change. Downstream of the trailing edge the lift coefficient is already negative. For $\Gamma_v = 0.16$, the sign of the lift coefficient and the trend of its temporal variation

reverse, as expected. Similar results are observed for the pitching moment coefficient C_m about the leading edge, as one can see in Fig. 5. The moment is considered positive in the clockwise direction. For $\Gamma_v = -0.15$ the lift force is positive, as discussed above, and the moment about the leading edge is negative. This happens for the entire initial motion, up to the airfoil leading-edge region. When the vortex is above the airfoil the lift force is still positive, although decaying fast, which causes a negative moment. By the trailing edge region, the moment changes sign. The agreement between the numerical and the experimental results is good for both C_L and C_m. When the vortex is in the trailing-edge region, some discrepancy is observed, which is larger for $\Gamma_v = 0.16$, the strongest interaction case. The reason for that may be attributed to the possible occurrence of flow separation on the airfoil surface, as pointed out by Straus et al., although the boundary layer was observed to be turbulent in the experiments. Our model is unable to predict flow separation.

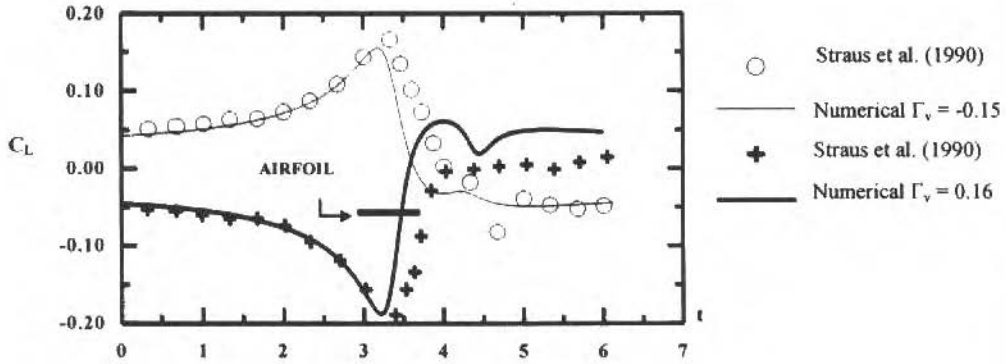

Fig. 4 Temporal Variation of the Lift Coefficient

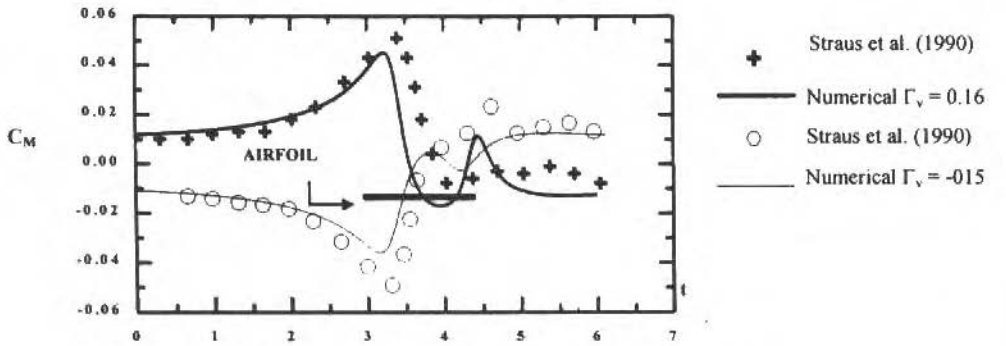

Fig. 5 Temporal Variation of the Pitching Moment Coefficient

Figure 6 depicts the time histories for the pressure coefficient at the quarter-chord point on both the upper and lower surfaces of the airfoil. This point is the center of pressure for a steady uniform flow over a symmetric airfoil at an angle of attack. Fig. 6a corresponds to the results for the $\Gamma_v = -0.15$, and Fig. 6b for $\Gamma_v = 0.16$. Again the agreement is good for most of the flow, but it presents some

discrepancy when the vortex is in the neighborhood of the trailing-edge. The discrepancy is again larger for the strongest interaction case, where flow separation occurs.

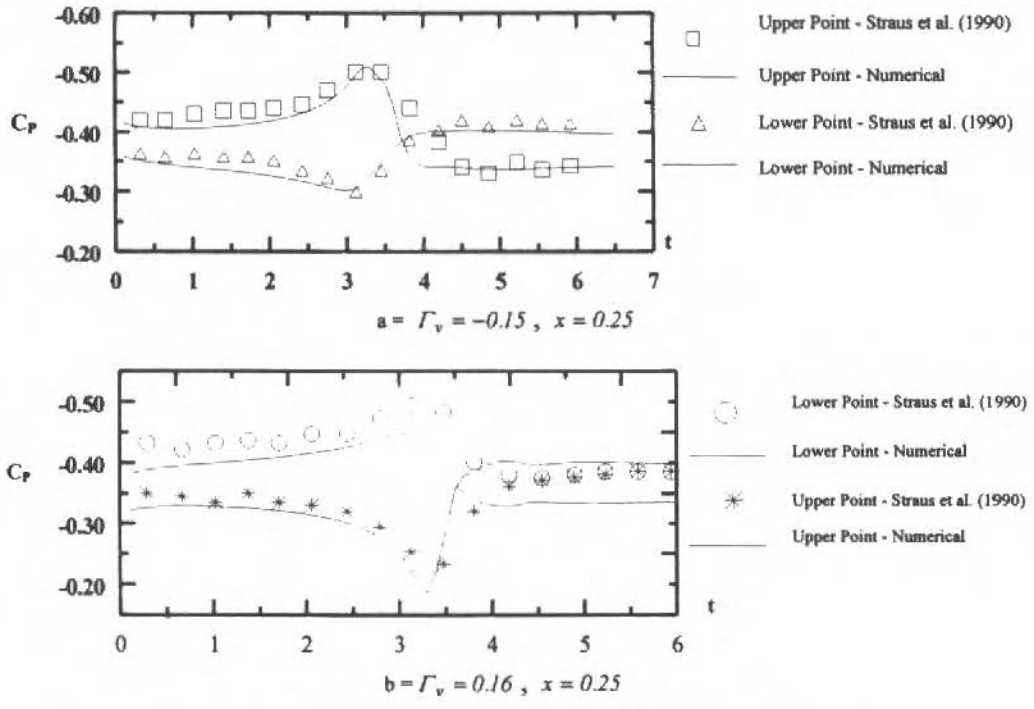

Fig. 6 Upper and Lower C_p Time Histories on the Airfoil Surface

It is important to note that the total circulation in the experiments is zero, since the vortex is generated in the wind tunnel by a second (NACA 0018) airfoil placed upstream of the test airfoil, and the whole flow begins from rest. In our computations the total circulation is Γ_v, which is the initial condition. As the comparisons have shown, the effect of the vortex-generating airfoil and the time for its wake to develop and form the main vortex may be neglected for the cases studied above. Two reasons for this can be pointed out. First, the bound circulation of the test airfoil is relatively small, and the vortex-generating airfoil is about 3.34 chord lengths far from the test airfoil's leading edge; these two parameters act together to cause a small induced velocity field on the leading edge of the test airfoil ($0.0076U_\infty$ in absolute value). Second, as stated by Straus et al. in their paper, the actual time required to pitch the airfoil, 15 ms in the experiments, must be less than the threshold time for the air to travel one chord of the pitching (or vortex-generating) airfoil, 21 ms in the experiments. Consequently, the vortex is fully generated when it reaches one chord length downstream of the trailing edge of the generating airfoil. These values yield dimensionless time intervals of approximately 0.56 and 0.40, respectively, which correspond to distances of 0.56 and 0.4 chord lengths, approximately. During this initial motion, the vortex is still far from the test airfoil. In fact, two runs of the code were conducted for the same cases studied above changing only the initial vortex release point to $x_v(t=0) = -2.77$, corresponding to $(-3.33 + 0.56)$. The largest difference occurred at the vortex release point; this

difference was observed to be very small by the time the vortex reaches one chord length upstream of the airfoil's leading-edge (in fact it is not noticeable when the results are plotted in a graph).

In conclusion, the numerical inviscid vortex model used here to predict the aerodynamics of the BVI phenomenon is able to capture global and local flow properties very well. In situations where viscous effects become important the model presents some discrepancy with respect to the experiments of Straus et al. (1990). This observation suggests that a more elaborated model must be implemented that takes into account the possible occurrence of flow separation. Three possibilities for such model, within the vortex method framework, could be mentioned: first, a model similar to the one used here could be employed to release vorticity from a fixed separation point (Vezza and Galbraith, 1985b); second, a model that solves the boundary layer equations in its integral formulation and feeds information to the potential flow model about the point where separation takes place and how much vorticity must be released into the flow at that point (Kamemoto, 1989); third, a model that satisfies the no-slip condition and allows for the generation of vorticity on the entire airfoil surface at every time-step, which is able to predict separation as part of the solution (Porthouse and Lewis, 1981).

Acknowledgments

The authors would like to acknowledge CAPES for the M.Sc. scholarship granted to G. F. Fonseca during the past two years, and CNPq for the financial support, under grant no. 521260/94-9, during the development of this project.

References

Batchelor, G.K., 1967, "Introduction to Fluid Dynamics", Cambridge University Press, Cambridge.

Basu, B.C. and Hancock, G.J., 1978, "The Unsteady Motion of a Two-Dimensional Aerofoil in Incompressible Inviscid Flow", Journal of Fluid Mechanics, Vol. 87, pp. 159-178.

Chacaltana, J.T.A., Bodstein, G.C.R. and Hirata, M.H., 1995, "Analytical Study of the Time-Dependent 2-D Interaction of a Thin Airfoil and a Vortex in the Presence of a Ground-Plane", Proceedings, 13th ABCM - Mechanical Engineering Conference (COBEM), Belo Horizonte, Brazil.

George, A.R., 1978, "Helicopter Noise: State of the Art", Journal of Aircraft, Vol. 15, pp. 707-715.

Giannakidis, G., 1996, "Prediction of H.A.W.T. Blade Stall and Performance", Final Report, Dept. of Aeronautics, Imperial College, London.

Giesing, J.P., 1969, "Vorticity and Kutta Condition for Unsteady Multienergy Flows", ASME Journal of Applied Mechanics, Vol. 91, pp. 608-613.

Kamemoto, K. and Suzuki, T., 1989, "A Vortex Method for Predicting Unsteady Flow and Boundary Layer Development around an Airfoil", in "Boundary Element Methods", edited by Annigeri, B.S. and Tseng, K., Springer-Verlag, pp. 51-57

Katz, J. and Plotkin, A., 1991, "Low Speed Aerodynamics - From Wing Theory to Panel Methods", McGraw-Hill, New York.

Lee, D.J. and Smith, C.A., 1991, "Effect of Vortex Core Distortion on Blade-Vortex Interaction", AIAA Journal, Vol. 29, pp. 1355-1362.

McCune, J.E. and Tavares, T.S., 1993, "Perspective: Unsteady Wing Theory - The Karman/Sears Legacy", ASME Journal of Fluids Engineering, Vol. 115, pp. 548-560.

Mook, D.T. and Dong, B., 1994, "Perspective: Numerical Simulations of Wakes and Blade-Vortex Interaction", ASME Journal of Fluids Engineering, Vol. 116, pp. 5-21.

Moran, J., 1984, "An Introduction to Theoretical and Computational Aerodynamics", John Wiley & Sons, New York.

Panaras, A.G., 1987, "Numerical Modeling of the Vortex/Airfoil Interaction", AIAA Journal, Vol. 25, pp. 5-11.

Poling, D.R., Dadone, L. and Telionis, D.P., 1989, "Blade-Vortex Interaction", AIAA Journal, Vol. 27, pp. 694-699.

Porthouse, D.T.C. and Lewis, R.I., 1981, "Simulation of Viscous Diffusion for Extension of the Surface Vorticity Method to Boundary Layers and Separated Flows", Journal of Mechanical Engineering and Science, Vol. 23, No. 3, pp. 157-167.

Press, W.H., Flannery, B.P., Teukolsky, S.A. and Vetterling, W.T., 1989, "Numerical Recipes - The Art of Scientific Computing (FORTRAN VERSION)", Cambridge University Press, Cambridge.

Rai, M.M., 1987, "Navier-Stokes Simulations of Blade-Vortex Interaction Using High-Order Accurate Upwind Schemes", AIAA Paper 87-0543.

Simões, F.J., 1993, "Um Modelo Potencial Bi-Dimensional para Escoamentos Separados que Permite a Verificação de uma Hipótese para Explicação do Efeito de Himmelskamp", 12th ABCM - Mechanical Engineering Conference (COBEM), Brasília, Brazil.

Srinivasan, G.R. and McCroskey, W.J., 1989, "Unsteady Interaction of a Rotor with a Vortex", AIAA Paper 89-1848.

Straus, J., Renzoni, P. and Mayle R.E., 1990, "Airfoil Pressure Measurements During a Blade Vortex Interaction and a Comparison with Theory", AIAA Journal, Vol. 28, pp. 222-228.

Vezza, M. and Galbraith, R.A.McD., 1985a, "A Method for Predicting Unsteady Potential Flow about an Aerofoil", International Journal for Numerical Methods in Fluids", Vol. 5, pp. 347-356.

Vezza, M. and Galbraith, R.A.McD., 1985b, "An Inviscid Method of Unsteady Aerofoil Flow with Fixed Upper Surface Separation", International Journal for Numerical Methods in Fluids", Vol. 5, pp. 577-592

RBCM - J. of the Braz. Soc. Mechanical Sciences
Vol. XIX - No.3 - 1997 - pp. 357-370

ISSN 0100-7386
Printed in Brazil

Convergence Acceleration Applied to Compressible and Incompressible Fluid Flow Calculations

Álvaro Luiz De Bortoli
Federal University of Rio Grande do Sul
CPGMAp - Applied Mathematics
90501-900 Porto Alegre, RS Brazil

Abstract

Today, numerical flow simulation plays more and more important role in the design process of an aerodynamic body. To design a new mechanical device involving fluid dynamics, a numerical simulation is well accepted and justified. However, much work still remains to improve the numerical methods towards a fast, accurate and stable convergence. Techniques to accelerate the convergence, namely the local time-stepping, residual averaging and multigrid techniques are normally employed. This work employs acceleration techniques to solve compressible and incompressible fluid flows using a finite volume, explicit Runge-Kutta multistage scheme with central spatial discretization in combination with multigrid and preconditioning. Numerical results are presented for a three dimensional channel and the NACA 00012 airfoil for Mach-numbers ranging from 0.8 to 0.005 using the Euler equations.

***Keywords**: Numerical Simulation, Aerodynamics, Finite Volume, Multigrid, Compressible and Incompressible Flows, Runge-Kutta Method.*

Introduction

Numerical simulation plays nowadays an important role to predict the flow field in many situations where experiments are usually too expensive or even impossible. The rapid evolution of computational fluid dynamics has been driven by the need of faster and most accurate methods for the calculation of flow fields around configurations of technical interest. However, the numerical methods present still limitations. Therefore, much work still remains to improve them towards a fast, accurate and stable convergence.

There are well known methods to solve compressible (Jameson et al, 1981) (Kroll and Jain, 1987) and incompressible fluid flows (Raithby and Schneider, 1979) (Patankar, 1981) (Karki and Patankar, 1989). However, some of these methods present some drawbacks towards its accuracy, cost and applicability. Not all methods can be easily and efficiently employed to analyse compressible and incompressible flow problems. The numerical methods have certain limitations, which must be investigated in order to obtain a suitable method to solve the governing equations of flow problems.

The governing equations of flow problems, the Navier-Stokes equations, are always as possible simplified for the numerical solution in many situations. This is done in order to reduce the computational costs. However, there are problems that can not be analysed using simplified equations, for example flows with strong shocks and with vorticity. Besides, the only adequate model for non viscous flows are the Euler equations (Radespiel, 1989), that requires a minimum of assumptions. Although the great development of modern computational methods, some experimental measurements and/or theoretical solutions must be employed in order to compare a new numerical code. One way to prove the validity of the numerical Euler solutions is to compare them with analytical solutions (potential flows).

In order to eliminate the difficulties of the compressible method to solve incompressible flows, preconditioning is suggested (Choi and Merkle, 1985) (Choi and Merkle, 1993) (Turkel, 1992). It consists in the transformation of the governing equations into a form that is better conditioned, ensuring rapid convergence to obtain steady state solutions. The same time-stepping scheme and spatial discretization can be employed to solve compressible as well as incompressible flows (De Bortoli, 1994).

Techniques to accelerate the convergence are required in order to efficiently solve flow problems. Some of these approaches, namely the local time-stepping, residual averaging and multigrid techniques

Manuscript received: January 1996. Technical Editor: Angela Ourivio Nieckele

(Brandt, 1981) (Jameson, 1985) (Radespiel, 1989) are employed. The local time-stepping allows to obtain steady state solutions with less computational effort. Residual averaging is used to increase the Courant number of an explicit scheme and consists in replacing the residuals by an average of neighbouring residuals. The idea of the multigrid approach is to use a sequence of successively coarser meshes to efficiently damp disturbances through the flow field (Brandt, 1981).

This work apply acceleration techniques to solve compressible and incompressible fluid flows using the finite volume explicit Runge-Kutta multistage scheme with central spatial discretization in combination with multigrid. Numerical results are presented for a three dimensional channel (tunnel) and the NACA 0012 airfoil for Mach-numbers ranging from 0.8 to 0.005 (De Bortoli, 1994). This is done in order to show that the same methodology can be employed to solve compressible as well as incompressible fluid flow problems accuratly. Applications of the standard compressible method for the Navier-Stokes equations is easily found in the literature (Radespiel, 1989).

Governing Equations

The governing equations for non viscous flows are the Euler equations. They can be written in Cartesian coordinates as (Kroll and Jain, 1987):

$$\frac{\partial \vec{W}}{\partial t} + \frac{\partial \vec{F}_1}{\partial x} + \frac{\partial \vec{F}_2}{\partial y} + \frac{\partial \vec{F}_3}{\partial z} = 0 \tag{1}$$

where

$$\vec{W} = \begin{Bmatrix} \rho \\ \rho u \\ \rho v \\ \rho w \\ \rho E \end{Bmatrix}, \vec{F}_1 = \begin{Bmatrix} \rho u \\ \rho uu + p \\ \rho uv \\ \rho uw \\ \rho uH \end{Bmatrix}, \vec{F}_2 = \begin{Bmatrix} \rho v \\ \rho vu \\ \rho vv + p \\ \rho vw \\ \rho vH \end{Bmatrix}, \vec{F}_3 = \begin{Bmatrix} \rho w \\ \rho wu \\ \rho wv \\ \rho ww + p \\ \rho wH \end{Bmatrix} \tag{2}$$

The total energy and total enthalpy are

$$E = e + \frac{u^2 + v^2 + w^2}{2}, \quad H = E + \frac{p}{\rho}$$

where e is the internal energy and u, v and w the velocity components.

To close this system of equations the state equation for a perfect gas (Kroll and Jain, 1987) is employed

$$p = \rho RT = (\gamma - 1)\rho[E - \frac{u^2 + v^2 + w^2}{2}] \tag{3}$$

where R is the gas constant, γ the specific heat ratio, ρ the density, u, v and w the velocity components and p the pressure. Equation (1) can be cast into the integral form (Kroll and Jain, 1987)

$$\int_V \frac{\partial \vec{W}}{\partial t} dV + \int_S (\overline{\overline{F}}.\vec{n}) dS = 0 \tag{4}$$

where $\overline{\overline{F}}$ is the convective tensor.

It is well known that when the magnitude of velocity becomes small, in comparison with the acoustic speed, the time-marching schemes converge very slowly. Therefore, preconditioning is employed. It consists basically in multiplying the vector W by a special matrix, which modifies the form of the governing equations (Choi and Merkle, 1985). Based on the conservative variables, the following preconditioning matrix is employed:

$$\Gamma \frac{\partial \vec{W}}{\partial t} + \frac{\partial \vec{F}_1}{\partial x} + \frac{\partial \vec{F}_2}{\partial y} + \frac{\partial \vec{F}_3}{\partial z} = 0 \tag{5}$$

where (Choi and Merkle, 1985)

$$\Gamma = \begin{bmatrix} 1 & 0 & 0 & 0 & 0 \\ 0 & 1 & 0 & 0 & 0 \\ 0 & 0 & 1 & 0 & 0 \\ 0 & 0 & 0 & 1 & 0 \\ \frac{u^2+v^2+w^2}{2}(M^{-2}-1) & u(1-M^{-2}) & v(1-M^{-2}) & w(1-M^{-2}) & M^{-2} \end{bmatrix} \tag{6}$$

Inspection of this preconditioning matrix indicates that the energy equation is transformed into temperature for low Mach-numbers. Thus, the eigenvalues of the resultant system of equations will be very similar when the Mach-number goes to zero, laying the basis of construction of efficient solvers to solve compressible and/or incompressible flows (Choi and Merkle, 1993).

Description of the Numerical Method

One of the differences among the various finite volume formulations known in the literature is the arrangement of the control volume and update points for the flow variables. The most frequently used schemes are the cell-centered, cell-vertex and node-centered approach (Kroll and Jain, 1987) (Radespiel, 1989). Each of these schemes has its advantages and disadvantages. The discretization used here is based on the node-centered/cell-centered arrangements, as shown in Fig. 1, in order to simplify the use of multigrid techniques.

As Eq. (1) is valid for arbitrary control volume, it is also valid for volume $V_{i,j,k}$, that means

$$\frac{\partial \vec{W}_{i,j,k}}{\partial t} = -\frac{1}{V_{i,j,k}} \int_S (\overline{\overline{F}}.\vec{n}) dS = -\frac{1}{V_{i,j,k}} \vec{Q}_{i,j,k} \tag{7}$$

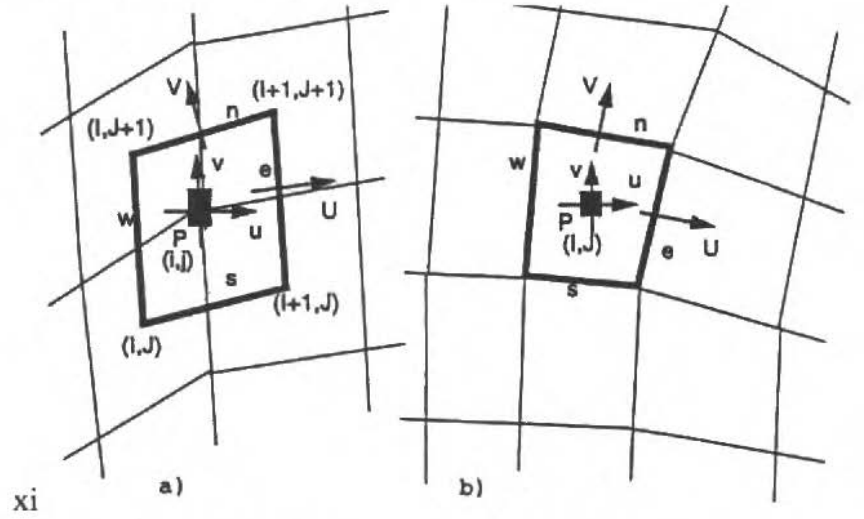

Fig. 1 Node-Centered and Cell-Centered Arrangements: a) Node-Centered, b) Cell-Centered

where U and V in Fig. 1 are the contravariant velocity components.

The finite volume discretization based on the central averaging is not dissipative (Kroll and Jain, 1987). The numerical procedure does not converge to the steady state solution when the high frequency oscillations in the solution are not damped. The dissipative vector $\vec{D}_{i,j,k}$ is introduced by adding dissipative fluxes (Jameson et al, 1981) (Radespiel, 1989) as follows

$$\frac{\partial \vec{W}_{i,j,k}}{\partial t} + \frac{1}{V_{i,j,k}}[\vec{Q}_{i,j,k} - \vec{D}_{i,j,k}] = 0 \tag{8}$$

This dissipation operator is a blend of second and fourth differences and is defined according to (Radespiel, 1989)

$$\vec{D}_{i,j,k} = d_{i+1/2,j,k} - d_{i-1/2,j,k} + d_{i,j+1/2,k} - d_{i,j-1/2,k} + d_{i,j,k+1/2} - d_{i,j,k-1/2} \tag{9}$$

whose dissipation coefficient is given by

$$d_{i+1/2,j,k} = \alpha_{i+1/2,j,k}\{\varepsilon^{(2)}_{i+1/2,j,k}\delta_x \vec{W}_{i,j,k} - \varepsilon^{(4)}_{i+1/2,j,k}\delta_{xxx}\vec{W}_{i-1,j,k}\} \tag{10}$$

The difference operators of first and third order are δ_x and δ_{xxx}, respectively, and α is the scaling factor, which is written for the i direction as (Blazek, 1994)

$$\alpha_{i+1/2,j,k} = \frac{1}{2}(\lambda^{i*}_{i,j,k} + \lambda^{i*}_{i+1,j,k}) \tag{11}$$

where λ is the cell spectral radius for the i (λ^i) and j (λ^j) directions, respectively. The spectral radius is modified as follows

$$\lambda^{l*}_{i,j,k} = \lambda^{l}_{i,j,k}\phi^{l}_{i,j,k} \tag{12}$$

$$\phi^{l}_{i,j,k} = 1 + max\left[\left(\frac{\lambda^{j}_{i,j,k}}{\lambda^{l}_{i,j,k}}\right)^{w}, \left(\frac{\lambda^{k}_{i,j,k}}{\lambda^{l}_{i,j,k}}\right)^{w}\right] \tag{13}$$

and w is chosen as ($0 \le w \le 0.667$). The coefficients adapted to the local pressure gradients $\varepsilon^{(2)}$ and $\varepsilon^{(4)}$ can be cast into the form (Radespiel, 1989)

$$\varepsilon^{(2)}_{i+1/2,j,k} = k^{(2)} max(\upsilon_{i+2,j,k}, \upsilon_{i+1,j,k}, \upsilon_{i,j,k}, \upsilon_{i-1,j,k}) \tag{14}$$

$$\varepsilon^{(4)}_{i+1/2,j,k} = max(0, k^{(4)} - \varepsilon^{(2)}_{i+1/2,j,k}) \tag{15}$$

where

$$\upsilon_{i,j,k} = \left|\frac{p_{i+1,j,k} - 2p_{i,j,k} + p_{i-1,j,k}}{p_{i+1,j,k} + 2p_{i,j,k} + p_{i-1,j,k}}\right| \tag{16}$$

and

$$0.5 \le k^{(2)} \le 0.6\,, \qquad \frac{1}{128} \le k^{(4)} \le \frac{1}{48} \tag{17}$$

Time-Stepping and Acceleration Techniques

In order to obtain numerical solutions of high accuracy, the Runge-Kutta (Kroll and Jain, 1987) (Blazek, 1994) method is chosen, which is characterised by its low operation count. More than two stages are used in order to extend the stability region. The classical fourth order Runge-Kutta method requires the evaluation of many coefficients and dissipative terms, what leads to storage problems. Therefore, the following multistage scheme, which requires few computational storage, is employed (Kroll and Jain, 1987).

$$\begin{aligned}
\vec{W}^{(0)}_{i,j,k} &= \vec{W}^{(n)}_{i,j,k} \\
\vec{W}^{(r)}_{i,j,k} &= \vec{W}^{(0)}_{i,j,k} - \frac{\alpha_r \Delta_t}{V_{i,j,k}} \vec{R}^{(r-1)}_{i,j,k} \\
\vec{W}^{(n+1)}_{i,j,k} &= \vec{W}^{(r)}_{i,j,k}
\end{aligned} \tag{18}$$

where

$$\vec{R}^{(r)}_{i,j,k} = \vec{Q}^{(r)}_{i,j,k} - \vec{D}^{(r)}_{i,j,k}, \qquad r = 0,1,2,\Lambda\,,m \tag{19}$$

An efficient 5-stage scheme is given by the following coefficients (Jameson et al, 1981)

$$\alpha_1 = \frac{1}{4}, \qquad \alpha_2 = \frac{1}{6}, \qquad \alpha_3 = \frac{3}{8}, \qquad \alpha_4 = \frac{1}{2}, \qquad \alpha_5 = 1 \tag{20}$$

For the general case of a non uniform mesh the time condition for a cell is written as (Blazek, 1994)

$$\Delta t_{i,j,k} = CFL \frac{V_{i,j,k}}{\lambda^{i}_{i,j,k} + \lambda^{j}_{i,j,k} + \lambda^{k}_{i,j,k}} \tag{21}$$

The need of efficient methods to solve viscous and non viscous flow problems is obvious. Many solvers, still in use today, exhibit slow convergence to obtain the solution, which leads to high design costs. In order to efficiently solve flow problems with require fine grids, techniques to accelerate the convergence are employed. Some of these approaches, namely the local time-stepping, residual averaging and its combination with multigrid are employed (Radespiel, 1989).

Local time-stepping allows to obtain steady state solutions with less computational effort. It is equivalent to preconditioning the residual by a scalar value in each cell. It can reduce the computational time needed to obtain steady state solutions by an order of magnitude. A weighted average of residuals is employed to increase the Courant-Friedrichs-Lewy number of an explicit multistage scheme. In this way the residuals are replaced by an average of neighbouring residuals (Kroll and Jain, 1987).

The slow asymptotic convergence behaviour of numerical methods is associated to the smooth error components. The good smoothing properties of the Runge-Kutta method, specially of the 5-stage scheme, are very important to be used in a multigrid solver. The success of the multigrid method depends on the use of a relaxation algorithm (Brandt, 1981), which rapidly reduce the high frequency error components. The low error frequencies in fine meshes are transformed in high frequencies in coarse meshes, where they can be better smoothed (Blazek, 1994) (De Bortoli, 1994).

A multiple sequence of grids is efficient because of the following reasons:

- the number of relaxation steps for coarse grids is smaller than for fine grids
- the rate of convergence for coarse grids is faster than for fine grids

The computational procedure to illustrate the FAS (Full Approximation Storage) scheme for two grids is written as follows (Brandt, 1981):

1. Improve the solution on the finest grid

$$\vec{W}_h^{(n+1)} = \vec{W}_h^{(5)} \tag{22}$$

where [(5) = (n+1)] is the last Runge-Kutta time-step for the finest grid.

2. Inject the flow variables from the fine to the coarse grid

$$\vec{W}_{2h}^{(0)} = \vec{W}_h^{(n+1)} \tag{23}$$

3. Transfer the residuals from the fine to the coarse grid

$$f_{2h} = I_h^{2h}\vec{R}_h(\vec{W}_h^{(n+1)}) - \vec{R}_{2h}^{(0)} \tag{24}$$

4. Solve the problem on the coarse grid

$$\vec{W}_{2h}^{(r)} = \vec{W}_{2h}^{(0)} - \alpha_r \frac{\Delta t_{2h}}{V_{2h}}(\vec{R}_h^{(r-1)} + f_{2h}) \tag{25}$$

$$\vec{W}_{2h}^{(n+1)} = \vec{W}_{2h}^{(m)}, \qquad r = 0,1,2,\Lambda\ ,m = 5 \tag{26}$$

5. Interpolate the solution correction from the coarse to the fine mesh

$$\vec{C}_{2h} = \vec{W}_{2h}^{n+1} - \vec{W}_{2h}^{(0)} \tag{27}$$

$$\vec{C}_h = \vec{W}_h^{(5)} - \vec{W}_h^{(0)} + I_{2h}^h\vec{C}_{2h} \tag{28}$$

6. Update the solution on the finest grid

$$\vec{W}_h^{n+1} = \vec{W}_h^{(5)} + I_{2h}^h\vec{C}_{2h} \tag{29}$$

where

$$I_{2h}^h = \frac{1}{4}\begin{bmatrix} 1 & 2 & 1 \\ 2 & 4 & 2 \\ 1 & 2 & 1 \end{bmatrix}, \qquad I_h^{2h} = \frac{1}{16}\begin{bmatrix} 1 & 2 & 1 \\ 2 & 4 & 2 \\ 1 & 2 & 1 \end{bmatrix} \tag{30}$$

For low Mach-numbers difficulties appear to smooth the low frequencies of error (De Bortoli, 1994) and, consequently, to obtain good convergence. This occurs because the eigenvalues of the compressible equations are very different when the Mach-number goes to zero. To alleviate this problem more work is done in the coarse meshes, using a W- multigrid cycle with two steps at each grid.

Numerical Results

In the following, numerical results for a three dimensional channel and the NACA 0012 airfoil are presented and compared with potential (analytical) solutions or experimental data (Blazek, 1994). One way of proving the validity of the numerical Euler solutions is to compare them with potential solutions (Schlichting and Truckenbrodt, 1959). Numerical solutions are related to the free stream Mach-number based on the non dimensional variables

$$\overline{p} = \frac{p}{p_\infty}, \qquad \overline{T} = \frac{T}{T_\infty}, \qquad \overline{\rho} = \frac{\rho}{\rho_\infty}$$

First computations were performed for channel submitted to incompressible flow. A channel is chosen because of its geometrical simplicity and because it represents a class of incompressible internal flow problems. The boundary conditions are far field at the inflow and outflow boundaries (Whitfield, 1983). The approach of Whithfield (1983) is based on the characteristic form of the one dimensional Euler equations normal to the boundary. Numerical conditions imposed on the outer boundary should assure that the outgoing waves are not reflected back into the flow field. At solid walls the slip condition is employed.

Figure 2 shows the computational grid used which contains 36x6x6 cells. Figure 3 shows the Mach contours computed for inflow Mach-number 0.05 (cylindrical part). These solutions are in agreement with the expected solution that the constant Mach lines remain in the channel reduction. The corresponding velocity vector distribution is presented in Fig. 4. It can be seen that velocity increases with the duct reduction, for incompressible flows. Besides the solution is symmetric related to y and z axis.

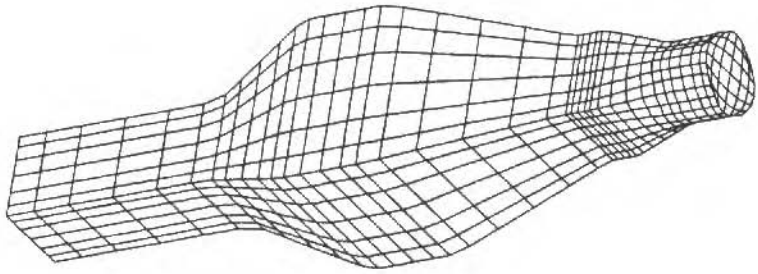

Fig. 2 Grid for Channel, 36x6x6 Cells

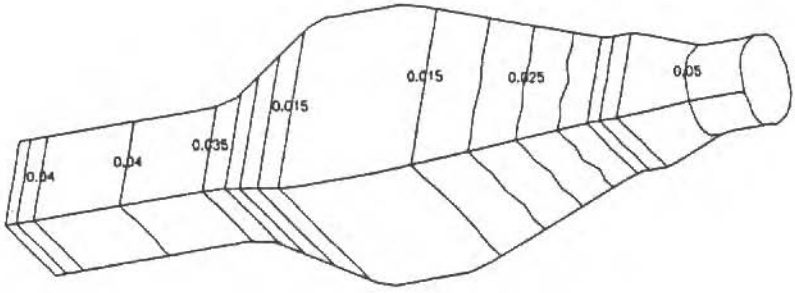

Fig. 3 Mach Contours for Channel, Mach = 0.05

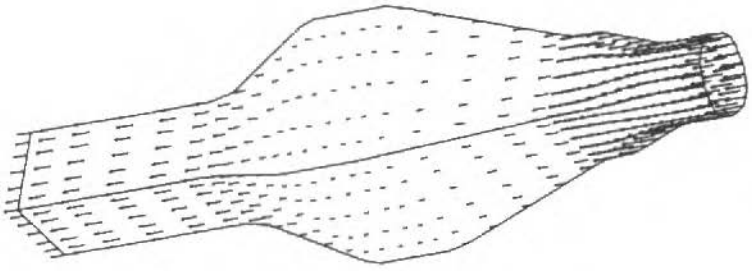

Fig. 4 Velocity Vectors for Channel, Mach = 0.05 (Euler)

In the following, compressible and incompressible flows over the NACA 0012 airfoil are presented and compared. Results were obtained using a C-grid topology which consists of 256x64 cells, as presented in Fig. 5. Numerical tests are related to the free stream Mach-number based on the non dimensional variables. The position of the outer boundary is around twenty chord lengths away from the airfoil and the far field boundary condition is modified due to a vortex (Usab and Murman, 1983). Five grids and a W-multigrid cycle (Brandt, 1981) were used in the multigrid process (256x64, 128x32, 64x16, 32x8 and 16x4 cells).

Although there is a circulation around the lifting bodies, the far field boundary condition employed assumes zero circulation (Whithfield, 1983). Therefore, the boundaries have to be placed sufficiently far away from the airfoil, so that the flow field remains undisturbed. Although the far field potential is strictly valid in subsonic flows, the correction of the free stream conditions is applied in transonic flows and has been proved to be helpful in this flow regime also.

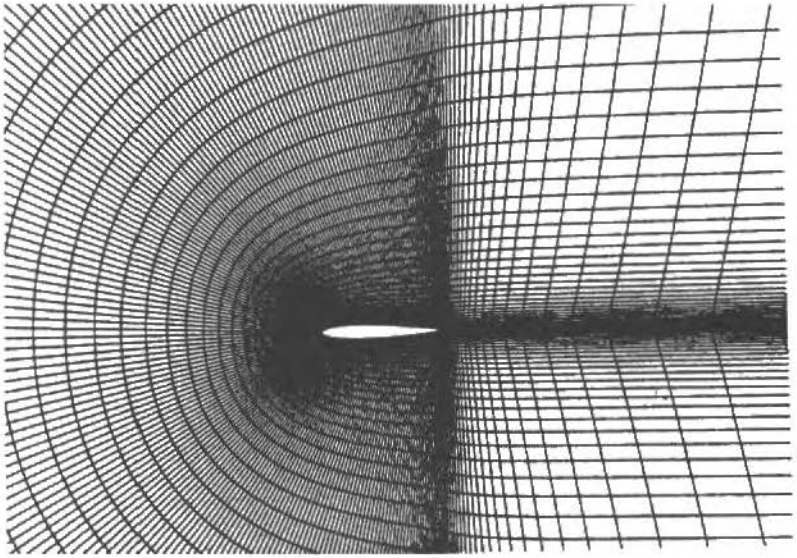

Fig. 5 Grid for NACA 0012, 256x64 cells

Figure 6 shows the pressure contours computed for Mach = 0.63 and angle of attack $\alpha = 2°$. Figure 7 shows the pressure coefficient computed for Mach = 0.63 and $\alpha = 2°$. The numerical solutions obtained for compressible and incompressible flows are in good agreement with the potential solutions or experimental data (Kroll and Jain, 1987).

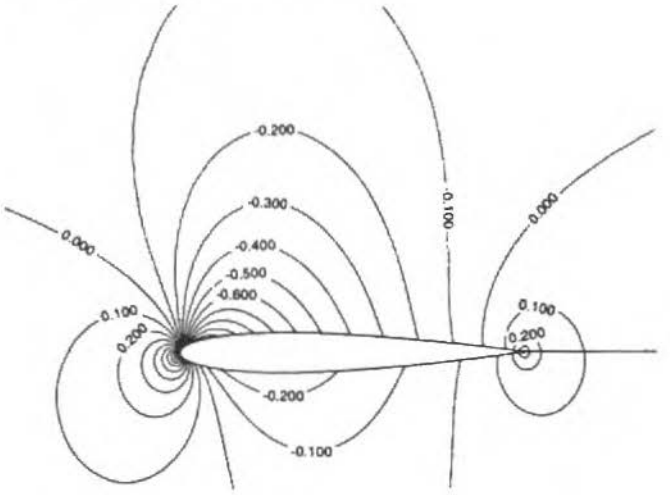

Fig. 6 Pressure Contours for NACA 0012, Mach = 0.63 and $\alpha = 2°$

Figure 8 shows the pressure coefficient computed for Mach 0.005 and $\alpha = 5°$ (incompressible flow). The convergence history computed for Mach = 0.1 with one and two steps at each grid (multigrid) is presented in Fig. 9. Figure 10 compares the convergence history for Mach = 0.1 with and without the use of multigrid techniques. Finally, Fig. 11 shows the pressure contours computed for Mach 0.8, $\alpha = 1.25°$.

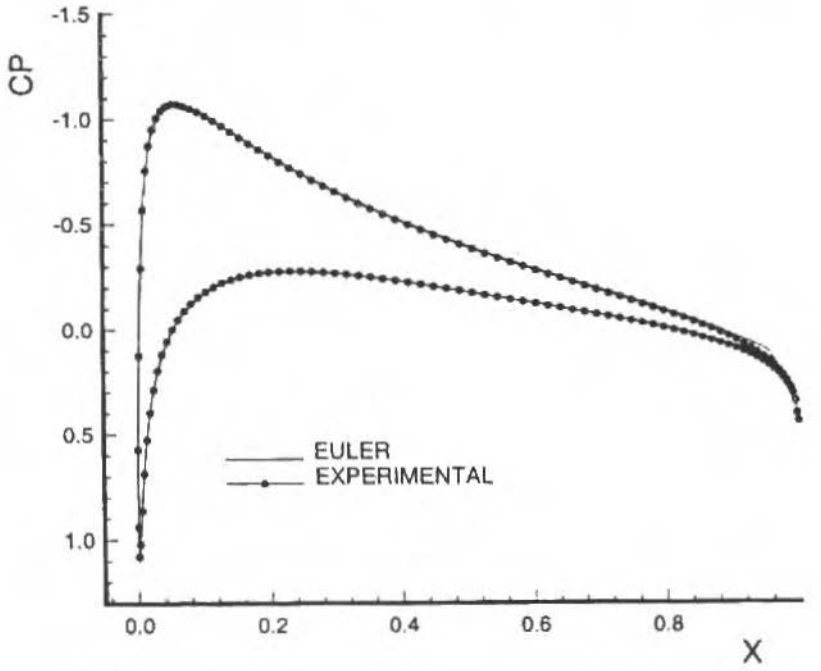

Fig. 7 Pressure Coefficient for NACA 0012, Mach = 0.63 and $\alpha = 2°$

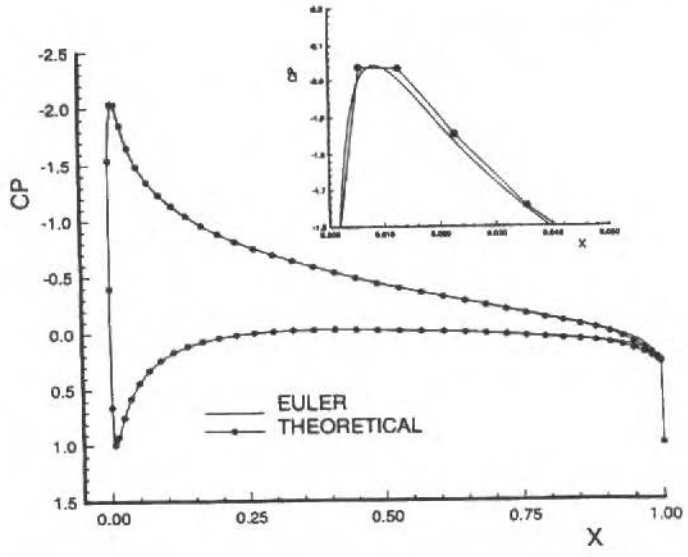

Fig. 8 Pressure Coefficient for NACA 0012, Mach = 0.005 and α = 5° (with an amplification)

Comparisons of the pressure coefficient for the NACA 0012 airfoil showed differences that are lower than 1%. The pressure coefficient for the Euler equations for incompressible flows is compared with the conforming mapping solution (Blazek, 1994). Besides, they were obtained with approximatly 300 time-steps for a convergence criterion $\varepsilon = 10^{-4}$ (De Bortoli, 1994). The convergence behaviour of this method for compressible flows can be easily found in the literature (Kroll and Jain, 1987) (Radespiel, 1989). Numerical solutions for these situations are obtained with as much as 200 time-steps (Blazek, 1994) (De Bortoli, 1994).

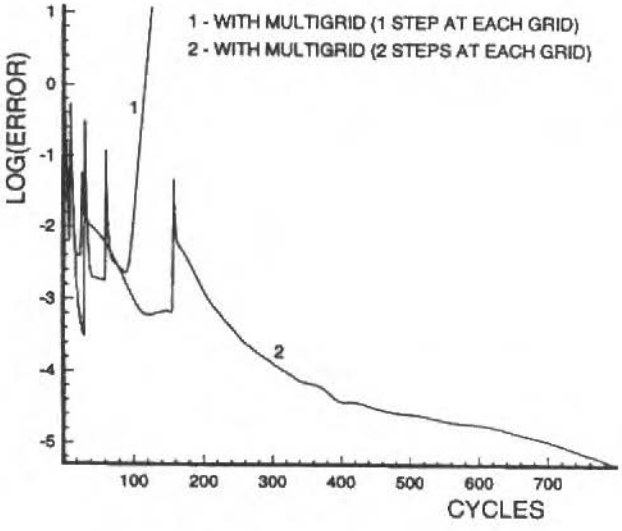

Fig. 9 Convergence Histories for NACA 0012 for Mach = 0.1 With Multigrid

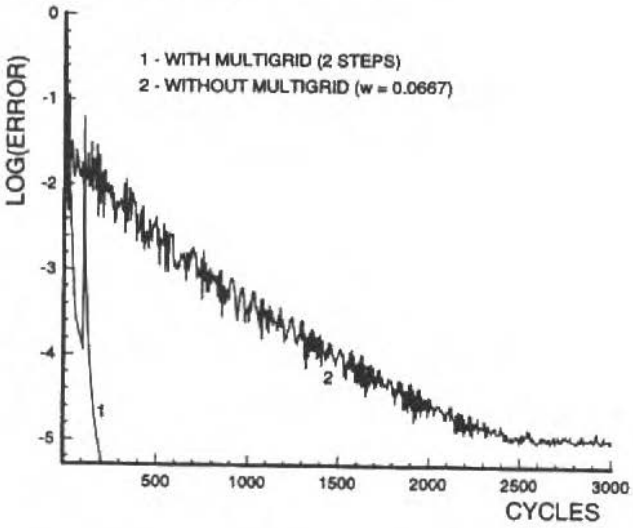

Fig. 10 Convergence History for NACA 0012 With and Without Multigrid Techniques, Mach =0.1

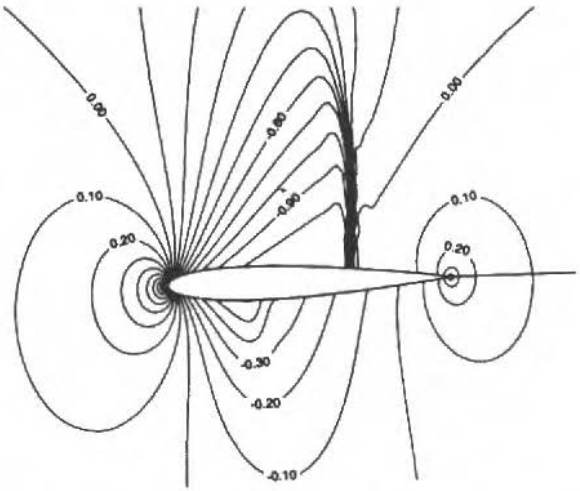

Fig. 11 Pressure Contours for NACA 0012 , Mach = 0.8 and α = 1.25°

These results indicate that the present method can be employed to efficiently solve compressible and incompressible fluid flows. The numerical solutions obtained using the preconditioning method are in good agreement with the theoretical solutions.

Conclusions

The finite volume spatial discretization and the Runge-Kutta time-stepping scheme are used to solve compressible as well as incompressible flow problems. Extension of a compressible code (Blazek, 1994), based on the node-centered/cell-centered arrangements, to solve incompressible flows is presented and compared for channel and the NACA 0012 airfoil. Accuracy and reliability of the code

have been tested in computing subsonic and transonic flows around airfoils. Since explicit time-stepping schemes are used, the solution algorithm is obviously vectorizable. Besides, extensive numerical tests have shown that transonic flows can be well predicted if the dissipative terms are carefully controlled.

Special care has been taken on the treatment of influence coefficients used to obtain the time-step, the artificial dissipation and to evaluate the boundary conditions (Choi and Merkle, 1985). The far field boundary condition proved to be helpful not only to solve the flow about airfoils, but also for the channel (tunnel). Additional modification have been done in the boundary conditions. The use of a vortex at the far field helps to use small domains (with approximatly 20 chord lengths) for airfoils.

The convergence to the steady state is accelerated using local time-stepping, residual averaging and multigrid. With these acceleration techniques the solution of the two-dimensional Euler equations can be obtained in few seconds on today supercomputers for sufficient accuracy (Brandt, 1981). However, for low Mach flows the efficiency of this technique was not so big as for transonic flows presented by Blazek (1994). The experience also indicates that it is important to employ the W-multigrid cycle for small speed flows, probably because more work is done in the coarse meshes.

The convergence behaviour of numerical methods is often sensitive to the application of boundary conditions, grid aspect ratio (Buelow et al., 1994) and flow regime. However, the preconditioning employed is applicable not only to incompressible flows, but also to compressible flows with incompressible regions. Such a method allows to get a goal of compressible and incompressible solution of fluid flows. Besides, the preconditioning system has a rate of convergence almost independent from the Mach-number.

The comparison between the theoretical and numerical solutions is encouraging. Specially the use of multigrid techniques and its combination with preconditioning present good convergence rates. Therefore, the same code can be employed to solve compressible as well as incompressible flow problems. Besides, second order solutions are obtained, which are indispensable to analyse the aerodynamic problems of interest. However, a lot of work must still be done. Extensions to three dimensional problems over complex geometries such as wings, launch vehicles and cars are currently under way.

Acknowledgement

This work was supported by DAAD and carried out at the DLR Institute of Design Aerodynamics in Braunschweig. The author is grateful to DAAD for this support and to DLR for this opportunity. The author gratefully acknowledges numerous discussions with Dr. J. Blazek and Dr. N. Kroll during this work. The work is now being supported by CNPq.

References

Blazek, J., 1994, "Verfahren zur Beschleunigung der Lösung der Euler- und Navier-Stokes Gleichungen bei Stationären Über- und Hyperschallströmungen", Ph.D. Thesis, University of Braunschweig.

Buellow, P.E.O, Venkateswaren, S., and Merkle, C.L., 1994, "Effect of Grid Aspect Ratio on Convergence", AIAA Journal, Vol. 32, Nr. 12.

Brandt, A., 1981, "Guide to Multigrid Development", Multigrid Methods I, Lecture Notes in Mathematics.

Choi, D., and Merkle, C.L., 1985, "Application of Time-Iterative Schemes to Incompressible Flow", AIAA Journal, Vol. 23, Nr. 10, pp. 1518-1524.

Choi, Y. H., and Merkle, C. L., 1993, "The Application of Preconditioning in Viscous Flows", Journal of Computational Physics 105, 1993, pp. 207-223.

De Bortoli, A.L., 1994, "Solution of Incompressible Flows Using Compressible Flow Solvers", DLR IB 129-94/18 Relatory, Braunschweig, Germany.

Jameson, A., Schmidt, W., and Turkel, E., 1981, "Numerical Solution of the Euler Equations by FiniteVolume Methods Using Runge-Kutta Time-Stepping Schemes", AIAA Paper 81-1259.

Jameson, A., 1985, "Multigrid Algorithm for Compressible Flow Calculations", Multigrid Methods, Cologne.

Karki, K.C., and Patankar, S.V., 1989, "Pressure Based Calculation Procedure for Viscous Flows at All Speeds in Arbitrary Configurations", AIAA Journal, Vol. 27, Nr. 9, pp. 1167-1174.

Kroll, N., and Jain, R. K., 1987, "Solution of Two-Dimensional Euler Equations - Experience with a Finite Volume Code", Forschungsbericht, DFVLR-FB 87-41 Relatory, Braunschweig, Germany.

Patankar, S.V., 1981, "Numerical Heat Transfer and Fluid Flow", McGraw-Hill, New York.

Raithby, G. D., and Schneider, G. E., 1979, "Numerical Solution of Problems in Incompressible Flow: Treatment of Velocity-Pressure Coupling", Numerical Heat Transfer, Vol. 2, pp. 417-440.

Radespiel, R., 1989, "A Cell-Vertex Multigrid Method for the Navier-Stokes Equations", NASA Technical Memorandum 101557.

Schlichting, H.,and Truckenbrodt, E., 1959, "Aerodynamik des Flugzeuges - Teil I", Springer-Verlag, Berlin.

Turkel, E., 1992, "Review of Preconditioning Methods for Fluid Dynamics", NASA Report 189712, ICASE Report Nr. 92-47.

Usab, W. J., and Murman, E. M., 1983, "Embedded Mesh Solution of the Euler Equation Using Flux Vector Splitting", MS 39762, Mississippi State University, USA.

Whitfield, D. L., 1983, "Three-Dimensional Unsteady Euler Equation Solutions Using Flux Vector Splitting", MS 39762, Mississippi State University, USA.

RBCM - J. of the Braz. Soc. Mechanical Sciences
Vol. XIX - No.3 - 1997 - pp. 371-391

ISSN 0100-7386
Printed in Brazil

A Unified Finite-Volume Finite-Differencing Exponential-Type Scheme for Convective-Diffusive Fluid Transport Equations

José Ricardo Figueiredo
UNICAMP - Universidade Estadual de Campinas
Faculdade de Engenharia Mecânica
Departamento de Energia
13083-970 Campinas, SP Brasil

Abstract

This paper presents a new discretization scheme for the convective-diffusive transport equation of heat, mass or momentum in fluid media, constructed within the control-volume approach for both regular or irregularly spaced rectangular meshes. The present scheme shares with others, such as LOADS and Flux-Spline, the kind of exponential interpolating curve, obtained as the exact solution of an approximated equation that admits a so called source term. To compute this term the present scheme incorporates Allen's finite difference approach into the finite volume method. The resulting procedure was called Unified Finite Approach Exponential-Based Scheme, UNIFAES. It is a conservative form scheme much simpler than both LOADS and Flux-Spline. The scheme is submitted to a series of tests in the linear problem of convection and diffusion of a scalar in a parallel flow, where it is compared to the central differencing, to the exponential scheme and to LOADS, showing excellent accuracy for all function types and unconditional stability for all Peclet numbers.
Keywords: *Convective-Diffusive Transport, CFD, UNIFAES, Finite Difference, Finite Volume.*

Introduction

This paper describes a discretization scheme for the convective-diffusive transport equations of heat, mass or momentum in fluid media, constructed within the control-volume approach for both regular or irregularly spaced rectangular meshes. The scheme presented here shares with some new schemes, such as LOADS and Flux-Spline, the kind of exponential interpolating curve, which is obtained as the exact solution of an approximated equation that admits a so called source term. In the present scheme the source term of the generating equation is computed with recourse to Allen's methodology (Allen and Southwell, 1955; Allen, 1962), so incorporating a finite difference approach into the finite volume method.

For simplicity, the scheme will be derived with respect to the two-dimensional thermal transport equation with constant thermophysical properties:

$$\frac{\partial(\rho c\phi)}{\partial t}+\frac{\partial(\rho c u\phi)}{\partial x}+\frac{\partial(\rho c v\phi)}{\partial y}-\frac{\partial}{\partial x}(\Gamma\frac{\partial\phi}{\partial x})-\frac{\partial}{\partial y}(\Gamma\frac{\partial\phi}{\partial y}) = S \qquad (1)$$

where ϕ is the temperature, t is time, ρ is the fluid density, u and v are respectively the x and y directions velocity components, Γ is the thermal conductivity, c is the specific heat and S is an eventual source term such as some form of energy dissipation into heat, or generation or consumption of heat in a chemically reacting flow.

The well known analogies between this equation and other convective-diffusive transport equations for species concentration, linear or angular momentum, turbulent kinetic energy and turbulent dissipation rate make possible the use of the scheme for such equations as well. The easy with which the finite-volume method copes with irregular coefficients also assures wider uses for the scheme.

The equation is put in non-dimensional form by dividing the spatial coordinates by a characteristic dimension L and the velocity components by a characteristic velocity V, without notational changes, leading to:

Manuscript received: September 1996. Technical Editor: Carlos Alberto Carrasco Altemani

$$\frac{\partial \phi}{\partial t} + \frac{\partial (Pe.u.\phi)}{\partial x} + \frac{\partial (Pe.v.\phi)}{\partial y} - \frac{\partial^2 \phi}{\partial x^2} - \frac{\partial^2 \phi}{\partial y^2} = S \qquad (2)$$

where Pe is the global Peclet number $Pe = \rho.V.L.c/\Gamma$. Variable t now represents the non-dimensional time, given by the dimensional time multiplied by $\Gamma/(\rho.c.L^2)$, and S stands for the non-dimensional source term, given by the dimensional source term multiplied by L^2/Γ .

Derivation of Proposed Scheme

Control-Volume Exponential-Based Schemes

Integrating Eq. (2) on the cell area (Fig. 1) and employing the divergence theorem, according to the control volume methodology, one obtains:

$$\delta x.\delta y.\frac{\partial \phi}{\partial t} + (J_e - J_w).\delta y + (J_n - J_s).\delta x = S.\delta x.\delta y \qquad (3)$$

where J_e is the combined convective and diffusive flux at cell boundary e:

$$J_e = Pe.u_e.\phi_e - \left.\frac{\partial \phi}{\partial x}\right|_e \qquad (4)$$

and so on for the other cell boundaries.

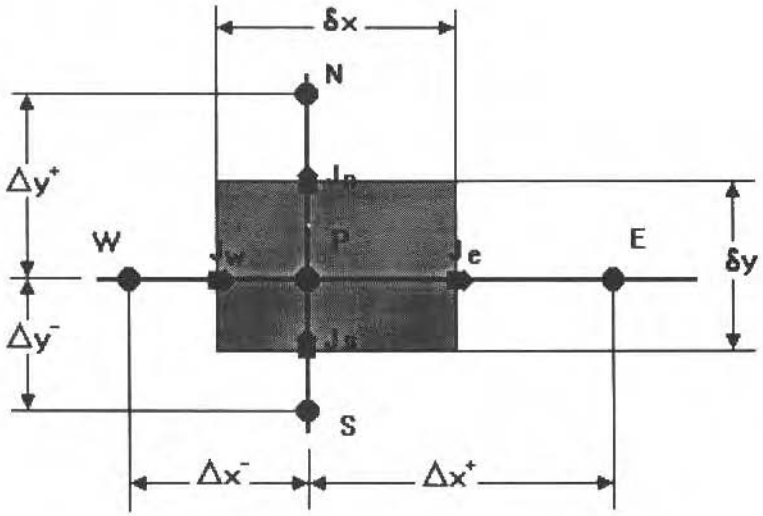

Fig. 1 Two-Dimensional Sketch for Finite Volume Discretization

The exponential-based schemes for the discretization of the spatial derivatives in each direction, say the x direction, are built upon an interpolating curve obtained as the exact solution of the one dimensional equation:

$$Pe.u.\frac{d\phi}{dx} - \frac{d^2\phi}{dx^2} = K_x \tag{5}$$

which approximates Eq. (2) by assuming the velocity component u to be locally constant, as well as the non-homogeneous term K_x , usually referred to as the source term of the generating equation, that represents all the terms of Eq. (2) not included in (5). The general solution to Eq. (5) is:

$$\phi = C_1 + C_2.x + C_3.exp(Pe.u.x) \tag{6.1}$$

where

$$C_2 = \frac{K_x}{Pe.u} \tag{6.2}$$

For the cell boundary e located in the middle point between nodes P and E (Fig. 2) above interpolating curve gives the following values for the function and its derivative:

$$\phi_e = C_1 + C_2.\frac{\Delta x^+}{2} + C_3.exp(Pe.u.\frac{\Delta x^+}{2}) \tag{6.3}$$

$$\left.\frac{d\phi}{dx}\right|_e = C_2 + C_3.Pe.u.exp(Pe.u.\frac{\Delta x^+}{2}) \tag{6.4}$$

$$J_e = Pe.u.C_1 + C_2.\left(Pe.u.\frac{\Delta x^+}{2} - 1\right) \tag{6.5}$$

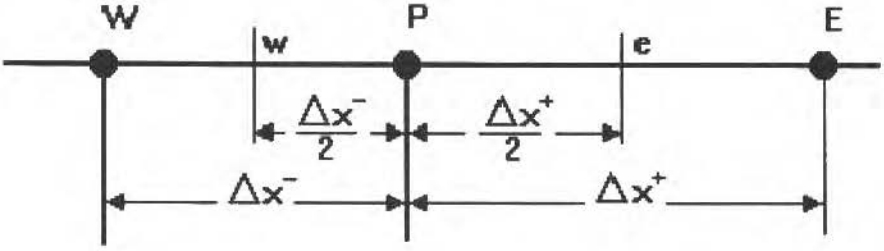

Fig. 2 One-Dimesional Sketch for Finite Volume and Finite Difference Discretizations

so that the combined convective-diffusive flux at cell boundary e , given in expression (4), becomes:

Adjusting the interpolating profile (6.1) to nodes P and E one forms the system:

$$\phi_P = C_1 + C_3 \tag{7.1}$$

$$\phi_E = C_1 + C_2.\Delta x^+ + C_3.exp(Pe.u.\Delta x^+) \tag{7.2}$$

that can be solved for C_1 leading to:

$$C_1 = \phi_P - \frac{\phi_E - \phi_P}{exp(Pe.u_e.\Delta x^+) - 1} + \frac{C_2.\Delta x^+}{exp(Pe.u_e.\Delta x^+) - 1} \tag{7.3}$$

Substituting (7.3) into (6.5), then employing (6.2), the combined convective and diffusive flux at cell boundary e becomes:

$$\begin{aligned} J_e = {} & Pe.u_e.\phi_P + \frac{\phi_P - \phi_E}{\Delta x^+}\frac{Pe.u_e.\Delta x^+}{exp(Pe.u_e.\Delta x^+) - 1} + \\ & + K_e.\Delta x^+.\left[\frac{1}{exp(Pe.u_e.\Delta x^+) - 1} - \frac{1}{Pe.u_e.\Delta x^+} + \frac{1}{2}\right] \end{aligned} \tag{7.4}$$

The other cell boundaries fluxes are obtained analogously and substituted, together with (7.4), into Eq. (3). After the cancellation of term $Pe.[(u_e - u_w).\delta y + (v_n - v_s).\delta x].\phi_P$ due to the continuity equation, the resulting difference equation is:

$$\begin{aligned} & \delta x.\delta y.\frac{\partial \phi}{\partial t} + (\phi_P - \phi_E).\pi(p_e).\frac{\delta y}{\Delta x^+} + (\phi_P - \phi_W).\pi(-p_w).\frac{\delta y}{\Delta x^-} + \\ & (\phi_P - \phi_N).\pi(p_n).\frac{\delta x}{\Delta y^+} + (\phi_P - \phi_S).\pi(-p_s).\frac{\delta x}{\Delta y^-} = S.\delta x.\delta y - \Psi \end{aligned} \tag{8.1}$$

where

$$p_e = Pe.u_e.\Delta x^+ \tag{8.2}$$

$$p_w = Pe.u_w.\Delta x^- \tag{8.3}$$

$$p_n = Pe.v_n.\Delta y^+ \tag{8.4}$$

$$p_s = Pe.v_s.\Delta x^- \tag{8.5}$$

$$\pi(p) = \frac{p}{exp(p) - 1} \tag{8.6}$$

$$\Psi = \left[K_e \Delta x^+ \chi(p_e) - K_w \Delta x^- \chi(p_w)\right] \delta y + \left[K_n \Delta y^+ \chi(p_n) - K_s \Delta y^- \chi(p_s)\right] \delta x \tag{8.7}$$

$$\chi(p) = \frac{1}{exp(p)-1} - \frac{1}{p} + \frac{1}{2} = \frac{\pi(p)-1}{p} + \frac{1}{2} \tag{8.8}$$

The functions π and χ of the cell Peclet number p are monotone, smooth varying functions for all real Peclet numbers. However, their algebraic forms present limitations. When the cell Peclet number vanishes above forms lead to indeterminacy and at very low Peclet some precision is lost on the division between too very small differences. The practice followed by this author is to represent them by a third or fourth order series about the origin for cell Peclet numbers lower than 0.01. On the other extreme, when the cell Peclet exceeds the admissible range of arguments for the computer exponentials, the function π is computed according to its limits: $lim\ \pi_{p\to+\infty} = 0$ and $lim\ \pi_{p\to-\infty} = -p$, and the function χ tends naturally to its limit according to the last expression in (8.8): $lim\ \chi_{p\to+\infty} = 0.5$ and $lim\ \chi_{p\to-\infty} = -0.5$.

All generating equation's source terms K are included in the deferred correction term Ψ so that they can be introduced, with relative easy, in the algorithms for the solution of transport equations originally based on five-node schemes.

Existing Forms to Compute the Source Term of the Generating Equation

The first divergent-form exponential and correlated schemes, such as Spalding's (1972) hybrid approximation to the exponential, and Raithby and Torrance's (1974) upstream-weighted scheme, assumed null K_x .

Wong and Raithby's LOADS (1979) was the first control-volume exponential-type scheme to take the source terms into account, computing them according to the meaning with which they were introduced in the generating equation, as can be seen by comparing Eqs. (2) and (5):

$$K_x = S - \left(\frac{\partial \phi}{\partial t} + Pe.v.\frac{\partial \phi}{\partial y} - \frac{\partial^2 \phi}{\partial y^2}\right) \tag{9.1}$$

For the computation of K_e (Fig. 3) one would have:

$$S = \frac{S_{i,j} + S_{i+1,j}}{2} \tag{9.2}$$

$$\frac{\partial \phi}{\partial t} = \frac{\left.\frac{\partial \phi}{\partial t}\right|_{i,j} + \left.\frac{\partial \phi}{\partial t}\right|_{i+1,j}}{2} \tag{9.3}$$

$$Pe.v.\frac{\partial \phi}{\partial y} - \frac{\partial^2 \phi}{\partial y^2} = \frac{\left(J_n - J_s\right) + \left(J_{ne} - J_{se}\right)}{2} \tag{9.4}$$

proceeding analogously for the terms K of the other directions.

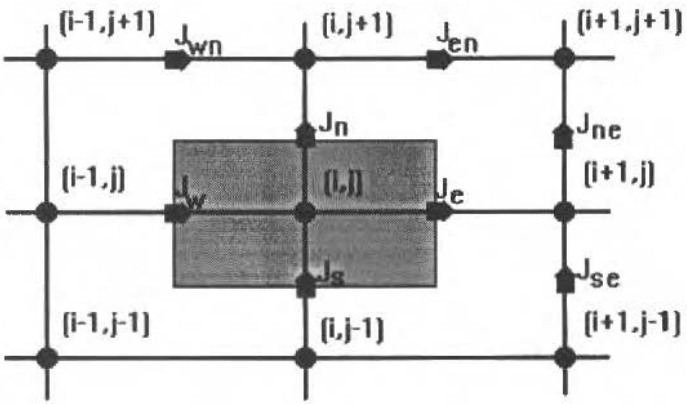

Fig. 3 Computational Molecule for LOADS

The computation of the convective and diffusive cross-fluxes in (9.4) is done by means of the simple divergent-form exponential scheme, where the terms K are neglected. Terms of kind $P e.v.\phi$, appearing in the computation of each J, are not automatically canceled as before Eqs. (8), being generally canceled as a further approximation.

A particular difficulty relates to the transient case where, as can be seen from (9.3), transient terms of point *(i+1,j)* , as well *(i-1,j)*, *(i,j+1)* and *(i,j-1)*, appear in the equation for point *(i,j)*. Transient problems are usually avoided in LOADS literature.

A similar rationale inspired the scheme due to Ulson de Souza (1992), which was presented as an extension of Raithby and Torrance's weighted-upstream differencing scheme, receiving the acronym WUDS-E. It differs from LOADS with regard to the scheme employed in computing the generating equation's source terms, namely central differencing instead of the simple exponential scheme, and was further extended to adaptive irregular grids.

Although conceptually similar, the derivation of the Flux-Spline (Varejão,1979, Nieckele,1985; Karki et al, 1989, Oliveira, 1997) differs from above expressions (6) to (9) by a distinct specification of the domain where the interpolating function is defined, with a corresponding change of the local axis.

The computation of terms K is done in the Flux-Spline discretization through the requirement that the combined convective-diffusive fluxes J are continuous between neighbouring cells, what is achieved through an iterative procedure analogous the algorithm SIMPLER (Patankar, 1980). The Flux-Spline algorithms results considerably more complicated than both five-node schemes and LOADS.

Extended Allen's Methodology

The complete generating Eq. (5) was used for the first time by Allen and Southwell scheme (1955), which was idealized in the finite-difference approach as a means of directly obtaining a numerical representation of the combined first and second derivatives for each direction in the transport equation, taken in its non-conservative form. The scheme was originally designed for regularly spaced grids. The extension to irregular grids will be presented first, followed by the application of this result within the control volume method.

By adjusting the interpolating curve (6.1) to the three neighbour nodes W , P and E one forms the system:

$$\phi_W = C_1 - C_2.\Delta x^- + C_3.exp(-Pe.u.\Delta x^-) \tag{10.1}$$

$$\phi_P = C_1 + C_3 \tag{10.2}$$

$$\phi_E = C_1 + C_2.\Delta x^+ + C_3.exp(Pe.u.\Delta x^+) \tag{10.3}$$

Solving system (10) for C_2 and employing (6.2) one obtains:

$$Pe.u_P.\frac{\partial \phi}{\partial x} - \frac{\partial^2 \phi}{\partial x^2} = K_x = (\phi_P - \phi_E).\Pi^+ + (\phi_P - \phi_W).\Pi^- \tag{11.1}$$

where

$$\Pi^+ = \frac{Pe.u_P.\left[1 - exp\left(-Pe.u_P.\Delta x^-\right)\right]}{\Delta x^+.\left[exp\left(-Pe.u_P.\Delta x^-\right) - 1\right] + \Delta x^-.\left[exp\left(Pe.u_P.\Delta x^+\right) - 1\right]} \tag{11.2}$$

$$\Pi^- = \frac{Pe.u_P.\left[exp\left(Pe.u_P.\Delta x^+\right) - 1\right]}{\Delta x^+.\left[exp\left(-Pe.u_P.\Delta x^-\right) - 1\right] + \Delta x^-.\left[exp\left(Pe.u_P.\Delta x^+\right) - 1\right]} \tag{11.3}$$

In the regular case, where $\Delta x^+ = \Delta x^- = \Delta x$, these expressions reduce to the original Allen and Southwell's scheme:

$$\Pi^+ = \frac{Pe.u_P.\Delta x}{\Delta x^2.\left[exp\left(Pe.u_P.\Delta x\right) - 1\right]} = \frac{\pi(Pe.u_P.\Delta x)}{\Delta x^2} \tag{11.4}$$

$$\Pi^- = \frac{-Pe.u_P.\Delta x}{\Delta x^2.\left[exp\left(-Pe.u_P.\Delta x\right) - 1\right]} = \frac{\pi(-Pe.u_P.\Delta x)}{\Delta x^2} \tag{11.5}$$

where function π was defined at Eq. (8.6).

Unified Finite Approach Exponential-Based Scheme

It has been seen that, by adjusting the interpolating curve to three mesh nodes, Allen's methodology is capable of determining the finite difference analog of the combined convective-form convective-diffusive derivatives in the direction considered. As expressed in the first equality of (11.1), this finite difference analog is equal to the generating equation's source term K. In the present proposal Allen's

methodology is employed as a means to determine the generating equation's source term K required in the finite volume analog described in the previous item. This procedure, blending finite volume and Allen's finite difference methodologies, received the name Unified Finite Approach Exponential-Based Scheme, and the acronym UNIFAES.

Term Λ_e, for instance, is determined as a mean value between Allen's estimate of Λ_x on nodes (i,j) and $(i+1,j)$:

$$K_e^{i,j} = \alpha . K_x^{i,j} + (1-\alpha) . K_x^{i+1,j} \qquad (12)$$

where each Λ_x is determined according to expressions (11). The arithmetic mean $(\alpha = 0.5)$ is assumed for expression (12). An upwind-form of the scheme can be defined by making $\alpha = 0$ or $\alpha = 1$ in order to privilege the most upwind node in the computation of each cell boundary's source term.

Because of the form the source term of the generating equation, the complete computational molecule for this scheme involves extra nodes on each direction (Fig. 4).

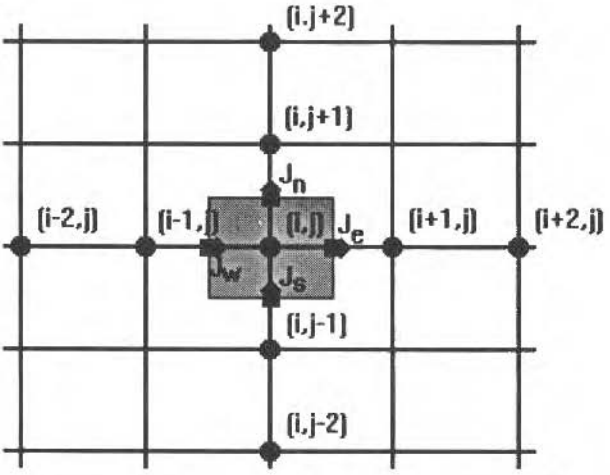

Fig. 4 Computational Molecule for UNIFAES

Although the original Allen and Southwell's scheme is not numerically conservative, the use of Allen's method within the finite volume approach guarantees the conservation since $K_e^{i,j} = K_w^{i+1,j}$, so that $J_e^{i,j} = J_w^{i+1,j}$, and so on for other common boundaries.

Terms K relative to the cell boundaries neighbour to the domain boundary with Dirichlet conditions can not be determined by above mean values since there is no Allen's estimate of K on the frontier. Such value was computed by linear extrapolation from internal nodes.

Uniform Velocity Test Case

The scheme just described was submitted to a series of steady-state linear test cases given by distinct solutions of the transport equation on a constant velocity field defined by modulus V and angle θ with the x-axis, so that its components are $u = V.cos(\theta)$ and $v = V.sin(\theta)$. The exact solutions are

found after writing the equation in terms of coordinates s and n, respectively parallel and normal to the flow directions (Fig. 5), obtaining:

$$Pe.\frac{\partial \phi}{\partial s} - \frac{\partial^2 \phi}{\partial s^2} - \frac{\partial^2 \phi}{\partial n^2} = 0 \qquad (13)$$

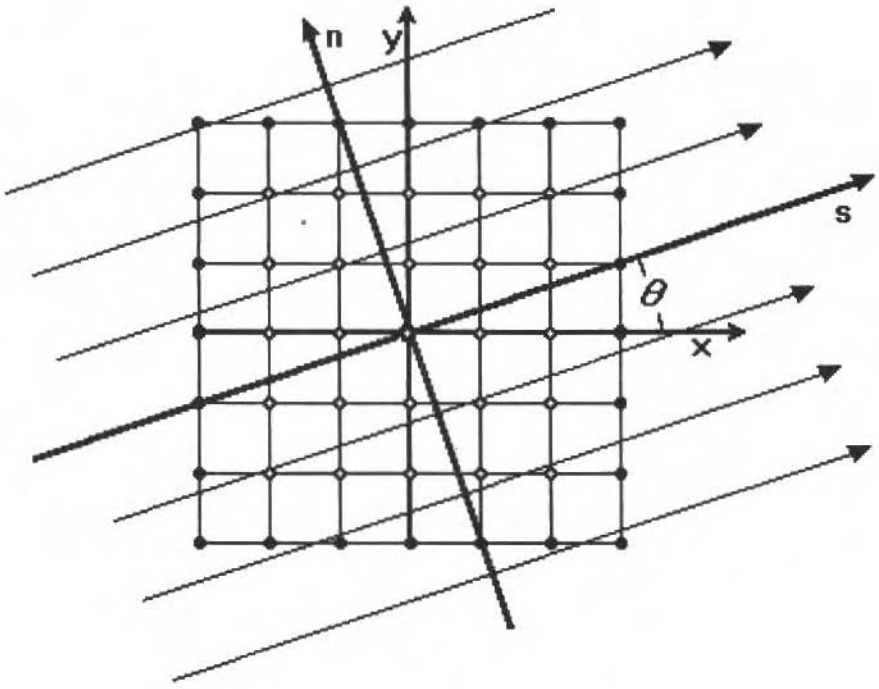

Fig. 5 Exact and Numerical Coordinates

According to the method of separation of variables, a solution of type $\phi = \xi(s).\varsigma(n)$ is initially assumed and substituted into (13) leading to:

$$\frac{Pe.\frac{d\xi}{ds} - \frac{d^2\xi}{ds^2}}{\xi} = \frac{\frac{d^2\varsigma}{dn^2}}{\varsigma} \qquad (14)$$

The above equality can only be satisfied if both members are equal to a real constant, say $\lambda^* = \mu\lambda^2$, leading to the simultaneous ordinary equations:

$$-\frac{d^2\xi}{ds^2} + Pe.\frac{d\xi}{ds} \pm \lambda^2.\xi = 0 \qquad (15.1)$$

$$\frac{d^2\varsigma}{dn^2} \pm \lambda^2.\varsigma = 0 \qquad (15.2)$$

The solutions to the equations above are respectively:

$$\xi = c_1.exp\left(\frac{Pe+\sqrt{Pe^2 \pm 4\lambda^2}}{2}\, s\right) + c_2.exp\left(\frac{Pe-\sqrt{Pe^2 \pm 4\lambda^2}}{2}\, s\right) \qquad (16.1)$$

$$\varsigma = c_3.exp\left[\sqrt{-(\pm 1)}.\lambda.n\right] + c_4.exp\left[-\sqrt{-(\pm 1)}.\lambda.n\right] \qquad (16.2)$$

except for $\lambda = 0$ where function ς can assume a linear form irreducible to (16.2):

$$\varsigma = c_5 + c_6.n \qquad (16.3)$$

Both the discriminants in (16.1) and the arguments of the square roots in (16.2) may be negative, leading to complex exponentials, so that complex coefficients c_1 to c_4 may be required in order to produce real solutions, of sinusoidal type.

Due to the linearity of Eq. (13), other solutions are given by any linear combination of functions $\phi_{\lambda^*} = \xi_{\lambda^*}(s).\varsigma_{\lambda^*}(n)$, where functions $\xi_{\lambda^*}(s)$ and $\varsigma_{\lambda^*}(n)$ are computed according to the appropriate expression within (16). Also, the general solution to (13) could be written as $\phi = \int_{\infty}^{\infty} \phi_{\lambda^*}.d\lambda^*$ assuming that coefficients c_1 to c_4 are complex functions of λ^* .

The linearity of the differential Eq. (13), together with the corresponding linearity of the difference equations that represent it, also assures that the error of any difference scheme for a particular linear combination of functions ψ_{λ^*} will be the corresponding linear combination of the errors of that scheme in functions ϕ_{λ^*} .

Inspired by that, the investigation of the errors of the schemes will be made by submitting them to elementary solutions assuming simple real forms allowed by expressions (16). By varying the kind of solution and the eigenvalue a wide spectrum of possible solutions will be analyzed. Those simple real solutions have the following forms:

For null eigenvalue there is one non trivial solution:

$$\phi_{B0} = exp(Pe.s).n \qquad (17.1)$$

When the eigenvalue is preceded by positive sign in (16.1) and (16.2) there appear solutions on the form:

$$\phi_A = exp\left(\frac{Pe-\sqrt{Pe^2+4\lambda^2}}{2}.s\right).sin(\lambda.n) \qquad (17.2)$$

$$\phi_B = exp\left(\frac{Pe+\sqrt{Pe^2+4\lambda^2}}{2}.s\right).sin(\lambda.n) \qquad (17.3)$$

For eigenvalues preceded by negative sign there are solutions on the form:

$$\phi_C = exp\left(\frac{Pe-\sqrt{Pe^2-4\lambda^2}}{2}.s\right).exp(\lambda.n) \tag{17.4}$$

$$\phi_D = exp\left(\frac{Pe+\sqrt{Pe^2-4\lambda^2}}{2}.s\right).exp(\lambda.n) \tag{17.5}$$

for $\lambda \leq Pe/2$. Above this limit there are solutions of real form:

$$\phi_{CD} = exp\left(\frac{Pe}{2}.s\right).sin\left(\sqrt{\lambda^2-\frac{Pe}{4}}.s\right).exp(\lambda.n) \tag{17.6}$$

$$\phi_{DC} = exp\left(\frac{Pe}{2}.s\right).cos\left(\sqrt{\lambda^2-\frac{Pe}{4}}.s\right).exp(\lambda.n) \tag{17.7}$$

In types A ad B (Eqs. 17.2 and 17.3) there are also solutions with cosines function instead of sinus on the normal direction, and in types C, D, etc. (Eqs. 17.4 to 17.7) there are also solutions with negative instead of positive exponentials on the normal direction. All these alternative solutions have been neglected here for differing from above expressions from a mere shift or inversion of axis.

Results

The above set of exact solutions of the transport equation was used to compare the present scheme with the central differencing, the simple exponential scheme and LOADS. The Flux-Spline was not included because of its complexity.

The exact solution is imposed as Dirichlet condition on the boundary nodes of a square domain with square cells (Fig. 5). Computations employ the transient Alternating Direction Implicit method for five-node schemes, but the source terms of UNIFAES and LOADS are computed explicitly.

For the constant velocity field there is no distinction between convective and divergent form schemes. Because of that and of the regularity of the grid, the Allen and Southwell scheme is entirely coincident with the simple exponential scheme.

Low ratios λ / Pe

Most of the computations to be presented refer to a standard set of parameters given by λ =10 and θ =22.5 degrees ; unless otherwise stated these parameters will be assumed.

Figures (6) to (9) present the profiles of the exact and the numerical schemes' solutions for functions A, B, C and D with Pe=100 in 10x10 spacings grid, showing the most downwind column, where the greatest error occurred.

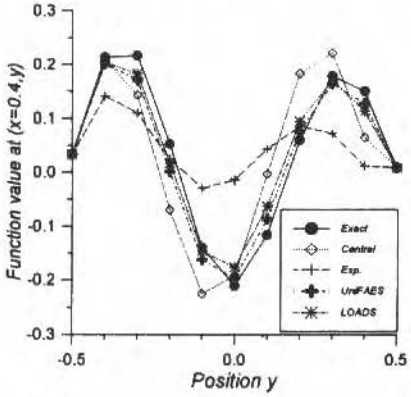

Fig. 6 Exact and Numerical Profiles for Function A at x=0.4, 10x10 grid, Pe=100, λ=10, θ=22.5 Degrees

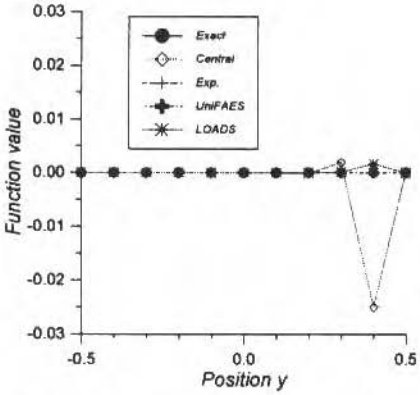

Fig. 7 Exact and Numerical Profiles for Function B at x=0.4, 10x10 grid, Pe=100, λ=10, θ=22.5 Degrees

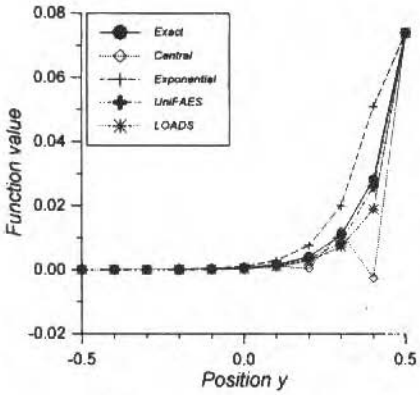

Fig. 8 Exact and Numerical Profiles for Function C at x=0.4, 10x10 grid, Pe=100, λ=10, θ =22.5 Degrees

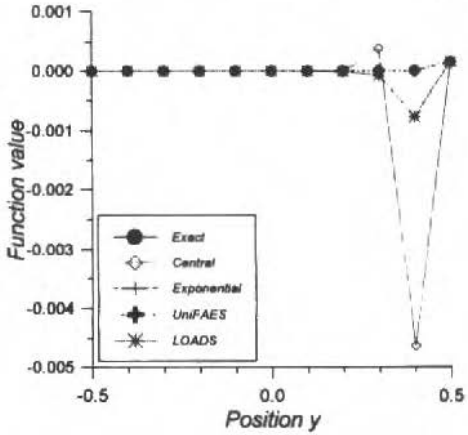

Fig. 9 Exact and Numerical Profiles for Function D at x=0.4, 10x10 grid, Pe=100, λ=10, θ=22.5 Degrees

For such low ratios λ / Pe (=0.1), functions A and C present low derivatives along the stream direction and moderate derivatives in the normal, so that the profiles of the inlet boundary are mainly convected along the stream direction, with low level of diffusion on the cross-flow direction. Meanwhile, functions B and D have very high derivatives on the exit boundary, close to the most downwind node, where there is strong counter-flow diffusion, the function being practically null upwind that boundary region.

Repeating conclusions of many previous studies, the central differencing shows wiggly behaviour, particularly in B and D functions, and the exponential confirms itself as a strongly diffusive scheme in functions A and C, although in functions B and D it has a superb accuracy, visually coinciding with the exact, almost null solution.

Both schemes that employ the generating equation's source term, LOADS and UNIFAES, present small errors in all functions, being almost coincident with the exact solution in all function types for 20x20 spacing grid.

In functions A and C they are much better than the two five-node schemes. In function C UNIFAES is clearly the best. In function A UNIFAES is closer to the exact solution in some nodes and LOADS is closer in others; the root mean square error of present scheme is 2.0% and that of LOADS is 2.2%.

UNIFAES behaves very closely to the exponential in functions B and D. In those cases LOADS presents some wiggles, even though much less significant than central differencing's. In his investigation of LOADS, Prakash (1984) has also found a wiggly behaviour.

Summing up the results for this low λ / Pe ratio, the present scheme is very accurate in all cases, either overcoming all other schemes or, at least, approaching the best performances, such as that of the exponential in functions B and D. Considering that practical solutions will be a summation of the various solution types, this restrict excellency of the exponential is lost due to A and C components of the solution, while the present scheme benefits from its very good accuracy in all components. To a lesser extent the same happens with LOADS.

Figures 10 and 11, relative to functions A and B respectively, show the errors of the four schemes for different mesh refinements. Here the error is presented by the root mean square of the internal nodes' errors, expressed as percentage of the difference between the maximum and minimum values of the function, including boundary nodes.

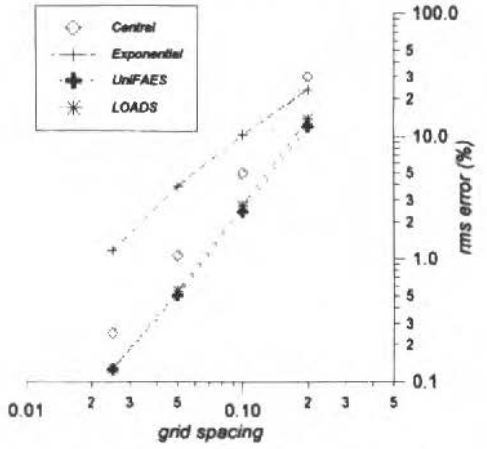

Fig. 10 Numerical Schemes' Root Mean Square Error Dependence on Grid Refinement for Function A, *Pe*=100, λ=10, θ=22.5 Degrees

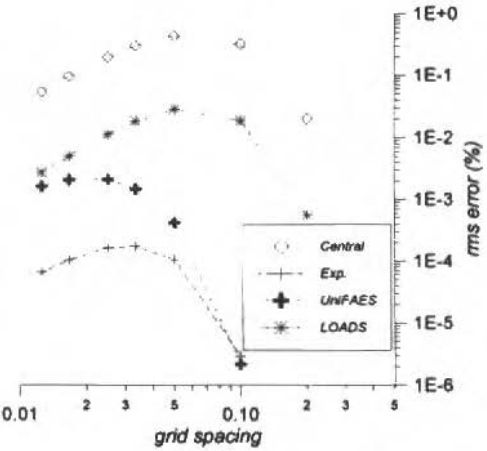

Fig. 11 Numerical Schemes' Root Mean Square Error Dependence on Grid Refinement for Function B, *Pe*=100, λ=10, θ=22.5 Degrees

In function A both central differencing, LOADS and UNIFAES show effectively quadratic reduction of the error with refinement, while the exponential shows lower rates of spatial convergence, tending asymptotically to the quadratic behaviour with the refinement. The superiority of UNIFAES is maintained with refinement.

For functions B the asymptotic tendencies can be noticed only at very refined grids. The central differencing and LOADS behave more closely to the quadratic, while the exponential and the present scheme have their behaviour dominated by higher order errors, so that the actual error is much smaller than the extrapolated second order error. The asymptotic errors of UNIFAES and LOADS appear to coincide or to be very close between themselves.

The behaviour of the schemes in functions C and D is entirely analogous to functions A and B respectively.

The functions A and C with low ratios λ / Pe correspond to the situation where the upwind and exponential schemes' solutions are strongly dependent on the angle between flow and grid. Figure 12

shows the root mean square error of the four schemes as a function of the angle for function A, keeping the remaining parameters unchanged. Although all schemes are favoured at low angles, UNIFAES shows the smallest dependence on the angle, as well as the smallest errors, being closely followed by LOADS.

The performance of the three exponential-type schemes at the very high $Pe = 10^{\gamma}$ is shown in Fig. (13) for function A with 10x10 spacings grid. The figures clearly show the superior performance of the present scheme and LOADS, whose profiles would be very close to the exact solution with the moderately refined 20x20 spacings grid.

Figure (14), showing the curves of the errors against refinement, indicates that UNIFAES and LOADS present closely quadratic reduction of the error even at such high Peclet number, the rate of error decay of UNIFAES being slightly superior than that of LOADS.

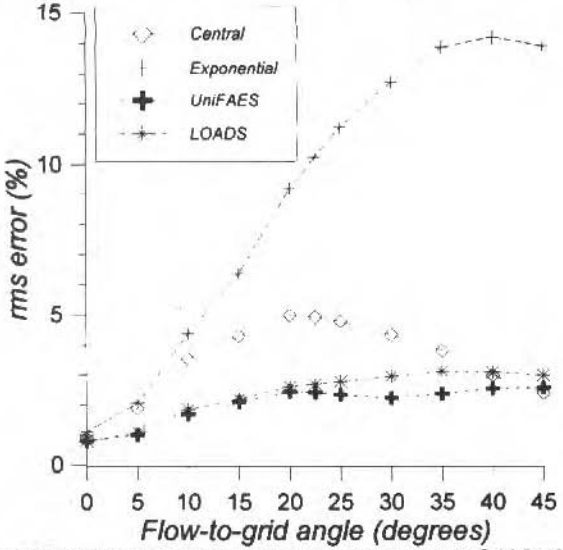

Fig. 12 Numerical Schemes' Root Mean Square Error Dependence on Flow-to-Grid Angle for Function A, *Pe*=100, λ =10

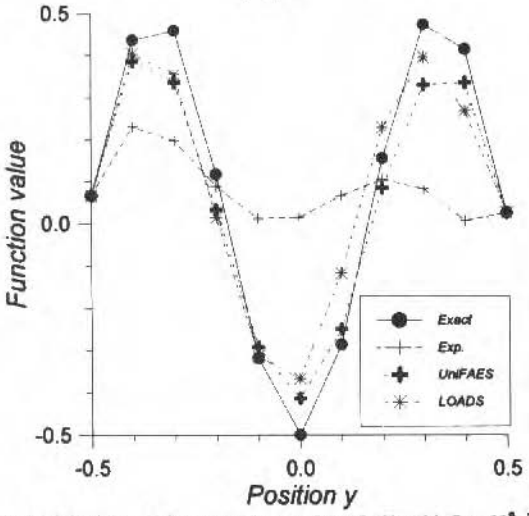

Fig. 13 Exact and Numerical Profiles for Function A at x=0.4, 10x10 grid, *Pe*= 10^5, λ =10, θ =22.5 Degrees

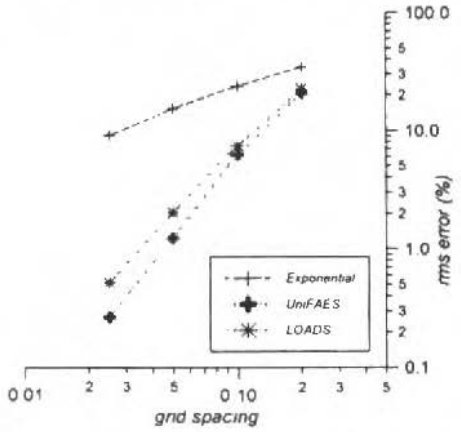

Fig. 14 Numerical Schemes' Root Mean Square Error Dependence on Grid Refinement for Function A, $Pe=10^8$, $\lambda=10$, $\theta=22.5$ Degrees

High ratios λ / Pe

The investigation of the behaviour of the schemes for growing eigenvalues presents the difficulty given by the inadequacy of the numerical mesh to resolve high frequencies. Two approaches are followed in order to investigate higher eigenvalues avoiding such difficulty.

First, by lowering the value of the Peclet number, say to $Pe=10$, one can compare the behaviour of the different schemes within a wider range of the ratio λ / Pe keeping acceptable solution frequencies. For such low Peclet number the errors are generally small, but the relative position of the schemes can be appreciated numerically in Table 1, presenting the root mean square error as percentage of the difference between the function's maximum and minimum.

Table 1 Schemes' Errors at Various Eigenvalues Pe=10; 10x10 spacings grid

λ	Central	Exponential	UNIFAES	LOADS
		Function Type A		
0.1	0.000,1	0.000,2	0.000,05	0.000,05
1.0	0.012	0.023	0.006	0.006
2.5	0.114	0.199	0.061	0.062
5.0	0.434	0.610	0.257	0.261
7.5	0.661	0.796	0.414	0.415
10.0	0.679	0.756	0.490	0.469
12.5	0.969	1.082	0.866	0.773
15.0	1.070	1.147	0.973	0.841
		Function Type B		
0.0	0.086	0.0	0.022	0.030
1.0	0.086	0.001	0.023	0.032
2.5	0.086	0.008	0.030	0.040
5.0	0.104	0.026	0.046	0.060
7.5	0.143	0.045	0.062	0.081
10.0	0.185	0.090	0.132	0.182
12.5	0.107	0.202	0.259	0.371
15.0	0.160	0.219	0.254	0.363

Table 1 (cont.)

		Function Type C		
0.1	0.000,1	0 000,5	0.000,05	0.000,05
1.0	0.012	0.031	0.005	0.005
2.5	0.068	0.016	0.016	0.017
5.0	0.053	0.050	0.049	0.051
		Function Type D		
0.0	0.086	0.0	0.022	0.030
1.0	0.198	0.000,09	0.005	0.007
2.5	0.141	0.007	0.030	0.040
5.0	0.053	0.050	0.049	0.051
		Function Type CD		
5.0	0.053	0.050	0.049	0.051
7.5	0.123	0.158	0.167	0.184
10.0	0.286	0.308	0.278	0.321
12.5	0.504	0.491	0.510	0.547
15.0	0.679	0.642	0.695	0.723
		Function Type DC		
5.0	0.053	0.050	0.049	0.051
7.5	0.114	0.168	0.148	0.169
10.0	0.268	0.276	0.279	0.309
12.5	0.529	0.528	0.481	0.556
15.0	0.575	0.574	0.503	0.585

The case λ =1 with Pe=10 corresponds to the same ratio λ / Pe as the four first examples above and the relative position of the schemes is analogous. The same occurs with other low ratios λ / Pe.

With few exceptions, there is a general increase in the errors of all schemes as the ratio λ / Pe increases, maintaining their relative positions but decreasing the relative distance between them, so the four schemes present roughly the same performance when this ratio is about or above unity. UNIFAES presents the smallest the errors within a wide range of functions and ratios λ / Pe.

The behaviour of the schemes at high eigenvalues with high Peclet numbers can be investigated by employing a summation of functions type A on the form:

$$\phi = \sum_{m=0}^{M} exp\left(\frac{Pe - \sqrt{Pe^2 + 4\lambda_m{}^2}}{2} . s \right) sin(\lambda_m . n) / (2.m - 1) \qquad (18.1)$$

where

$$\lambda_m = (2m - 1)\lambda_0 \qquad (18.2)$$

that produces the purely convective transport of a stepwise profile as both the Peclet number and the number of terms in the series, M, tend to infinite.

Such inviscid configuration has been used as a basis for describing the flow-to-grid influence upon the upwind scheme since Wolfshtein's (1968) numerical experiments (see also Patankar, 1980). The flow-to-grid problem has already been discussed for a continuous function case, where the present scheme has shown excellent performance. The convection of a stepwise profile is a severe test function for convection-diffusion schemes: first due to the high Peclet number, second because the function's discontinuity voids any conclusion based on Taylor series analysis, third because the square wave is a slowly converging function, where high frequency terms have strong influence.

Figure (15) shows the results of UNIFAES, UNIFAES-Upwind, LOADS and the simple exponential scheme for the case $Pe = 10^9$, $\lambda_0 = \pi\sqrt{2}/2 \cong 2.22$ and M = 500 with 40x40 spacings grid.

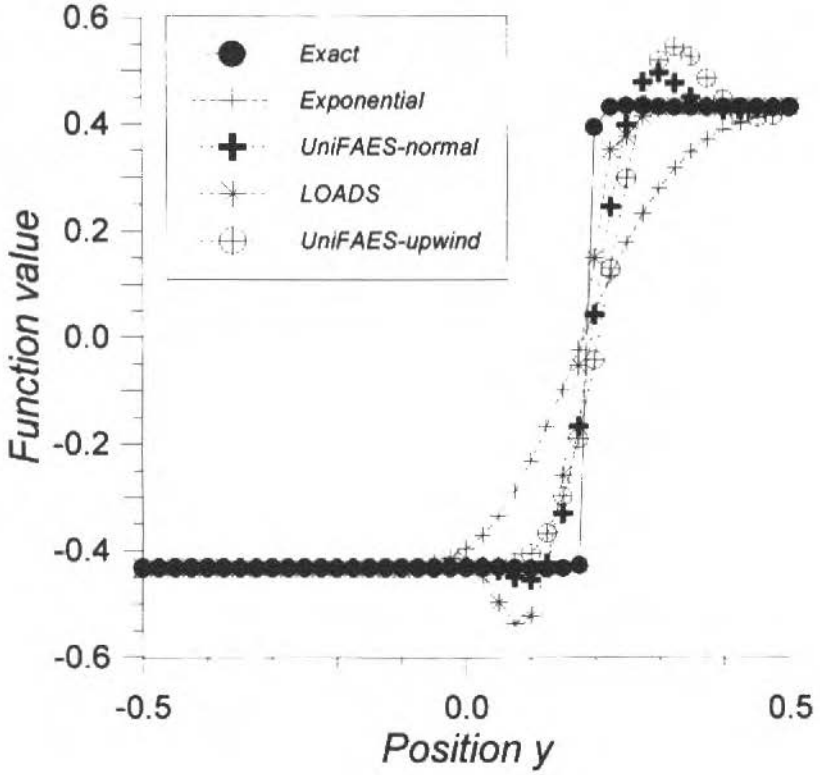

Fig. 15 Exact and Numerical Profiles for Summation of Functions A for x=0.475, 40x40 Grid, Pe= 10^9 , θ =22.5 Degrees

The exponential scheme always shows diffusive behavior. All other schemes' solutions are closer to the exact solution, but present some overshoots or undershoots. LOADS shows undershoots in the lower level region, UNIFAES-Upwind in the upper level, and UNIFAES presents both overshoots and undershoots, however its errors are smaller in the minimax sense.

In fig. (16) the same problem is taken under the point of view of the rate of decrease of the rms error with refinement, showing that both UNIFAES and LOADS have superior rate of spatial convergence to the exponential and that UNIFAES-Upwind appears to present the same rate than the exponential.

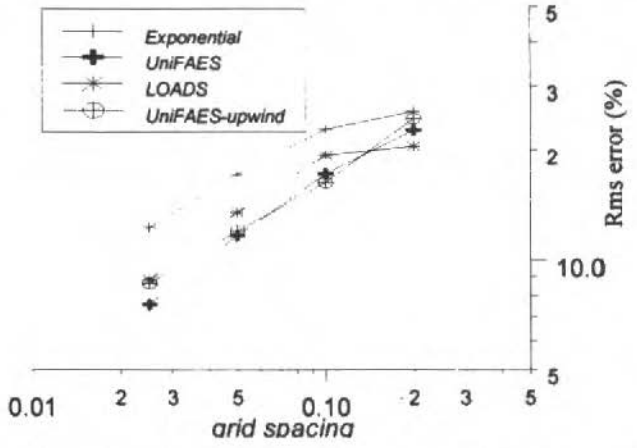

Fig. 16 Numerical Schemes' Root Mean Square Error Dependence on Grid Refinement for Summation of Functions A, $Pe = 10^9$, θ =22.5 Degrees

Stability and Convergence

As already said, the computations above employed the transient Alternating Direction Implicit method for five node schemes. The terms K for UNIFAES and LOADS were computed explicitly and included in the deferred correction term Ψ. Therefore, the computations are effectively implicit for the five-node schemes, but partially explicit with respect to these other schemes.

For the square grid case the relevant parameter for the stability of transient-like iterative processes is $\rho_k = \Delta t/\Delta x^2$. Most computations above were performed with $\rho_k = 10 / Pe$, except for Pe bellow 10, were a unitary value sufficed.

Table 2 presents the number of iterations required for A and B problems with Pe=1000, λ =10, θ =22.5 degrees, 10x10 spacings grid, for several values of ρ_k. Each iteration is actually constituted of two ADI cycles: one sweep from West to East boundaries, one from South to North, one from East to West, and one from North to South.

Table 2 Number of Iterations for Various Time-Steps Pe=1000; λ=10, 10x10 grid spacings

	Function A					
	ρ_k					
Scheme	0.002	0.005	0.01	0.02	0.05	0.1
Central	678	288	178	138	175	288
Exponencial	50	21	9	10	14	27
UNIFAES	50	27	30	151	no cvg.	no cvg.
LOADS	64	29	17	14	195	no cvg.
	Function B					
Scheme	0.002	0.005	0.01	0.02	0.05	0.1
Central	562	247	146	111	140	235
Exponencial	1	1	1	1	1	1
UNIFAES	1	1	1	1	1	1
LOADS	28	13	8	7	124	no cvg.

When precise transient information is required, so that ρ_k must be small, the number of iterations is necessarily high for all schemes (although in this case LOADS should be changed). When the transient is employed solely to reach the steady-state, the number of iterations is minimized for ρ_k roughly about 0.01. In the present case the number of iterations is proportional to the computational time spending, since the calculation of the coefficients is done only once for each scheme. For optimal values of ρ_k the number of iterations of both UNIFAES and LOADS are close to that of the exponential and much lower than that of central differencing. LOADS needs generally less iterations than UNIFAES in function A, whilst UNIFAES is much quicker than LOADS in function B.

The convergence of the algorithm with the two five-node schemes occurred for all values of ρ_k in the table, but with UNIFAES and LOADS convergence was not so unconditional. UNIFAES has more restrict range of stability in function A and LOADS more restrict range in function B. Improved stability could be expected for both schemes by employing effectively implicit methods. However, for the present purposes the simplified approach was capable of offering quick results within its restrict, but wide, stability range.

Conclusions

The methodology of Allen for constructing exponential type differencing schemes for convective-diffusive transport equation was generalized for irregularly spaced grids, and then introduced within the control volume methodology as a means to compute the source term of the generating equation, constructing a new scheme of the family of exponential schemes that includes LOADS and Flux-Spline.

Although restricted to the constant velocity case, the methodology of testing employed, sweeping the spectrum of solutions, was able to reproduce many of the situations found in applied problems, such as the effects of flow-to-grid angle, Peclet number variations and the distinct levels of smoothness or steepness of solutions.

The schemes that employ the source term of the generating equation, LOADS and UNIFAES, presented in general superior accuracy to the classic schemes central and simple exponential. UNIFAES has shown the best performance almost always, while LOADS presents undesirable wiggles in some cases. On the other side UNIFAES is simpler and more general than LOADS, since its computation of the generating equation's source terms only employs terms emerging from the direction under consideration, demanding no information from source, transient and cross-fluxes terms.

The present scheme was given a name inspired in the fact that it unified two so far distinct numerical approaches with regard to the exponential interpolating curve. Through the test cases it has also been shown to unify accuracy and stability with relative simplicity and great generality. Those results are clearly encouraging of further testing and application of the present scheme.

Acknowledgements

The author gratefully acknowledges the financial support of the Brazilian National Council for Scientific and Technological Development, CNPq, for this research, under grant number 350776/94.8

References

Allen, D.N.de G., and Soutwell, R.V., 1955, "Relaxation Methods Applied to Determine the Motion, in Two Dimensions, of a Viscous Flow Past a Fixed Cylinder"; Quart. J. Mech. and Applied Math.,Vol.8, pp. 129-145.

Karki, K. C., Patankar, S. V., and Mongia, M. C., 1989, "Solution of Three-Dimensional Flow Problem Using a Flux-Spline Method", AIAA-89-0687.

Nieckele, A. O., 1985, "Development and Evaluation of Numerical Schemes for the Solution of Convection-Diffusive Problems", Ph.D. Thesis, University of Minnesota, Minneapolis.

Oliveira, P. C., 1997, "Esquema FLUX-SPLINE Aplicado em Cavidades Abertas com Convecção Natural", Doctoral Thesis, Universidade Estadual de Campinas, Campinas, SP.

Patankar, S. V., 1980, "Numerical Heat Transfer and Fluid Flow", Mc-Graw-Hill, New York.

Prakash, C., 1984, "Application of the Locally Analytic Differencing Scheme to Some Test Problems for the Convection-Diffusion Equation", Numer. Heat Transfer, Vol.7, pp.165-182.

Raithby, G.D., and Torrance, K. E., 1974, "Upstream-Weighted Differencing Scheme and Their Application to Elliptic Problems Involving Fluid Flow", Computers and Fluids, Vol. 2, pp.191-206.

Spalding, D.B., 1972, "A Novel Finite Difference Formulation for Differential Expressions Involving Both First and Second Derivatives", Int. J. Numer. Meth. Eng., Vol. 4, pp.551-559.

Ulson de Souza, A.A., 1992, "Um Esquema para Minimização da Difusão Numérica na Solução de Escoamentos em Geometrias Arbitrárias", Doctoral Thesis, Universidade Federal de Santa Catarina, Florianópolis, S.C.

Varejão, L.M.C., 1979, "Flux-Spline Method for Heat and Momentum Transfer", Ph.D. Thesis, University of Minnesota, Minneapolis.

Wolfshtein, M., 1968, "Numerical Smearing in One-Sided Difference Approximations to the Equations of Non-Viscous Flow", Report EF/TN/A/3, Imperial College, Mech. Eng. Dept., London.

Wong, H.H., and Raithby, G.D., 1979, "Improved Finite-Difference Methods Based on a Critical Evaluation of the Approximation Errors", Numer. Heat Transfer, Vol. 2, pp.139-163.

RBCM - J. of the Braz. Soc. Mechanical Sciences
Vol. XIX - No 3 - 1997 - pp. 392-409

ISSN 0100-7386
Printed in Brazil

An Optimization of the Finite Difference Method for Modeling Solidification of Complex Shaped Domains

Jaime Alvares Spim Junior
Amauri Garcia
UNICAMP - Universidade Estadual de Campinas
Faculdade de Engenharia Mecânica
Departamento de Engenharia de Materiais
13083-970 Campinas. S.P. Brasil
spim@fem.unicamp.br

Abstract

The finite-difference method is widely used in the formulation of a mathematical representation of the solidification process in metal/mold systems. When complex geometries have to be analyzed, generally Finite-Elements Methods are preferred. The present work proposes a modification in the distribution of elements from the mesh, by using an analogy between electrical and thermal circuits, which permits greater versatility in discretizing regions of complex shape. The governing equation of electrical circuits theory is used by applying an explicit version of the Finite-Difference Method.

Keywords: *Mathematical Modeling, Solidification, Simulation, Two-phase Systems.*

Introduction

The numerical techniques applied to the solution of differential equations governing a number of engineering problems, emerge as powerful tools for the simulation of manufacturing processes. The progressive advance of computer facilities has permitted the development of models of high precision and efficiency, which can be applied in different areas of the human knowledge. Particularly in the modern foundry industry, the simulation of the solidification process has become an increasing practice in last years in the search for better quality products. Porosities formation, the number and size of inclusions, species distribution, surface cracks, etc., as well as cooling rates along the foundry system can be predicted and modeled by using an appropriate numerical approach.

The numerical tools based on the finite difference technique have proved to be flexible and efficient when analyzing heat transfer phenomena, and are widely applied on:

- One-dimensional and multidimensional systems;
- Systems where physical properties varying with space and/or time must be considered;
- Systems with variable boundary conditions;
- Systems where the physical body has to be represented by a mesh variable in form and size in order to permit a better description of geometric features.

Nomenclature

C_t - Capacitance [J/K],
c - Specific Heat [J/kg.K];
f_s - Solid Fraction [%].
H - Latent Heat of Fusion [J/kg];
hox e hoy - Heat Transfer Coefficients in directions X and Y [W/m K].
i, j - Mesh Indices;
k - Thermal Conductivity [W/m.K],
Lx e Ly - Length[m],
Nx e Ny - Number of Elements in directions X and Y;
n - Time Index;
R_t - Thermal Resistance [K/W],
T - Temperature [K];
Tox e Toy - Cooling Temperatures [K];
t - Time [s],
'x', 'y' e 'z'- Space Coordinates [m];
ρ - Density [kg/m³];

A number of authors (Spim and Garcia, 1992; 1993; 1996) have developed numerical models based on the Finite Difference Method (FDM), including applications on the continuous casting of steel,

Manuscript received: December 1994. Technical Editor: Leonardo Goldstein Jr

metal-mold systems of complex shapes and in general analysis of foundry systems. These models have proved to provide a realistic description of these processes, and can be considered extremely versatile in terms of the development of computer programs for simulation and control of industrial processes. However, the application of FDM to complex shaped geometries as shown in Fig. 1, can be a difficult task. Spatial domains with a very fine grid, like some used on the solution of problems of solidification of metallic alloys, rapid transient boundary conditions and phase change (Voller, 1991; Ramakrishna, 1984), require a significant increase on computer memory storage. The computation time can be impractical when using traditional solution techniques since it is proportional to the number of nodes squared.

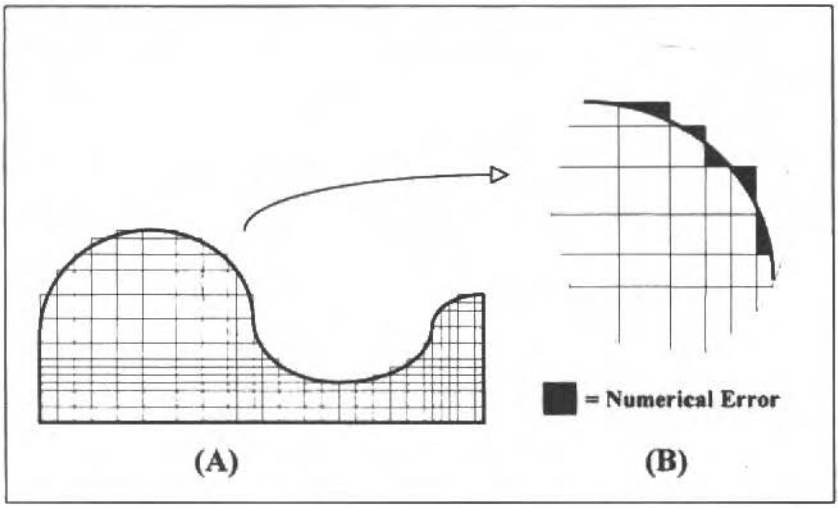

Fig. 1 (A) Finite Difference Network on Spatial Domain; (B) Numerical Errors on Boundaries.

Patankar (1980) suggests mesh manipulations when using the finite difference representation of the heat conduction equation in cartesian, cylindrical or spherical coordinates. However, he is not clear about the treatment to be given for complex boundaries where it is usually impractical to choose a uniform square mesh. In these cases a very refined grid is necessary for providing accurate simulation. Philips e Schimidt (1984) have proposed a multigrid computational scheme, which permits the use of local mesh refinement. A coarse grid is used for the main part of the physical body and at the irregular boundaries a sufficiently fine grid to yield accurate results is adopted. The success of the proposed approach depends on the transmittal of information at the interface boundaries between grid patterns. The authors have observed a significant saving on computational time and computer memory storage. The approach generates simultaneous results in real time, in both coarse and fine grids, and an iterative process to connect solutions of each grid mesh is not necessary.

Heat Transfer During Solidification

The solid/liquid phase change heat transfer problem can be analyzed by the heat conduction equation (Incropera, 1981), given by:

$$\rho\left(c - H\frac{\partial fs}{\partial T}\right)\frac{\partial T}{\partial t} = \frac{\partial}{\partial x}\left(k(x)\frac{\partial T}{\partial x}\right) + \frac{\partial}{\partial y}\left(k(y)\frac{\partial T}{\partial y}\right) + \frac{\partial}{\partial z}\left(k(z)\frac{\partial T}{\partial z}\right) \qquad (1)$$

where ρ, c, k and H are respectively density, specific heat, thermal conductivity and latent heat of fusion. The term 'fs' is the solidified fraction, 'T' is the temperature, 't' is time and 'x', 'y' and 'z' the space coordinates.

During solidification of binary alloys the phase transformation takes place in a situation where solid and liquid phases can coexist in equilibrium at various temperatures and separated by a intermediate phase between the liquidus temperature (T_L) and the solidus temperature (T_S). This intermediate region is called mushy zone.

Usually, the metallic alloys used in engineering applications can be considered as isotropic materials in terms of conduction, where:

$$k(x) = k(y) = k(z) = k \tag{2}$$

The term $\left(H.\frac{\partial f_s}{\partial T}\right)$ on the right hand side of Eq. (1) can be considered as a pseudo specific heat. The apparent specific heat represented by $c' = \left(c - H.\frac{\partial f_s}{\partial T}\right)$ includes the effect of latent heat evolved internally during liquid/solid transformation.

The physical properties when the material is totally liquid or completely solid will be considered as constants, and:

$\rho = \rho_L$; $k = k_L$ *and* $c = c_L$ ⇨ Liquid phase ⇨ *100% Liquid*

$\rho = \rho_S$; $k = k_S$ *and* $c = c_S$ ⇨ Solid phase ⇨ *100% Solid*

At the range of temperatures where solidification occurs for metallic alloys ($T_{Liquidus} \leq T \leq T_{Solidus}$), the physical properties will be evaluated taking into account the amount of liquid and solid which coexist in equilibrium at each temperature (Voller, 1991):

$$\rho_P = (\rho_S - \rho_L) f_s + \rho_L \tag{3}$$

$$k_P = (k_S - k_L) f_s + k_L \tag{4}$$

$$c_P = (c_S - c_L) f_s + c_L - H \frac{\partial f_s}{\partial T} \tag{5}$$

Considering the assumptions described above, Eq. (1) in a two-dimensional form can be written as:

$$\rho c' \frac{\partial T}{\partial t} = k\left(\frac{\partial^2 T}{\partial x^2} + \frac{\partial^2 T}{\partial y^2}\right) \tag{6}$$

The solid fraction, depends on a number of parameters involved in the foundry system. However is quite reasonable to assume f_s varying only with temperature:

$$fs = F(T) \text{ where } T_S < T < T_L \tag{7}$$

The correct formulation of F(T) is dependent on chemical species present in the alloy composition and on the way they interact with solidification parameters. The $f_s(T)$ can be obtained from: 1- Lever Rule; 2- Scheil's Equation; 3- Brody-Flemings Model; 4- Clyne-Kurz Model; 5- Ohnaka's Model (Spim, 1996).

Finite Difference Representation of the Heat Conduction Equation

By introducing finite difference terms into Eq. (6), yields:

$$\rho\, c\cdot \frac{T_{i,j}^{n+1} - T_{i,j}^{n}}{\Delta t} = k\left(\frac{T_{i+1,j}^{n+1} - 2\,T_{i,j}^{n-1} + T_{i-1,j}^{n+1}}{\Delta x^2} + \frac{T_{i,j+1}^{n+1} - 2\,T_{i,j}^{n-1} + T_{i,j-1}^{n+1}}{\Delta y^2}\right) \tag{8}$$

where:

$$T_{i,j}^{n+1} = T(t_i + \Delta t, x_i, y_i) \tag{9}$$

$$T_{i,j}^{n} = T(t_i, x_i, y_i) \tag{10}$$

$$T_{i+1,j}^{n+1} = T(t_i + \Delta t, x_i + \Delta x, y_i) \qquad T_{i,j+1}^{n+1} = T(t_i + \Delta t, x_i, y_i + \Delta y) \tag{11}$$

$$T_{i-1,j}^{n+1} = T(t_i + \Delta t, x_i - \Delta x, y_i) \qquad T_{i,j-1}^{n+1} = T(t_i + \Delta t, x_i, y_i - \Delta y) \tag{12}$$

and t_i, x_i and y_i are instantaneous time and space representations.

Multiplying Eq. (8) by '$\Delta x.\Delta y.\Delta z$' and considering in each case $At_y = \Delta x.\Delta z$ and $At_x = \Delta y.\Delta z$:

$$\begin{aligned}\Delta x\ \Delta y\ \Delta z\ \rho\, c\cdot \frac{T_{i,j}^{n+1} - T_{i,j}^{n}}{\Delta t} = {} & At_x\ k\,\frac{(T_{i+1,j}^{n+1} - T_{i,j}^{n-1})}{\Delta x} + At_x\ k\,\frac{(T_{i-1,j}^{n+1} - T_{i,j}^{n+1})}{\Delta x} \\ & + At_y\ k\,\frac{(T_{i,j+1}^{n+1} - T_{i,j}^{n+1})}{\Delta y} + At_y\ k\,\frac{(T_{i,j-1}^{n-1} - T_{i,j}^{n-1})}{\Delta y}\end{aligned} \tag{13}$$

Equation (13) represents heat flux variations with time.

Analogy Between Electrical and Thermal Circuits and the FDM Numerical Technique Applied to Heat Flow Phenomena

There is a large body of literature dealing with the analogy between a thermal system and the passive elements of an electrical circuit (resistors and capacitors), according to Eqs. (14), (15) and (16) and Figs. 2 e 3 (Holman, 1983):

$$Ct_{i,j} = \rho_{i,j} . c_{i,j} . Vol_{i,j} \tag{14}$$

where: $Vol_{i,j} = \Delta x_i . \Delta y_j . \Delta z$

In Figure 2:

$T^n_{i,j}$ = Temperature of 'i,j' at time 't';

q_E= Heat flux entering the element;

q_S = Heat flux out of the element;

q_q = Charge flow of $Ct_{i,j}$;

q_D = Uncharge flow of $Ct_{i,j}$;

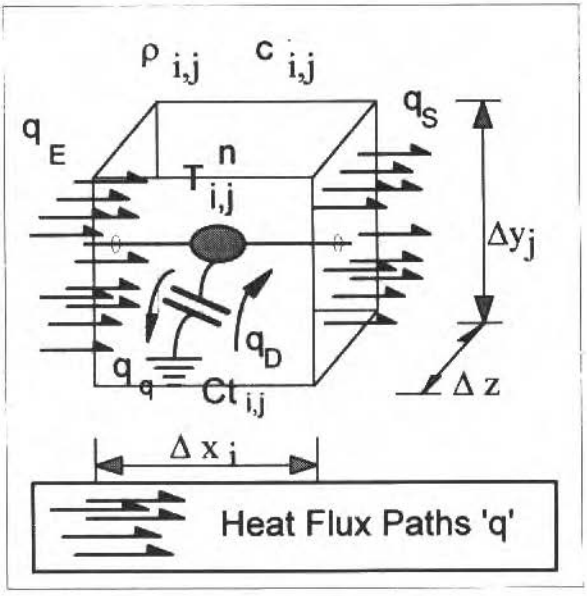

Fig. 2 Physical Representation of Thermal Capacitor

$$Rt_{i,j} = \frac{Dist}{2 . k_{i,j} . At_x} \tag{15}$$

$$Rt_{o,j} = \frac{1}{h_o . At_x} \tag{16}$$

In Figure 3:

$T^n_{i,j}$ = Temperature of 'i,j' at time 't';

T_{Amb} = Environment temperature;

$k_{i,j}$ = Thermal conductivity of point 'i,j';

h_o = Convection heat transfer coefficient;

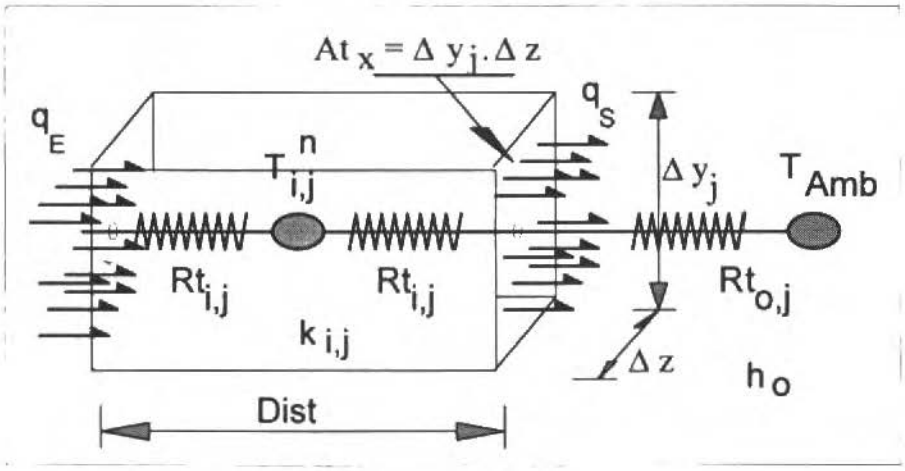

Fig. 3 Physical Representation of Thermal Resistances

It can be seen on Eq. (13), that each term on the right hand side is related to an equation similar to that which defines the thermal resistance $Rt_{i,j}$ Eq. (15), in the following manner:

$$At_x \; k \frac{(T^{n+1}_{i+1,j} - T^{n+1}_{i,j})}{\Delta x} = \frac{\left(T^{n+1}_{i+1,j} - T^{n+1}_{i,j}\right)}{Rt_{i,j \leftarrow i+1,j}} \tag{17}$$

where the term $Rt_{i,j \leftarrow i+1,j}$ represents the thermal resistance at the heat flux line from point "i+1,j" to the point "i,j". It can be observed on Fig. 4, that this term is given by the sum of thermal resistances inside the element "i,j" - (from center to the At_x interface) and thermal resistances inside element "i+1,j" - (from At_x interface to the center), according to the following equation:

$$Rt_{i,j \leftarrow i+1,j} = Rt_{i,j} + Rt_{i+1,j} = \frac{\Delta x_{i,j}}{2\, k_{i,j}\, At_x} + \frac{\Delta x_{i+1,j}}{2\, k_{i+1,j}\, At_x} \tag{18}$$

The right hand side terms of Eq. (18) can be rearranged in the form:

$$Rt_{i,j \leftarrow i+1,j} = \frac{1}{2\, At_x}\left(\frac{\Delta x_i}{k_{i,j}} + \frac{\Delta x_{i+1}}{k_{i+1,j}}\right) = \frac{1}{2\, At_x}\,\frac{k_{i+1,j}\,\Delta x_i + k_{i,j}\,\Delta x_{i+1}}{k_{i+1,j}\,k_{i,j}} \tag{19}$$

The mean thermal resistance between points 'i+1,j' ('$k_{i+1,j}$') and 'i,j' ('$k_{i,j}$'), 'k_m', can be defined as:

$$k_m = \frac{k_{i+1,j}\,\Delta x_i + k_{i,j}\,\Delta x_{i+1}}{k_{i+1,j}\,k_{i,j}} \tag{20}$$

Equation (20) is well known and applied for multiphase materials (Kingery, 1976), and is recommended to be used for cases of variable thermal conductivity (Patankar, 1980).

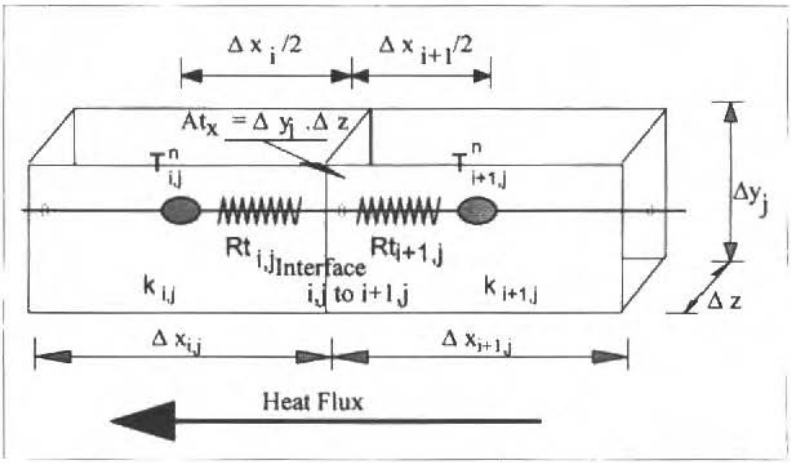

Fig. 4 Physical Representation of Thermal Resistances for Heat Flow Through Neighboring Elements

A similar procedure makes possible to find each term on Eq. (13), resulting:

$$\frac{Ct_{i,j}}{\Delta t}.(T_{i,j}^{n+1} - T_{i,j}^{n}) = \frac{T_{i+1,j}^{n+1}}{Rt_{i,j} + Rt_{i+1,j}} + \frac{T_{i-1,j}^{n+1}}{Rt_{i,j} + Rt_{i-1,j}} + \frac{T_{i,j+1}^{n+1}}{Rt_{i,j} + Rt_{i,j+1}} + \frac{T_{i,j-1}^{n+1}}{Rt_{i,j} + Rt_{i,j-1}} - \ldots$$
$$\ldots - T_{i,j}^{n+1}.\left(\frac{1}{Rt_{i,j} + Rt_{i+1,j}} + \frac{1}{Rt_{i,j} + Rt_{i-1,j}} + \frac{1}{Rt_{i,j} + Rt_{i,j+1}} + \frac{1}{Rt_{i,j} + Rt_{i,j-1}}\right) \quad (21)$$

By rearranging Eq. (21), we obtain:

$$T_{i,j}^{n} = -\frac{\Delta t}{\tau_{i+1,j}}.T_{i+1,j}^{n+1} - \frac{\Delta t}{\tau_{i-1,j}}.T_{i-1,j}^{n+1} - \frac{\Delta t}{\tau_{i,j+1}}.T_{i,j+1}^{n+1} - \frac{\Delta t}{\tau_{i,j-1}}.T_{i,j-1}^{n+1} + \left(1 + \frac{\Delta t}{\tau_{i,j}}\right).T_{i,j}^{n+1} \quad (22)$$

where:

$$\tau_{i+1,j} = Ct_{i,j}.\left(Rt_{i+1,j} + Rt_{i,j}\right) \quad (23)$$

$$\tau_{i-1,j} = Ct_{i,j}.\left(Rt_{i-1,j} + Rt_{i,j}\right) \quad (24)$$

$$\tau_{i,j+1} = Ct_{i,j}.\left(Rt_{i,j+1} + Rt_{i,j}\right) \quad (25)$$

$$\tau_{i,j-1} = Ct_{i,j}.\left(Rt_{i,j-1} + Rt_{i,j}\right) \quad (26)$$

$$\frac{1}{\tau_{i,j}} = \frac{1}{\tau_{i+1,j}} + \frac{1}{\tau_{i-1,j}} + \frac{1}{\tau_{i,j+1}} + \frac{1}{\tau_{i,j-1}} \tag{27}$$

Equation (22) represents the implicit form of the finite difference method. The equation representing the explicit form is obtained by a similar treatment and is given by:

$$T_{i,j}^{n+1} = \frac{\Delta t}{\tau_{i+1,j}} . T_{i+1,j}^{n} + \frac{\Delta t}{\tau_{i-1,j}} . T_{i-1,j}^{n} + \frac{\Delta t}{\tau_{i,j+1}} . T_{i,j+1}^{n} + \frac{\Delta t}{\tau_{i,j-1}} . T_{i,j-1}^{n} + \left(1 - \frac{\Delta t}{\tau_{i,j}}\right) . T_{i,j}^{n} \tag{28}$$

Equation (28) becomes unstable for $\Delta t \leq \tau_{i,j}$ (Stability Limits).

Equation (22) can be solved by introducing a linear system:

$$\Delta t . [M_T] . \{T_{i,j}\}^{n+1} = \{T_{i,j}\}^{n} \tag{29}$$

where there is no restriction on the size of the time step Δt.

Application of the Thermal / Electrical Analogy to a Net of Variable Mesh Size

The literature presents a number of papers treating the finite difference mesh with variable size (different values of Δx, Δy, Δz). Patankar (1980) has pointed out the advantages of using a non-uniform mesh to cases of one and two dimensions grids, as shown in Fig. 5.

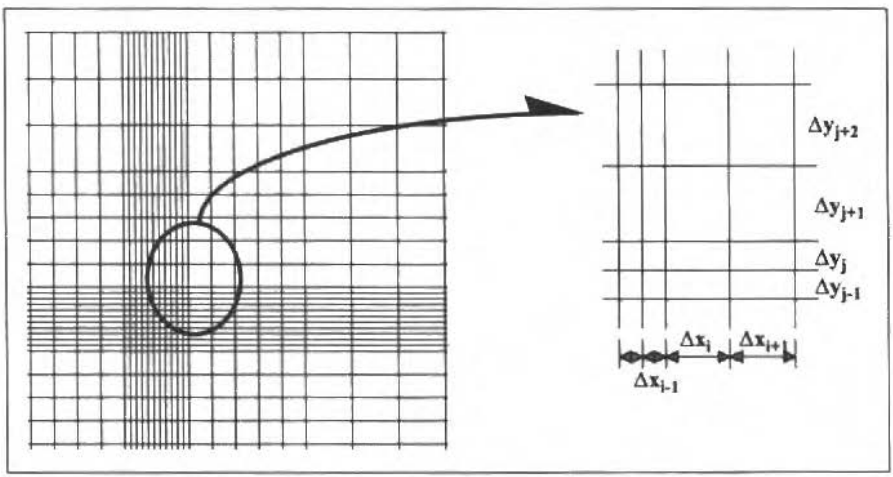

Fig. 5 Finite Difference Mesh with Elements of Different Size

However, the network shown in Fig. 5 will not be efficient when applied to irregularly shaped domains, due to numerical errors associated, as it was shown in Fig. 1. An irregular boundary may be approximated by a series of rectangular steps, as shown in Fig. 6, yielding a more efficient solution. Anyway, the mathematical treatment of this grid is not an easy task.

It can be seen that at the coarse elements / fine elements interface there is not a common heat flux path, as shown in Fig. 7:

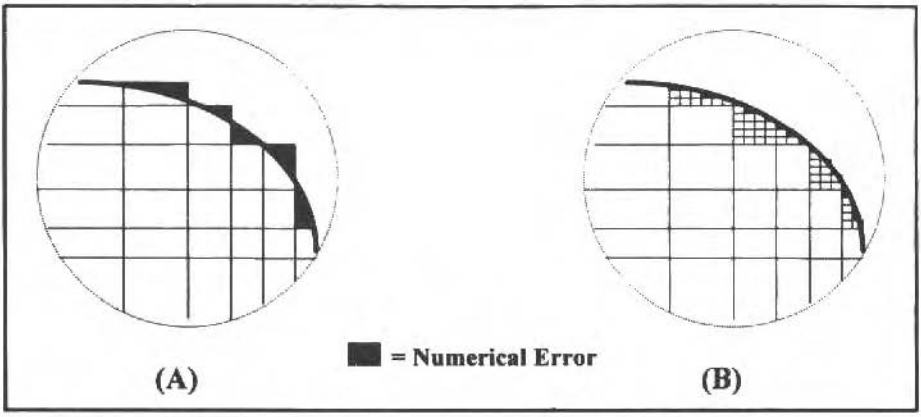

Fig. 6 (A) Conventional Grid; (B) Modified Grid

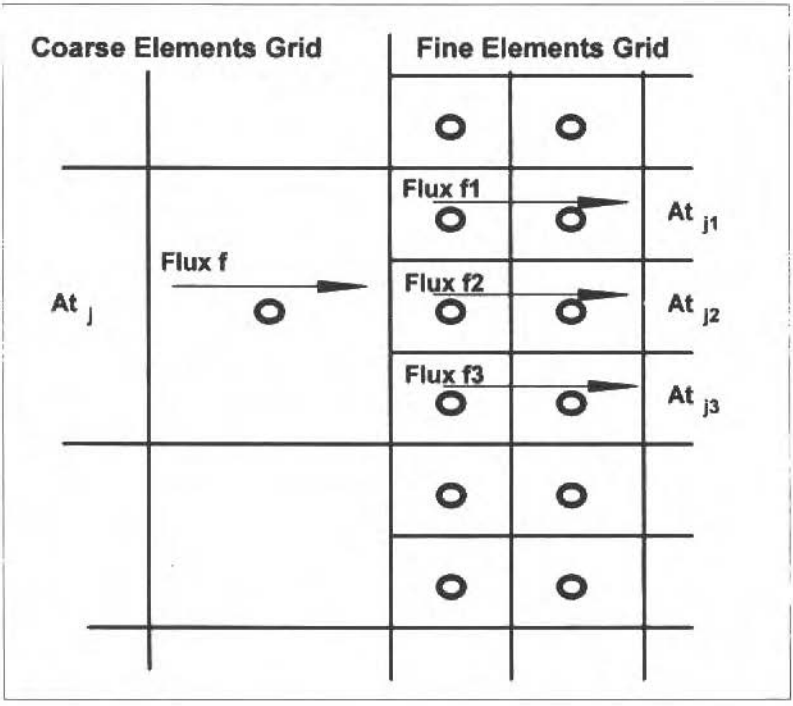

Fig. 7 Heat Flow at the Coarse Grid / Fine Grid Interface

Philips e Schimidt (1984) have proposed an approach to obtain a solution for the network proposed in Fig. 7. However, the above mentioned approach is restricted to the connection between coarse grid and fine grid.

The present work presents a solution for the problem formulated in Fig. 7, based on the analogy between thermal and electrical circuits. It is important to emphasize that when the finite difference network is modified from thermal to electrical elements, it will be subjected to the theoretical considerations which are applied to electric circuits (resistors and capacitors). This permits a flexible and versatile representation and connection among electrical elements, as can be seen in Fig. 8, where each coarse element is connected to these elements of the finer grid.

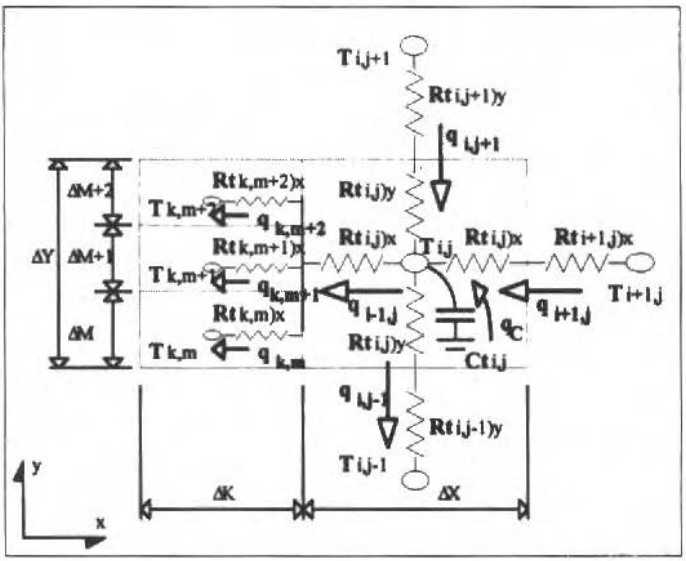

Fig. 8 Modified Network: Coupling of Coarse and Fine Elements

The mathematical approach is similar to that used in the conventional finite difference method, that is:

$$\sum \begin{bmatrix} Flux\ (q) \\ entering \\ point\ (i,j) \end{bmatrix} = \sum \begin{bmatrix} Flux\ (q) \\ leaving \\ point\ (i,j) \end{bmatrix} \tag{30}$$

However, it is not easy to determine the flux $q_{i-1,j}$, as can be seen in Fig. 8, where by using electrical relationships, we have:

$$q_{i-1,j} = q_{k,m} + q_{k,m+1} + q_{k,m+2} \tag{31}$$

We can now suppose that a nodal point of temperature T_p is connecting the resistances of the coarser grid with resistance of the finer grid, according to Fig. 9:

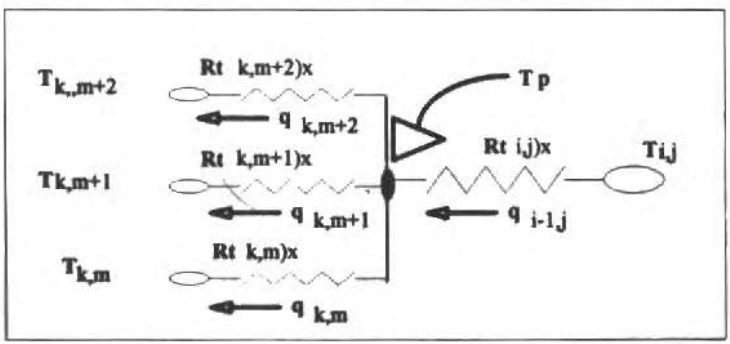

Fig. 9 Nodal Point Connecting Coarse with Fine Grid

Heat flux is given by:

$$q_{i-1,j}^{n+1} = \frac{T_{i,j}^{n+1} - T_p^{n+1}}{Rt_{i,j)x}} \tag{32}$$

$$q_{k,m}^{n+1} = \frac{T_p^{n+1} - T_{k,m}^{n+1}}{Rt_{k,m)x}} \tag{33}$$

$$q_{k,m+1}^{n+1} = \frac{T_p^{n+1} - T_{k,m+1}^{n+1}}{Rt_{k,m+1)x}} \tag{34}$$

$$q_{k,m+2}^{n+1} = \frac{T_p^{n+1} - T_{k,m+2}^{n+1}}{Rt_{k,m+2)x}} \tag{35}$$

By substitution of Eqs. (32), (33), (34) and (35) into Eq. (31), we have:

$$T_p^{n+1} = R_p \cdot \left(\frac{T_{i,j}^{n+1}}{Rt_{i,j)x}} + \frac{T_{k,m}^{n+1}}{Rt_{k,m)x}} + \frac{T_{k,m+1}^{n+1}}{Rt_{k,m+1)x}} + \frac{T_{k,m+2}^{n+1}}{Rt_{k,m+2)x}} \right) \tag{36}$$

where:

$$R_p = \left(\frac{1}{Rt_{i,j)x}} + \frac{1}{Rt_{k,m)x}} + \frac{1}{Rt_{k,m+1)x}} + \frac{1}{Rt_{k,m+2)x}} \right)^{-1} \tag{37}$$

So, by substitution of Eq. (36) into Eq. (32), the heat flux $q_{i-1,j}$ is given by:

$$q_{i-1,j}^{n+1} = \frac{T_{i,j}^{n+1}}{Rt_{i,j)x}} - \frac{R_p}{Rt_{i,j)x}} \cdot \left(\frac{T_{i,j}^{n+1}}{Rt_{i,j)x}} + \frac{T_{k,m}^{n+1}}{Rt_{k,m)x}} + \frac{T_{k,m+1}^{n+1}}{Rt_{k,m+1)x}} + \frac{T_{k,m+2}^{n+1}}{Rt_{k,m+2)x}} \right) \tag{38}$$

For one element of the coarse grid connected to N elements from the fine grid, the general equation is given by:

$$q_{i-1,j}^{n+1} = \frac{T_{i,j}^{n+1}}{Rt_{i,j)x}} - \frac{R_p^G}{Rt_{i,j)x}} \cdot \left(\frac{T_{i,j}^{n+1}}{Rt_{i,j)x}} + \sum_{m=1}^{N} \frac{T_{k,m}^{n+1}}{Rt_{k,m)x}} \right) \tag{39}$$

where:

$$R_p^G = \left(\frac{1}{Rt_{i,j)x}} + \sum_{m=1}^{N} \frac{1}{Rt_{k,m)x}} \right)^{-1} \tag{40}$$

The solution for any point of the network, representing the physical body, is given by:

$$T_{i,j}^{n} = \frac{\Delta t}{Ct_{i,j}} \cdot \left(q_{i-1,j}^{n+1} - q_{i+1,j}^{n+1} + q_{i,j-1}^{n+1} - q_{i,j+1}^{n+1} \right) + T_{i,j}^{n+1} \tag{41}$$

Validation of the Coupling Between Coarse and Fine Grids

In order to test the above approach, a comparison between prediction furnished by Eq. (41) and a exact solution would be convenient. As there is no exact solution available, comparisons will be performed by using a conventional finite difference technique with an extremely fine grid. The physical body to be considered is a rectangular ingot cooled in two surfaces and insulated at the opposite surfaces, as shown in Fig. 10.

In Figure 10:

- Lx and Ly are ingot dimensions in X and Y directions,
- Nx and Ny are number of elements form the mesh in X and Y directions,
- Tox and Toy are cooling temperatures in X and Y directions, and
- hox and hoy are heat transfer coefficients in X and Y directions.

Simulation starts with all the nodal points at a temperature above the liquidus temperature. Solidification begins at the cooled surfaces and the solidification front is progressively displaced toward the insulated regions. The beginning of solidification is characterized by the nodal points at the liquidus temperature, and the solidification front by those points at the solidus temperature.

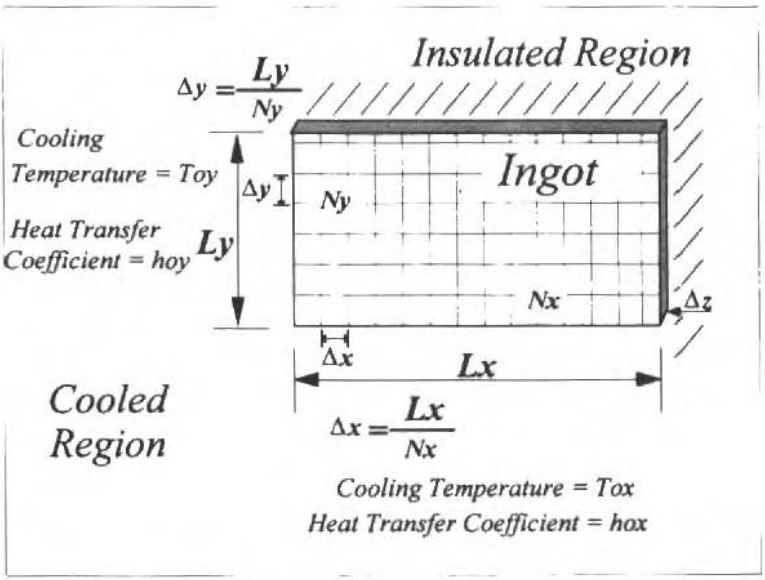

Fig. 10 Physical Body Admited for Simulation

The materials selected for simulations were a 0,62% carbon steel and a Al-4,5%Cu alloy. The thermophysical properties used in calculations are presented in Table 1. To take into account the evolution of the solid fraction in the range of solidification, the lever rule was assumed for the steel and the Scheil's equation was considered for the aluminum alloy (Spim, 1996). The numerical computer program has been structured by using the C language, and the simulations were performed on a DX4-486/100MHz computer with 16Mb of RAM memory.

The different network configurations used on simulations and comparisons are shown in Fig. 11. The number of elements on the coarse network, Nx and Ny, were taken as reference values. The grid was then refined according to cases (B), (C), (D) and (E) in Fig. 11.

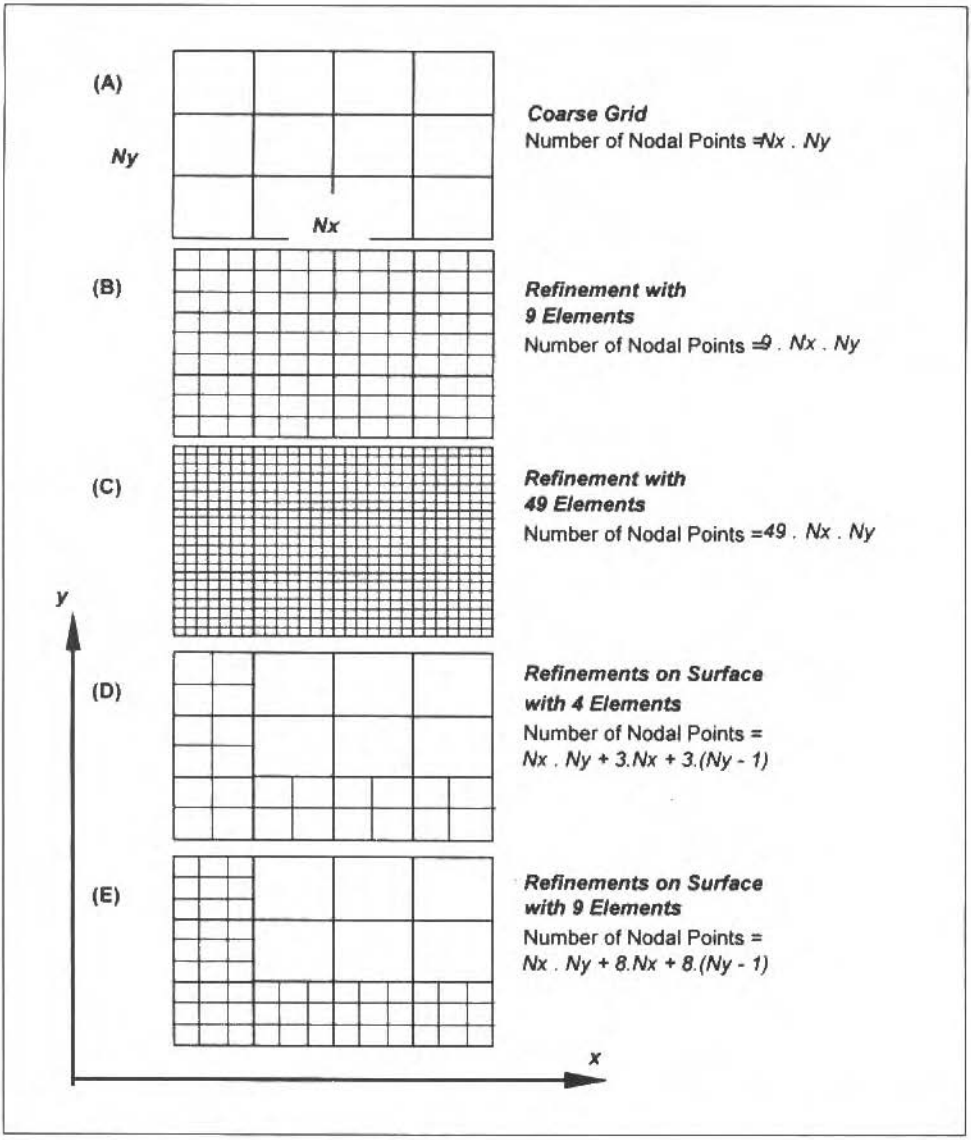

Fig. 11 (A) Coarse Grid; (B) Refinement with 9 Elements; (C) Refinements with 49 Elements; (D) Refinement on Surface - 4 Elements; (E) Refinement on Surface 9 Elements

Table 1 Physical Properties

Metal		Thermal Condutivity k [W/m.K]	Specific Heat c [J/kg.K]	Density ρ [kg/m³]	Temperature [K]	Latente Heat H [J/kg]	References
Al-4,5%Cu	Solid	100	880	2750	821	384000	Metals
	Liquid	180	920	2650	920		1989
Aço 1062	Solid	25,4	679	7000	1693	260000	Wahburn
	Liquid	29,3	670	7400	1765		1972

Results of Simulations

A first set of simulations was carried out to confirm the validity of the proposed model, by comparing predictions with those provided by a conventional finite difference technique with an extremely fine grid. Fig. 12 shows the results concerning the cooling curves of a surface point for different network refinement situations. It can be seen that a single refinement on surface with 9 elements permits the proposed model predictions to have an excellent agreement with the results furnished by the fine grid conventional finite difference method.

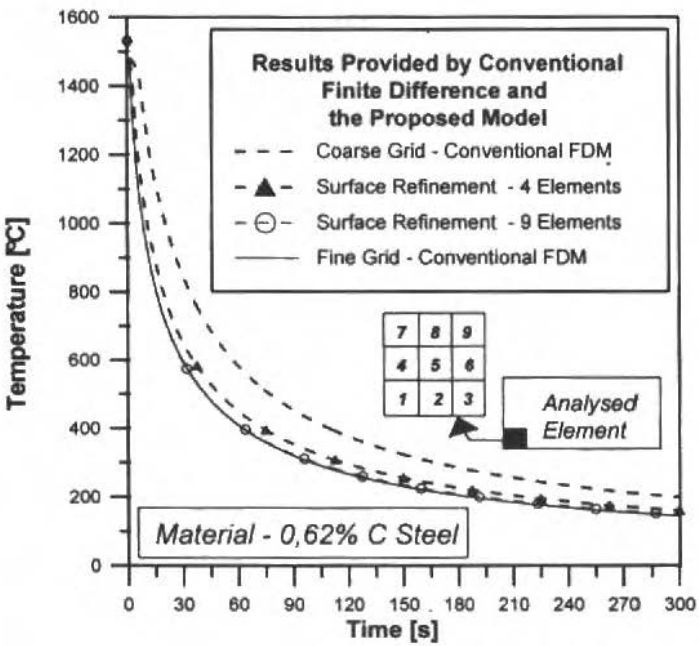

Fig. 12 Comparison of the Proposed Model with Fine Grid Conventional Finite Difference Method Predictions

The main advantage of a local mesh refinement consists on higher simulation velocities, as well as on significant savings in computer memory storage. Table 2 shows the input data used on simulations and characteristics of computer processing. It can be seen that the computational time required for the coarse grid solution is 27 times higher than that necessary to yield the refinement on surface solution (9 Elements), and the consequent computer storage requirement is 4 times higher.

Figure 13 shows the results of cooling curves simulated for different elements from the mesh subjected to a refinement on surface with 9 elements, and compared to the cooling curve for the case of a non-refined grid (element at corner of the cooled region). The physical coherency of the relative position of the resulting curves can also be observed in Fig. 13.

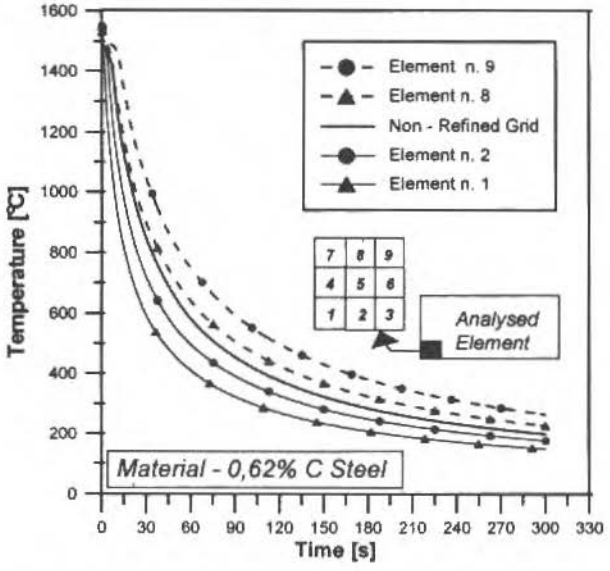

Fig. 13 Comparison of Simulated Cooling Curves Refinement on Surface - 9 Elements and Coarse Grid

Table 2 Simulation Data and Processing Characteristics

Material: Carbon Steel	%C = 0.62	
Ingot Dimensions (m)	Cooling Temperature (K)	Heat Transfer Coefficients (W/m².K)
Lx = 0.20 Ly = 0.15 dz = 0.01	Tox = 308 Toy = 303	hox = 1000 hoy = 2100

Processing Results

Elements from the Mesh	Total Number of Elements	Computer Storage (Bytes)	Computational Time (s)
Nx = 20; Ny = 10 (Coarse)	200	800	74
Nx = 60; Ny = 30 (Refined)	1800	7200	6200
Nx = 20; Ny = 10 (Refinement on Surface) 4 Elements	287	1148	118
Nx = 20; Ny = 10 (Refinement on Surface) 9 Elements	432	1728	230

A similar comparison is shown in Fig. 14, for elements situated 10 cm away from the corner of the cooled region, in the X and Y directions.

In order to verify the model performance for the case of materials of higher thermal diffusivities, some simulations were performed with an aluminum-copper alloy (Al-4,5%Cu). The results can be seen on Fig. 15 where the proposed model predictions are presented for the cases of refinement on surface with 4 and 9 elements and for a fully refined grid with 9 and 49 elements. The resulting performance is

similar to that observed at the previous analysis with steel. Table 3 shows the input data used on simulations and characteristics of computer processing.

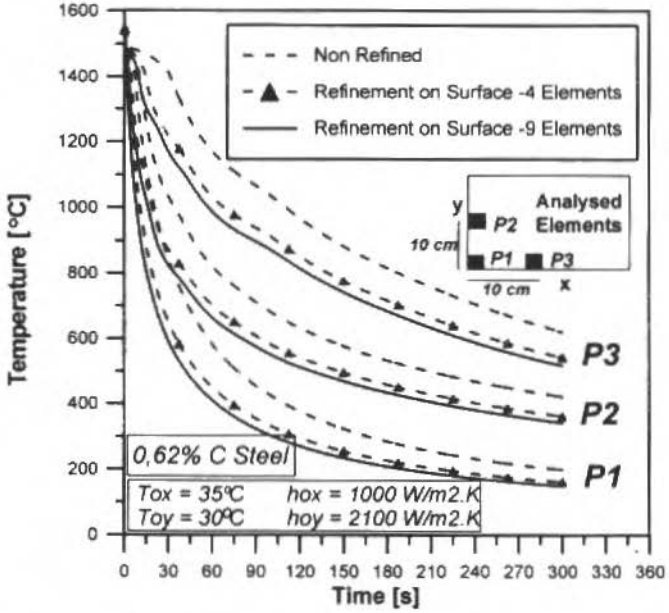

Fig. 14 Comparison of Simulated Results Proposed Model and Non- Refined Grid

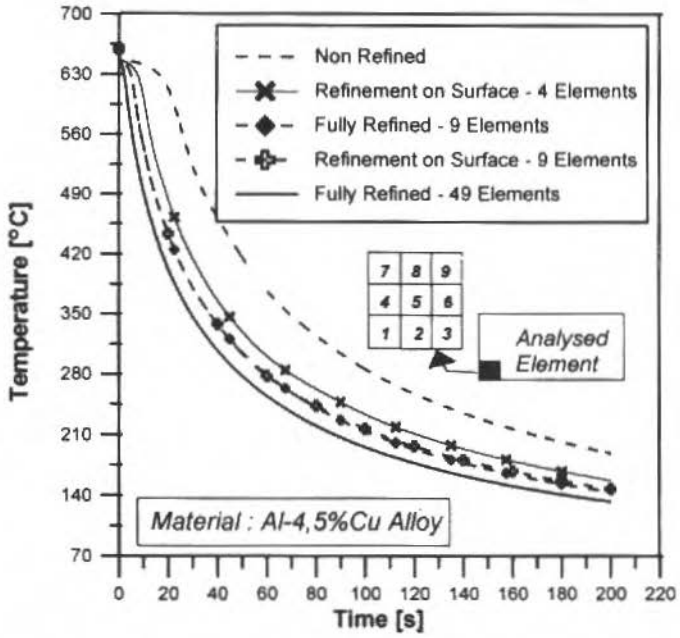

Fig. 15 Comparison of Simulated Results Proposed Model and Non-Refined Grid

Table 3 Simulation Data and Processing Characteristics

Material: Al-4,5%Cu Ingot Dimensions (m)	Cooling Temperature (K)	Heat Transfer Coefficients (W/m².K)
Lx = 0.20 Ly = 0.15 dz = 0.01	Tox = 308 Toy = 303	hox = 2100 hoy = 1500

Processing Results			
Elements from the Mesh	Total Number of Elements	Computer Storage (Bytes)	Computational Time (s)
Nx = 5; Ny = 5 (Non-Refined)	25	100	68
Nx = 15; Ny = 15 (Fully Refined- 9 Elements)	225	900	491
Nx = 35; Ny = 35 (Fully Refined-49 Elements)	1225	4900	10820
Nx = 5; Ny = 5 (Refinement on Surface) 4 Elements	52	208	205
Nx = 5; Ny = 5 (Refinement on Surface) 9 Elements	97	388	263

Conclusion

The proposed model has proved to be efficient, versatile and easy of manipulation, as can be seen by the presented mathematical development. It can be applied to complex shaped domains with a good numerical accuracy and substantial savings in computational time and computer storage requirements. The coupling of elements from the fine grid with those from the coarse grid has been validated by using the Thermal/Electrical Analogy. This approach should be of considerable use in describing real foundry situations.

Acknowledgment

The authors would like to acknowledge the financial support provide by FAPESP (The Scientific Research Foundation of the State of São Paulo).

References

Holman, J. P., 1983, "Heat Transfer", by *McGraw-Hill, Inc.* New York.

Incropera, F. P. and Witt, D. P., 1981, "Fundamentals of Heat and Mass Transfer", 3° Ed., *John Wiley & Sons*, New York.

Kingery, W. D., Bowen, H. K. and Uhlmann, D. R., 1976, "Introduction to Ceramics", 2° Ed., *John Wiley & Sons*, New York.

Metals Handbook, 1989; *Aluminum Alloys*, 8ª Ed., V.I, pp. 948.

Patankar, S. V., 1980, "Numerical Heat Transfer and Fluid Flow", *Hemisphere Publishing Corporation*.

Phillips, R. E. and Schimidt, F. W., 1984, "Multigrid Techniques for the Numerical Solution of the Diffusion Equation", *Numerical Heat Transfer*, V.7, pp. 251-268.

Ramakrishna, R., P.; 1984, "Efficient Numerical Method for Two-Dimensional Phase Change Problems", *International Journal Heat Mass Transfer*, V.11, n° 11, pp. 2077-2084.

Spim Jr , J. A., 1996, "Aplicação da Modelagem Matemática da Solidificação no Controle Ótimo do Lingotamento Contínuo de Aços", *PhD Thesis, UNICAMP/FEM/DEMA*.

Spim Jr., J. A., 1993, "Aplicação da Modelagem Matemática da Solidificação no Controle Ótimo do Lingotamento Contínuo de Aços", *M. Sc. Dissertation, UNICAMP/FEM/DEMA*.

Spim Jr., J. A. and Garcia, A., 1992, "Modelagem Numérica da Solidificação Baseada na Analogia entre Sistemas Térmicos e Elétricos", *10° Congresso Brasileiro de Engenharia e Ciência dos Materiais - CBECIMAT*, V.2, pp. 594-597.

Voller, V.R. and Swaminathan, C.R., 1991, "General Souce-Based Method for Solidification Phase Change", *Numerical Heat Transfer*, Part B, V.19, pp. 175-189.

Wahburn, E. W., 1972, International Critical Tables, V. 5, Ed. *McGraw-Hill Co.*, New York.

Welty, J. R., 1976, "Engineering Heat Transfer", *J. Wiley and Souns*, Inc. New York.

RBCM - J. of the Braz. Soc. Mechanical Sciences
Vol. XIX - No.3 - 1997 - pp. 410-425

ISSN 0100-7386
Printed in Brazil

Análise do Comportamento de Rebolos Convencionais na Retificação de Aços Frágeis e Dúcteis

Behavior Analysis of Conventional Grinding Wheel in Brittle and Ductile Steels Machining

Eduardo Carlos Bianchi
Odilson Coimbra Fernandes
Octávio Mogami
Carlos Elias da Silva Júnior
Ivan De Domenico Valarelli
UNESP - Universidade Estadual Paulista
Faculdade de Engenharia e Tecnologia - Campus de Bauru
Departamento de Engenharia Mecânica

Paulo Roberto Aguiar
Departamento de Engenharia Elétrica
17033-360 Bauru, SP Brasil

Abstract

The aim of this work war to study the behavior of the plan tangential grinding process with conventional grinding wheels, under several machining conditions and a selected dressing condition. The analysis of the grinding performance was done regarding the cutting surface wear behavior of the grinding wheel for brittle and ductile steels workpieces. The grinding input parameters, which were, cutting speed, workpiece speed and cutting feed, were chosen based on the grinding machine characteristics. The results discussion emphasized the wear mechanism of the grinding wheel cutting surface and the cutting phenomenology of the grinding process.
Keywords: *Machining Conditions, Conventional Grinding Wheels, Grinding Wheel Wear.*

Resumo

Neste trabalho foi estudado o comportamento do processo de retificação plana com rebolos convencionais, submetido a diversas condições de usinagem e de uma condição de dressagem. O comportamento quanto ao desgaste da superfície de corte, durante a retificação de aços frágeis e dúcteis, também foi analisado. Os parâmetros de entrada (velocidade de corte, velocidade da peça e penetração do rebolo na peça) que definem uma condição de usinagem, foram escolhidos em função das características da máquina retificadora.
Palavras-chave: *Condições de Usinagem, Rebolos Convencionais, Desgaste de Rebolos*

Introdução

Durante os últimos anos os requisitos de qualidade e funcionalidade dos componentes fabricados industrialmente tem aumentado significativamente. Como conseqüência, os componentes tem sido fabricados com melhor qualidade, e mais rapidamente, para compensar o custo do material utilizado e o processo de usinagem. O custo de produção é substancialmente agravado na usinagem de peças com geometria complexa (Westkämper e Tönshoff, 1993).

A concorrência estrangeira está obrigando as indústrias nacionais a atender aos padrões internacionais de qualidade e desempenho de um produto. Isto implica no conhecimento detalhado de aspectos básicos que vão desde o projeto até a fabricação das máquinas e equipamentos.

Na fabricação de máquinas e equipamentos de precisão são utilizadas peças com tolerâncias controladas (dimensionais e de forma) e rugosidade superficial de pequena magnitude. Essas peças são obtidas, normalmente, através da operação de retificação de precisão, a qual deve proporcionar mínimo custo e máxima produção (Bianchi et al., 1996).

Um dos processos de acabamento mais utilizados na fabricação de peças de precisão é o processo de retificação apesar de o mesmo ser um dos processos menos dominado tecnologicamente, se

Manuscript received. November 1996. Technical Editor Paulo Eigi Miyagi

comparado aos processos convencionais de usinagem. Esse processo também tem a função de solucionar os problemas de qualidade e tempo de toda a seqüência de fabricação (Kegg, 1983).

O desempenho da operação de retificação é muito dependente da habilidade e sensibilidade do operador, e das condições de usinagem e dressagem do rebolo (afiação). A otimização desta operação de usinagem não pode ser obtida alterando-se apenas um parâmetro de entrada do processo. Normalmente, o operador é responsável por decidir, através do método de tentativas e erros, sobre os procedimentos aos quais as peças devem ser submetidas para sua confecção.

Um exemplo característico dos problemas que podem ocorrer durante uma operação de retificação, do tipo cilíndrica externa, está relacionado aos seus parâmetros de entrada. Imagine-se um operador que verifica um aumento excessivo na rugosidade da peça. Por iniciativa própria ele decide que, para eliminar este problema sem comprometer o tempo de fabricação, deve aumentar a velocidade de corte do processo. Entretanto, essa alteração eleva a temperatura na região de corte provocando queima na superfície da peça. Para resolver esse novo problema, ele melhora a refrigeração da operação, aumentando a pressão e a vazão do fluido de corte. Não conseguindo resolver o problema de queima com esta atitude, opta por aumentar a velocidade periférica da peça. Isto eleva o nível de vibrações, por desbalanceamento da peça, provocando maiores danos na superfície da mesma. Como estas alterações não proporcionaram a diminuição da rugosidade, o operador resolve diminuir a velocidade de corte. Com isto, é diminuída a dureza dinâmica do rebolo que passa a desgastar-se mais e irregularmente, provocando erros de forma na peça, que antes não existiam.

Este exemplo mostra que o desempenho desejado de uma operação de retificação não pode ser obtido alterando-se apenas um dos parâmetros de entrada, mas uma combinação bem elaborada de todos os parâmetros envolvidos, simultaneamente (König, 1980).

Conhecendo-se o comportamento do processo de retificação, pode-se interpretar melhor a operação que está sendo realizada em uma peça e proceder às modificações no processo que possibilitem atingir os resultados desejados.

Nomenclatura

a = penetração do rebolo na peça [μm]
a_d = profundidade de dressagem [mm]
A_{sd} = área de dressagem [mm^2]
b = largura média do topo dos grãos abrasivos [mm]
b_d = largura de atuação do dressador [mm]
d_s = diâmetro externo do rebolo [mm]
F_{tf} = força tangencial de corte final [N]
F_{tm} = força tangencial de corte média da última passada [N]
F_{tlg} = força tangencial de corte em um grão abrasivo [N]
G = relação entre Z_w e Z_s [--]
h_{eq} = espessura equivalente de corte [μm]
h_{max} = espessura teórica máxima do cavaco [μm]
K_n = tensão de escoamento do metal da peça [N/mm^2]
K_s = pressão específica de corte [N/mm^2]
L = espaçamento médio entre os grãos abrasivos [mm]
l_c = comprimento de contato entre o rebolo e a peça [mm]
n_m = rotação média em cada passada [rpm]
P_c = potência de corte [W]
P_{ci} = potência de corte instantânea [W]
P_{cm} = potência de corte média[W]
Q_w' = taxa de remoção específica de metal no tempo [mm^2/s]
R_a = rugosidade superficial da peça [μm]
R_{af} = rugosidade superficial obtida na última passada de cada ensaio [μm]
S_d = passo de dressagem [mm/volta]
U_d = grau de recobrimento de dressagem [--]
V_s = velocidade de corte [m/s]
V_w = velocidade da peça [m/s]
Z_w = volume de metal removido [mm^3]
Z_s = volume de rebolo gasto [mm^3]
μ = coeficiente de atrito entre o grão e a peça [--]

O objetivo deste trabalho é estudar experimentalmente o comportamento do processo de retificação tangencial plana com rebolos convencionais, submetido à diversas condições de usinagem e uma única condição de dressagem, e analisar seu desempenho, quanto ao desgaste da superfície de corte, durante a retificação de aços frágeis e dúcteis. Os parâmetros de entrada: V_s [m/s] - velocidade de corte, V_w [m/s] - velocidade da peça e a [μm] - penetração do rebolo na peça, foram escolhidos em função das

características da máquina retificadora. Os resultados obtidos são apresentados e discutidos, dando-se maior ênfase aos mecanismos de desgaste da superfície de corte do rebolo e à fenomenologia de corte do processo de retificação.

Aspectos Teóricos sobre as Condições de Usinagem no Processo de Retificação do Tipo Tangencial Plana

O processo de retificação é muito sensível às condições de usinagem e dressagem. Tendo como objetivo facilitar o entendimento do comportamento das condições de usinagem do processo de retificação, serão apresentadas algumas considerações teóricas sobre a influência de cada parâmetro relacionado às condições de usinagem (Bianchi, 1990; Bianchi, 1992).

No processo de retificação tangencial plana de mergulho a peça é fixada sobre uma placa magnética, que permanece presa sobre a mesa da máquina retificadora. A peça possui movimento longitudinal pendular com velocidade V_w. O rebolo, de diâmetro externo d_s [mm], possui uma velocidade de corte V_s, e penetra na peça com profundidade a, conforme é apresentado (esquematicamente) na Fig. 1.

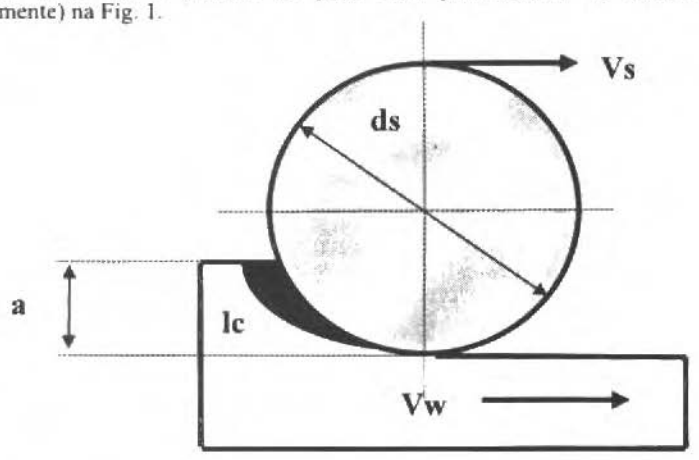

Fig. 1 Representação do Processo de Retificação do Tipo Tangencial Plana de Mergulho

Influência da Profundidade de Corte: a

A eficiência do processo de retificação e a integridade superficial da peça são afetadas pela deflexão que ocorre entre o rebolo e a peça. Esta deflexão aumenta com a área de contato e com o número de grãos em contato com a peça.

A temperatura na superfície da peça, depende do comprimento de contato entre o rebolo e a peça l_c [mm]. A determinação do comprimento de contato é importante para a determinação da máxima temperatura na superfície da peça, da tensão superficial e do desgaste do rebolo (Rowe, 1993).

A penetração do rebolo na peça (a) e o diâmetro externo do rebolo (d_s) estão relacionados ao comprimento de contato entre o rebolo e a peça (l_c), o qual é determinado pela equação (König, 1980):

$$l_c = (a\, d_s)^{0.5} \qquad (1)$$

Um aumento na profundidade de corte, causa um aumento no número de grãos ativos e no tempo de contato, nesta região, fazendo com que cada grão abrasivo remova uma quantidade menor de metal. Os

cavacos resultam mais alongados e finos. Há uma maior parcela de atrito e riscamento, desde o início da formação do cavaco até sua expulsão. Desta forma, o atrito e riscamento entre os cavacos removidos e a peça elevam a temperatura na região de corte tendo como conseqüência a elevação de: rugosidade da peça, nível de emissão acústica e forças de corte (tangencial e normal).

Influência da Velocidade de Corte: V_s

A velocidade de corte V_s exerce uma substancial influência sobre o comportamento das forças de corte, desgaste do rebolo, acabamento e queima superficial da peça, vibrações da máquina, dentre outros.

Quando a velocidade de corte é elevada, um mesmo grão abrasivo passa a remover um menor volume de cavacos, pelo aumento da sua freqüência de contato com a peça. Portanto o número de grãos ativos é maior. A espessura dos cavacos removidos é menor, diminuindo as forças de corte, rugosidade da peça e desgaste do rebolo, pela menor solicitação sobre cada grão abrasivo. Assim, o rebolo apresenta uma aparente elevação da sua dureza dinâmica, já que cada rebolo possui uma dureza estática característica (fornecida pelo fabricante). Entretanto, pelo aumento da intensidade de contato dos grãos com a peça, ocorre uma elevação da temperatura, a qual pode ocasionar a queima da peça.

Influência da Velocidade da Peça: V_w

A velocidade da peça V_w é coincidente com a velocidade da mesa da máquina retificadora, no caso de retificação tangencial plana de mergulho. Esta velocidade está relacionada aos impactos que os grãos abrasivos provocam na peça.

Pode-se analisar a influência da velocidade da peça na operação de retificação de duas formas, conforme apresentado na Fig. 2.

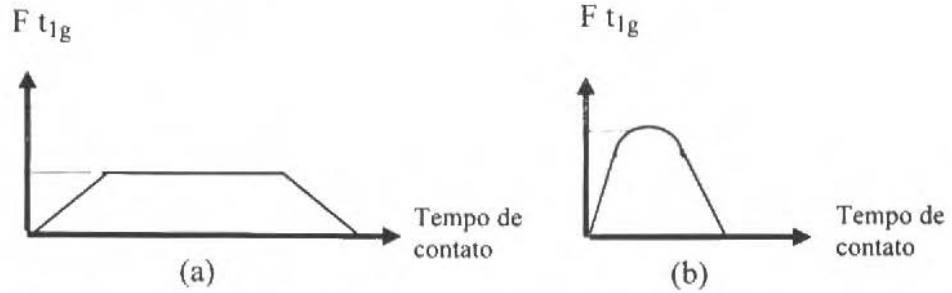

Fig. 2 Influência do Tempo de Contato na Força Tangencial de Corte em um Grão Abrasivo F t_{lg}

a. Quando a velocidade da peça é baixa e a penetração do rebolo na peça é grande. Neste caso, os impactos dos grãos abrasivos do rebolo sobre a peça são pequenos e os cavacos são alongados. O tempo de contato grão/peça e o número de grãos ativos, são maiores. Assim, a força em um grão abrasivo é pequena e atua durante um tempo longo (Fig. 2a). Os grãos abrasivos tendem a permanecer mais tempo em contato com a peça o que provoca um desgaste maior. As forças de corte (normal e tangencial) tendem a aumentar com o tempo de retificação, pelo desgaste das arestas cortantes. Com isto o desgaste do rebolo tende a ser menor, considerando-se que os grãos abrasivos permanecem mais tempo presos ao ligante, o que minimiza a perda de grãos.

b. Quando a velocidade da peça é alta e a penetração do rebolo na peça é pequena. Os impactos dos grãos abrasivos do rebolo sobre a peça são grandes e os cavacos são curtos. O tempo de contato grão/peça e o número de grãos ativos são menores, gerando uma força por grão abrasivo grande e por pouco tempo (fig. 2b). Os grãos tendem a se fraturar e a se desprender da superfície de corte do rebolo. Neste caso as forças totais de corte tendem a uma estabilização pela troca constante de grãos abrasivos. O desgaste do rebolo tende a ser maior que no caso anterior.

Parâmetros Relacionados ao Processo de Retificação

Espessura Equivalente de Corte e Espessura Teórica Máxima do Cavaco

A espessura equivalente de corte h_{eq} [μm] representa a espessura da camada de metal que é arrancada pelo rebolo numa volta completa. Trata-se de um parâmetro que permite quantificar uma condição de trabalho, a partir dos parâmetros de entrada (V_s, V_w, a). A espessura equivalente de corte, definida como sendo a relação entre a taxa de remoção específica de metal no tempo e a velocidade de corte, é, expressa por (Peters e Decneut, 1975):

$$h_{eq} = Q_w' / V_s = (a \cdot V_w / V_s) \quad (2)$$

A taxa de remoção específica de metal no tempo Q_w' [mm²/s] é determinada pelo produto entre a penetração do rebolo na peça e a velocidade desta. O parâmetro h_{eq} está diretamente relacionado com o comportamento do processo de retificação em função de variáveis envolvidas, como: forças de corte, rugosidade, vida da ferramenta, etc.

A espessura teórica máxima do cavaco h_{max} [μm] é diretamente proporcional ao parâmetro espessura equivalente de corte, conforme a equação (Bianchi et al., 1992):

$$h_{max} = h_{eq} \cdot (2 \cdot L / l_c) \quad (3)$$

onde L [mm] é o espaçamento médio entre os grãos abrasivos.

Portanto, aumentando-se h_{eq} e/ou diminuindo-se l_c, há um aumento na espessura máxima do cavaco arrancado. Todavia, variando-se a espessura do cavaco arrancado, altera-se a força tangencial de corte num grão abrasivo. Esta força tangencial de corte pode ser expressa pela equação (Bianchi et al., 1992):

$$F_{tg} = b \cdot h_{max} \cdot K_s + \mu \cdot b \cdot \pi \cdot K_n / 4 \quad (4)$$

sendo b [mm] a largura média do topo dos grãos abrasivos, K_s [N/mm²] a pressão específica de corte, μ o coeficiente de atrito entre o grão e a peça e K_n [N/mm²] a tensão de escoamento do metal da peça.

Relação G

O desempenho de um rebolo pode ser avaliado através da relação G, definida como sendo a relação entre volume de metal removido Z_w [mm³] e volume de rebolo gasto Z_s [mm³], conforme equação (Hahn, 1955):

$$G = Z_w / Z_s \quad (5)$$

Dressagem da Superfície de Corte do Rebolo

O mecanismo cinemático para a operação de dressagem consiste no deslocamento do dressador transversalmente ao rebolo em movimento de rotação. O dressador penetra no rebolo a uma certa profundidade de dressagem a_d [mm], a qual implica numa largura de atuação do dressador b_d [mm]. Desta forma, ao deslocar-se o dressador com um determinado passo de dressagem S_d [mm/volta], o rebolo será dressado removendo-se partículas de grãos abrasivos equivalentes à área de dressagem A_{sd} [mm²], conforme é apresentado na Fig. 3.

A operação de dressagem modifica as características topográficas dos rebolos convencionais pela geração do macro e microefeito de dressagem. O macroefeito corresponde à rosca gerada na superfície de corte do rebolo e o microefeito ao estado de afiação de cada grão abrasivo (Bianchi, 1990).

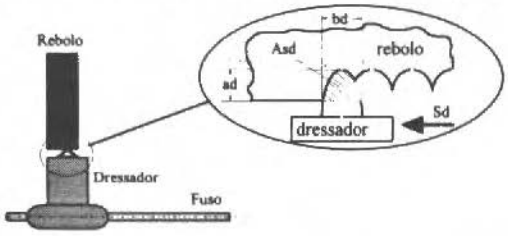

Fig. 3 Forma Esquemática da Operação de Dressagem de Rebolos Convencionais com Dressador do Tipo Ponta Única

O parâmetro grau de recobrimento de dressagem U_d ($U_d = b_d/S_d$) representa a forma com que o rebolo está sendo dressado. Quando um rebolo é dressado com grau de recobrimento de dressagem próximo à unidade, os valores do macro e microefeito de dressagem são máximos. De maneira oposta, quanto maior for o valor do valor do grau de recobrimento de dressagem, menores serão aqueles valores.

Durante a operação de dressagem os grãos com pouca ancoragem soltam-se, e os que estão bem aderidos na superfície de corte do rebolo são fraturados. O ligante também sofre as conseqüências da operação de dressagem, fraturando-se proporcionalmente à sua tenacidade. Se a tenacidade do ligante for pequena, a tendência é liberar grãos da superfície de corte do rebolo com maior intensidade do que no caso onde o ligante possui maior tenacidade.

Procedimentos Experimentais

Para a verificação experimental da influência dos parâmetros de entrada do processo de retificação do tipo tangencial plana de mergulho, foi desenvolvido um banco de ensaios específico onde os parâmetros de entrada pudessem ser controlados. Descreve-se a seguir o prosseguimento de medição experimental da força tangencial de corte.

Medição da Potência de Corte: P_c

A Figura 4 mostra um esquema geral do Banco de Ensaios desenvolvido para a realização dos experimentos.

O corpo de prova, em formato de "T", com largura menor que o rebolo, é fixado diretamente sobre a placa magnética.

No início de cada ensaio, o rebolo é dressado numa condição específica e idêntica para todos os ensaios. Isto permite que a influência da operação de dressagem seja minimizada. Consequentemente, os resultados refletem melhor o comportamento das variáveis de saída (potência de corte, rugosidade superficial da peça, desgaste do rebolo e volume de material removido).

A potência do motor de indução é transmitida à polia de acionamento, que está ligada ao eixo árvore da máquina retificadora. Um torquímetro, posicionado entre o motor e a polia de acionamento, faz a leitura do torque total instantâneo necessário para a realização da operação de retificação. Acoplado ao eixo árvore, que suporta o rebolo, é fixado um "encoder" que faz a leitura da rotação instantânea deste. Esta rotação é alterada, de acordo com as necessidades de cada condição de ensaio, por um inversor de freqüência. Os valores de tensão, proporcionais ao torque e rotação, são recebidos, simultaneamente, pelo microcomputador através de uma placa A/D de aquisição de dados. A potência total instantânea solicitada pela operação é obtida através do produto: torque total x rotação. A potência de corte instantânea (P_c), em cada ponto da peça, é obtida subtraindo-se da potência total instantânea, a

potência média em vazio. Esta última é obtida determinando-se os valores da rotação e torque em vazio, por um determinado tempo, e calculando-se o valor médio dos produtos de ambos.

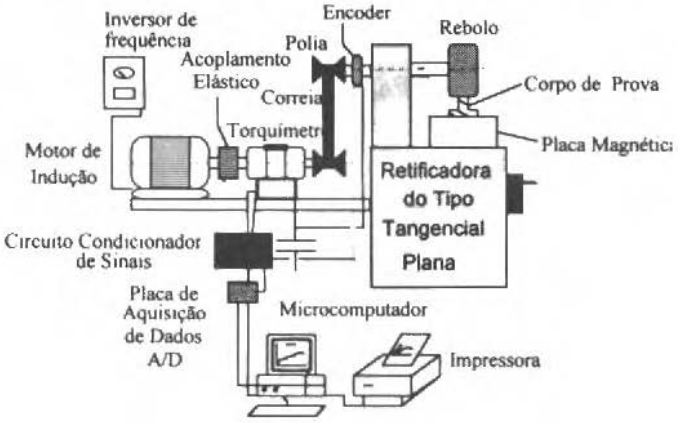

Fig. 4 Esquema Geral do Banco de Ensaios Utilizado

A potência de corte média (P_{cm}), em cada passada, é obtida pela média dos valores da potência de corte instantânea em cada ponto.

O "software" desenvolvido, para o gerenciamento do banco de ensaios, é responsável pela aquisição dos dados de ensaio, tratamento destes e determinação dos valores da potência de corte (P_c) instantânea e média, em [W], por passada.

Os valores de rugosidade superficial (R_a [μm]) foram medidos por um rugosímetro portátil e registrados via teclado.

Os ensaios foram realizados com rebolo de granulometria média AA 46 K V e aço ABNT 1045-58 HRc - temperado e rebolo de granulometria fina AA 120 M6 V15 e aço ABNT 1020. Para ambos os casos foi adotado grau de recobrimento de dressagem unitário. Os parâmetros de entrada utilizados foram adequados para a obtenção de duas espessuras equivalentes de corte h_{eq} = 0,02 μm e h_{eq} = 0,06 μm, respectivamente, as quais foram mantidas constantes durante os ensaios.

Resultados e Discussão

Os resultados dos ensaios são mostrados em figuras que agrupam 6 ensaios cada, variando-se os parâmetros de entrada. São apresentados na forma de curvas de potência de corte média e rugosidade superficial da peça em função do volume de material removido. Posteriormente é feita uma comparação entre as variáveis de saída, envolvendo os 6 ensaios simultaneamente.

Resultados Obtidos com Rebolo AA 46 K V e Aço ABNT 1045 - 58 HRc - Temperado, com h_{eq} = 0,02 μm

O mecanismo de desgaste dos rebolos convencionais consiste na elevação da potência de corte causada pela perda do macro e microefeito, decorrentes da operação de dressagem. Inicialmente a densidade de grãos ativos é menor, e cada grão abrasivo remove uma quantidade maior de material. Assim, a potência necessária para remover material, por grão abrasivo, é maior.

Com a perda do macro e microefeito de dressagem, há um aumento da densidade de grãos ativos na região de contato entre o rebolo e a peça. Logo, cada grão abrasivo passa a remover um volume menor de material. A potência consumida por grão abrasivo é menor. Entretanto o somatório das perdas dissipativas (devido ao atrito e riscamento dos grãos abrasivos sobre a peça, emissão acústica, geração

de calor, dentre outras) é maior, e proporcional ao desgaste da superfície de corte do rebolo, pelo aumento das áreas no topo dos grãos (por abrasão), o que eleva a potência de corte média.

Na Figura 5 são apresentados os resultados de potência de corte média e rugosidade superficial da peça, em função do volume de material removido, obtidos com o rebolo AA 46 K V, aço ABNT 1045 - 58 HRc - temperado h_{eq} = 0,02 μm. O valor R_{af} [μm], que aparece na legenda das figuras, corresponde ao valor da rugosidade superficial obtida na última passada de cada ensaio. O valor F_{tf} [N], que aparece na legenda das figuras, corresponde ao valor da força tangencial de corte média (F_{tm} [N]), da última passada. Em cada passada a força tangencial de corte média é calculada pela relação:

$$F_{tm} = (P_{cm})/(n_m).(d_s/2) \qquad (6)$$

onde n_m é a rotação média em cada passada.

A potência de corte média tende a estabilizar-se pela renovação da superfície de corte do rebolo, através do equilíbrio entre a capacidade de retenção do ligante sobre os grãos abrasivos e a potência de corte média necessária para a remoção do material. Quando a força corte média é maior que a capacidade de retenção do ligante sobre o grão, este é expulso. Devido a isto, novos grãos afiados (que ainda não foram utilizados) surgem, mantendo a agressividade da superfície de corte do rebolo (capacidade da superfície de corte do rebolo em remover material). Isto ocorreu em quase todos os ensaios em que foi utilizado um rebolo de dureza K, classificado como mole, o qual permite a liberação dos grãos da superfície de corte (auto-afiação) com maior facilidade, se comparado a rebolos duros que possuem maior capacidade de retenção dos grãos abrasivos.

A potência de corte média eleva-se devido ao aumento da força tangencial por grão: a largura média do topo dos grãos abrasivos, b, cresce devido ao desgaste dos mesmos, compensando a diminuição da espessura teórica máxima do cavaco, h_{max}, causada pelo aumento da densidade de grãos ativos na região de contato (L menor).

Os ensaios mostraram que a rugosidade superficial da peça, inicialmente alta, decresce com o aumento do número de grãos ativos. Isto faz com que os esforços de corte médios sejam melhor distribuídos por grão, além de gerar um número maior de cavacos (com menor espessura teórica máxima), por unidade de tempo. Em alguns casos a rugosidade superficial da peça, baixa no início da operação de retificação, manteve-se baixa, com pouco decréscimo, até o final do ensaio.

Conforme a Eq. (2), para que h_{eq} seja constante, a elevação da velocidade de corte deve ser acompanhada por uma maior taxa de remoção específica de material no tempo ($Q_w' = a \cdot V_w$), garantindo-se assim a capacidade de produção de peças numa empresa. Entretanto, da Eq. (3), pode-se concluir que se o comprimento teórico do cavaco aumentar, sua espessura teórica máxima diminui. O aumento do comprimento teórico do cavaco é conseguido por um aumento da penetração do rebolo na peça (Eq. 1). Desta forma, a força tangencial de corte por grão abrasivo é menor, conforme a Eq. (4). Porém, o aumento da penetração do rebolo na peça, está relacionado ao maior tempo de permanência do grão abrasivo na superfície de corte do rebolo, o que aumenta a largura média do topo dos grãos (b), elevando a força tangencial de corte. Deve-se considerar, para uma análise global, as forças dissipativas que não são representadas na Eq. (4).

A estabilização da potência de corte média, e consequentemente da força tangencial de corte média, ocorreu pela constante renovação dos grãos abrasivos na superfície de corte do rebolo, que deixou o rebolo permanentemente agressivo; ou seja, com capacidade de remoção de material durante todo o tempo.

Os ensaios mostraram que em todos os casos houve uma tendência de crescimento das curvas de potência de corte média. Inicialmente este crescimento foi maior pela perda do macro e microefeito de dressagem. Posteriormente, com o aumento do número de grãos ativos na região de corte, o crescimento das curvas foi menor. As modificações topográficas ocorridas na superfície de corte do rebolo afetaram a geometria dos cavacos gerados.

Nos ensaios 1 e 2, foram mantidas constantes a velocidade de corte (V_s) e a taxa de remoção específica de material no tempo ($Q_w' = a \cdot V_w$). Quando a penetração do rebolo na peça é maior, os esforços de corte são melhor distribuídos entre os grãos abrasivos. Neste caso, a rugosidade superficial

final da peça é menor, pelo aumento do número de grãos ativos na região de contato e geração de cavacos alongados e finos. A potência de corte média é maior pelo aumento das forças dissipativas.

No caso da penetração do rebolo na peça ser menor, a velocidade da peça é maior. Assim os impactos entre os grãos abrasivos e a peça são maiores, gerando cavacos curtos e grossos. Entretanto, como a penetração do rebolo na peça é pequena, os impactos e os cavacos gerados não provocam uma expulsão significativa dos grãos abrasivos da superfície de corte do rebolo. Devido a isto, a relação G resultou maior para o caso de penetração menor do rebolo na peça, mesmo com velocidade da peça maior.

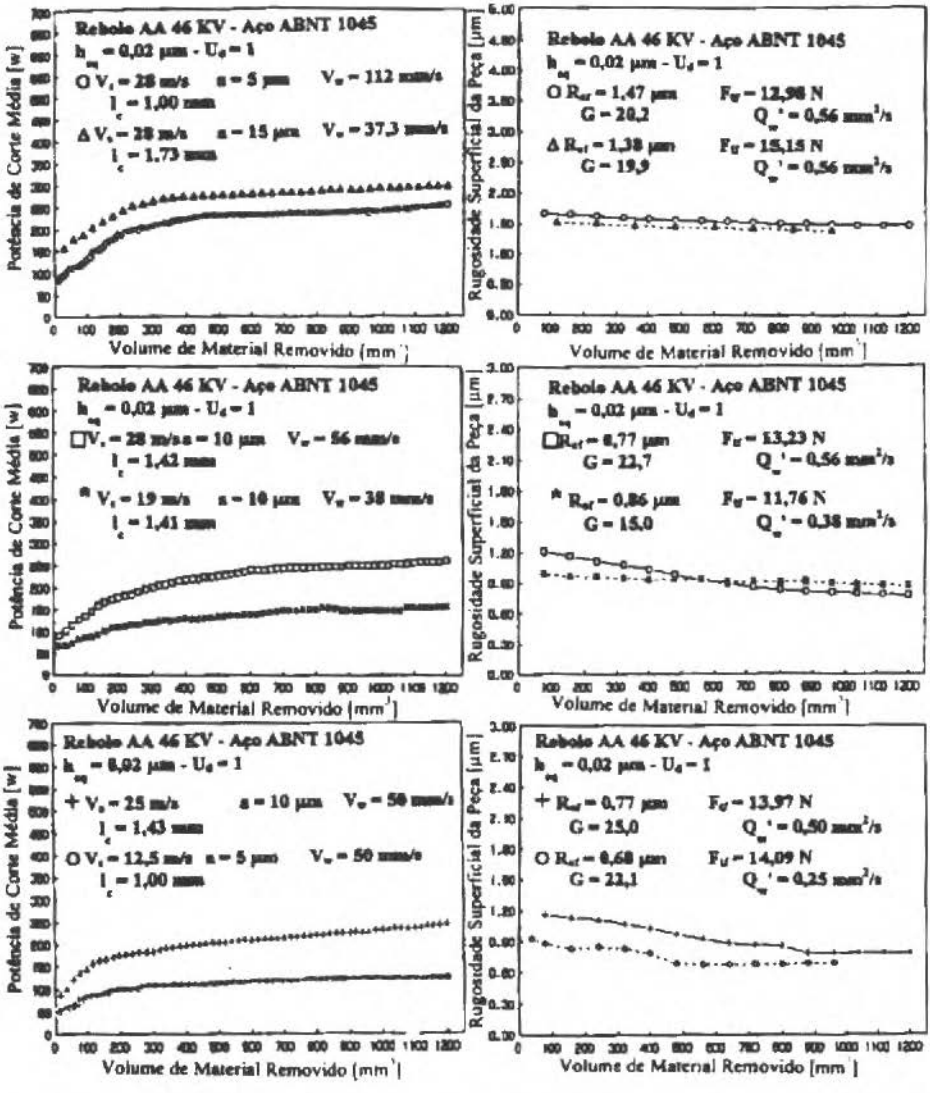

Fig. 5 Resultados de Potência de Corte Média e Rugosidade Superficial da Peça, em Função do Volume de Material Removido, para h_{eq} = 0,02 µm

Nos ensaios 3 e 4, a penetração do rebolo na peça (a) foi mantida constante e variadas a velocidade de corte (V_s), a velocidade da peça (V_w) e a taxa de remoção específica de material no tempo (Q_w'). Com o aumento da velocidade de corte (ensaio 4 para ensaio 3), pela elevação da rotação do rebolo, a potência de corte média e a força tangencial de corte média, aumentaram. A rugosidade final da peça resultou menor quando a velocidade de corte foi maior. Isto ocorre pela menor espessura de corte do cavaco gerado. Na curva 3, a velocidade de corte, a velocidade da peça e a taxa de remoção específica de material no tempo foram maiores. Mesmo assim a relação G foi maior neste caso, pela diminuição da geometria do cavaco gerado.

Nos ensaios 5 e 6, somente a velocidade da peça (V_w) foi mantida constante. Na condição de maior velocidade de corte e maior penetração do rebolo, a rugosidade da peça resultou maior. Com penetração do rebolo maior, são gerados cavacos alongados e com espessura teórica máxima menor. Como o comprimento de contato é maior, as parcelas de energia dissipativa são maiores. A rugosidade final da peça é maior neste caso. Na condição de menor velocidade de corte e menor penetração do rebolo, a taxa de remoção específica de material no tempo é menor. Por conseguinte, o volume dos cavacos gerados por passada da peça sob o rebolo é menor, porém com maior espessura teórica máxima, o que aumenta a força de corte por grão. Assim, o desgaste da superfície de corte do rebolo cresce pela maior intensidade dos impactos e desgaste do ligante pelos cavacos gerados, e pelo aumento da força de corte, fazendo com que a relação G seja menor.

A Figura 6 (6a e 6b) apresenta uma comparação entre as variáveis de saída obtidas nestes ensaios.

Pode-se notar que quando a velocidade de corte e a taxa de remoção específica de material no tempo são constantes (ensaios 1, 2 e 3), a menor rugosidade superficial e o maior valor de G foram obtidos com o ensaio 3 (V_s = 28 m/s, V_w = 56 mm/s e a = 10 μm). Estes três ensaios mostraram, também, que a variação da força tangencial de corte (F_t) acompanha a variação de a. O comportamento de R_a pode ser explicado: O ensaio 3, em comparação aos ensaios 1 e 2, tratou de uma condição intermediária com relação à penetração do rebolo na peça (a) e a velocidade da mesma (V_w). Como conseqüência da variação de a e V_w, o ensaio 1 produziu cavacos grossos e curtos, o ensaio 2 produziu cavacos finos e longos e o ensaio 3 produziu cavacos médios. Os cavacos curtos e grossos, ao saírem, riscam a peça, os cavacos finos e longos, entupindo as porosidades do rebolo, aumentam o atrito, piorando o acabamento superficial; isto explica por que o melhor acabamento foi obtido no ensaio 3.

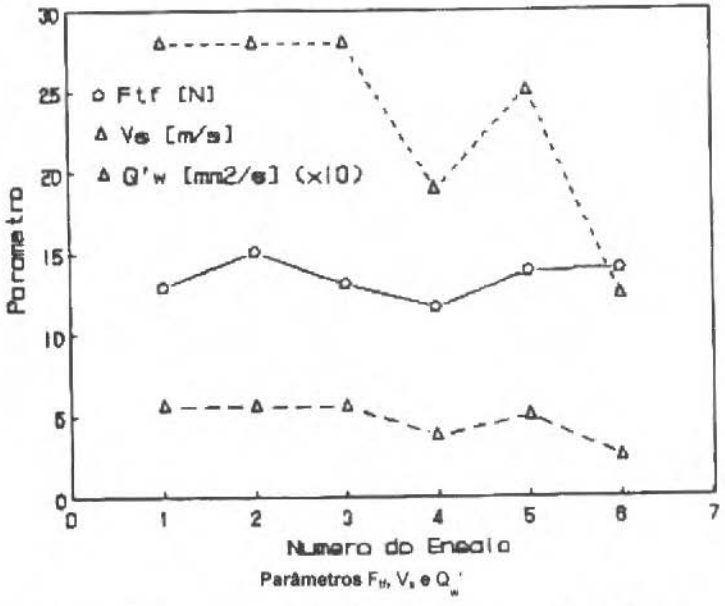

Fig. 6a Comparação entre os Parâmetros de Saída, para h_{eq} = 0,02 μm

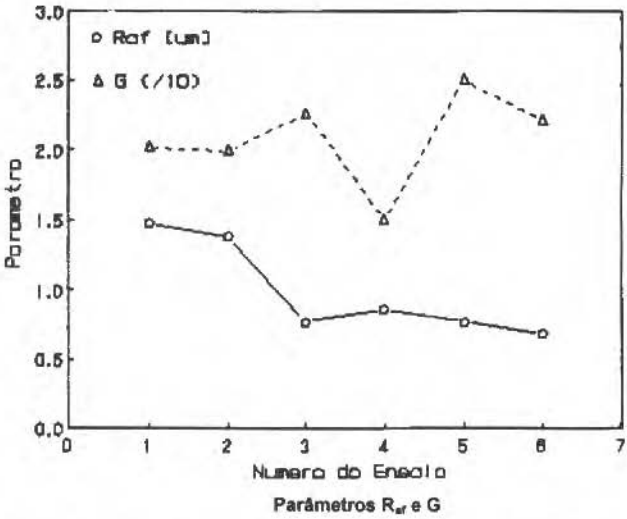

Fig. 6b Comparação entre os Parâmetros de Saída, para h_{eq} = 0,02 μm

O comportamento de G pode ser explicado: No ensaio 1 (a_{min} e $V_{w\,max}$) os impactos dos grãos sobre a peça são elevados provocando o desprendimento dos grãos e, consequentemente, um maior desgaste do rebolo. No ensaio 2 (a_{max} e $V_{w\,min}$) os impactos dos grãos abrasivos sobre a peça são pequenos; porém como o comprimento de contato $[(a.d_e)^{0.5}]$ é grande, a parcela relativa ao atrito e riscamento é elevada, o que provoca o desprendimento de maior número de grãos, aumentando o desgaste do rebolo. Novamente os valores médios do ensaio 3, proporcionaram o melhor valor para G.

A menor rugosidade superficial da peça foi obtida no ensaio 6, com a menor taxa de remoção específica de material no tempo, com a menor velocidade de corte e com o segundo melhor valor obtido para G. Todavia, o custo de fabricação por peça será maior, porquanto a taxa de remoção específica de material no tempo é a menor e, consequentemente, o número de peças usinadas por unidade de tempo, também será menor.

Os três melhores valores da relação G foram obtidos nos ensaios 5, 6 e 3 respectivamente. A penetração do rebolo na peça é a mesma nos ensaios 5 e 3; entretanto, a taxa de remoção específica de material no tempo foi diferente nos três casos. A ordem decrescente da taxa de remoção específica de material no tempo é a dos ensaios 3, 5 e 6. Como o volume de material removido por passada é menor, o tempo, no qual os esforços de corte agem no material por passada, é maior. Os esforços de corte são melhor distribuídos, desgastando menos a superfície de corte do rebolo. Não foram detectados, nestes ensaios, entupimento ou incrustações na superfície do rebolo.

Resultados Obtidos com Rebolo AA 120 M6 V15 e Aço ABNT 1020 (dúctil), com h_{eq} = 0,06 μm

Na retificação de aços dúcteis os cavacos arrancados são mais alongados, em comparação com a retificação de aços frágeis. Rebolos finos possuem porosidades menores que rebolos médios. Assim, os cavacos arrancados encontram maior dificuldade de alojamento nas porosidades do rebolo (para posterior eliminação), principalmente quando se utiliza valores mais elevados de espessura equivalente de corte (h_{eq}).

Para alcançar o objetivo deste trabalho, optou-se por utilizar um outro rebolo com granulometria fina submetido à diversas condições de usinagem e uma única condição de dressagem. Para a viabilização de uma análise comparativa (com o rebolo AA 46 K V), as condições de usinagem foram mais severas.

A Figura 7 mostra os resultados de potência de corte média e rugosidade superficial da peça, em função do volume de material removido, para h_{eq} = 0,06 μm, obtidos na retificação de aços dúcteis com rebolo fino (120 mesh e dureza média M).

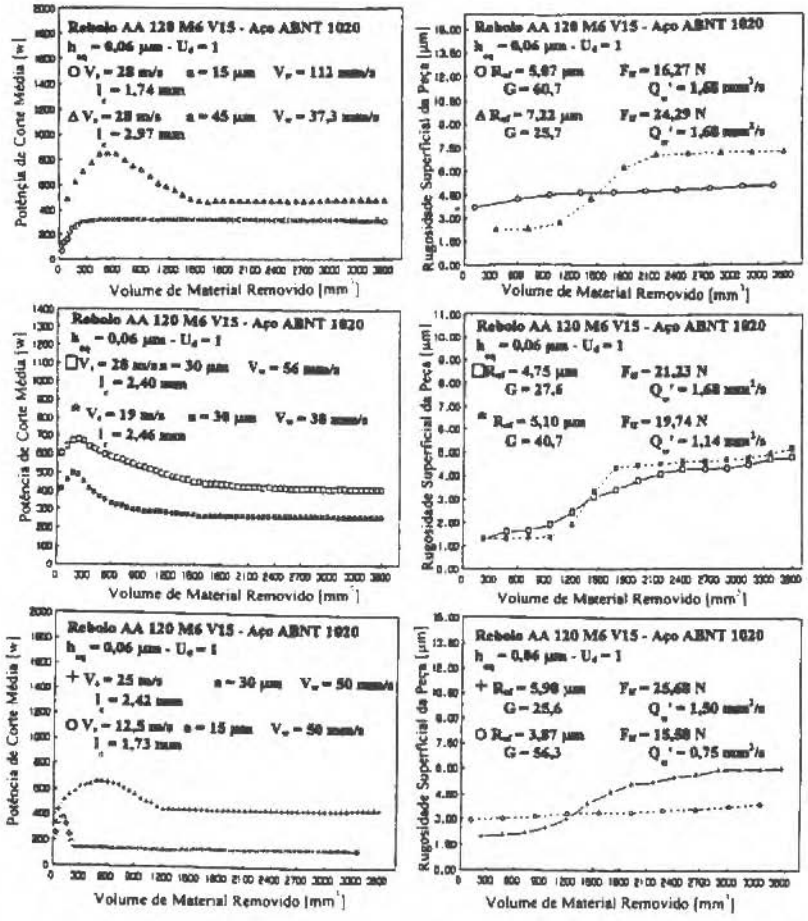

Fig. 7 Resultados de Potência de Corte Média e Rugosidade Superficial da Peça, em Função do Volume de Material Removido, para h_{eq} = 0,06 μm

No ensaio 1, com pouca penetração do rebolo na peça, a potência de corte média cresceu e estabilizou-se. Entretanto, nos demais ensaios a potência de corte média cresceu até um máximo e em seguida decresceu, tendendo a estabilizar-se. Isto ocorreu porque, após uma operação de dressagem, os grãos abrasivos da superfície de corte do rebolo ficam bem ancorados e afiados. Com a perda do macroefeito de dressagem, há um aumento da densidade de grãos ativos na região de contato e da área do topo dos grãos abrasivos. Assim, a potência de corte média tende a crescer até atingir um valor máximo, correspondente ao limite máximo de retenção do ligante sobre os grãos abrasivos. A partir daí os grãos passam a ser arrancados, resultando na diminuição e estabilização da potência de corte média. Esta condição de estabilização, tende a ser alcançada devido ao estado de auto-afiação dos grãos abrasivos na superfície de corte do rebolo.

A rugosidade superficial da peça, em todos os ensaios, mostrou-se inicialmente baixa, pela pouca densidade de grãos ativos na região de contato. Com a perda do macroefeito de dressagem, ocorre um aumento na densidade destes grãos, os quais removem mais cavacos com menor espessura teórica,

porém aumentando o riscamento sobre a superfície da peça. Os cavacos entopem, com mais facilidade, as porosidades do rebolo, colaborando para a elevação da rugosidade superficial da peça.

Nos ensaios, nos quais ficou caracterizado o limite máximo de retenção do ligante sobre os grãos abrasivos, houve um crescimento repentino da rugosidade superficial da peça, correspondendo à renovação dos grãos abrasivos da superfície de corte do rebolo. Grãos novos e afiados removem material com maior facilidade; porém, a densidade destes grãos na região de contato diminui. Assim, cada grão abrasivo remove um volume maior de material, riscando mais a superfície da peça.

A Figura 8 (8a e 8b) apresenta uma comparação entre os parâmetros de saída dos ensaios realizados.

Os valores máximos da força tangencial de corte média por passada ($F_{t\ Max}$) foram maiores nos ensaios 2 e 5. No ensaio 2 a penetração do rebolo na peça foi elevada (45μm) e no ensaio 5, a combinação entre os parâmetros de entrada elevou a potência de corte média.

Nos ensaios onde ocorreu a elevação da potência de corte média até o limite máximo de retenção do ligante sobre os grãos abrasivos, as curvas de rugosidade superficial correspondentes apresentaram uma elevação repentina no instante em que a potência de corte média decresceu. Isto ocorreu pela diminuição da densidade de grãos ativos; cada grão removendo um volume maior de material, risca mais a superfície da peça, aumentando a rugosidade da mesma.

No ensaio 2, a rugosidade superficial da peça foi maior devido ao aumento das parcelas de atrito e riscamento causadas pelos cavacos arrancados que, sendo longos e de pouca espessura, se aquecem rapidamente e entopem as porosidades do rebolo.

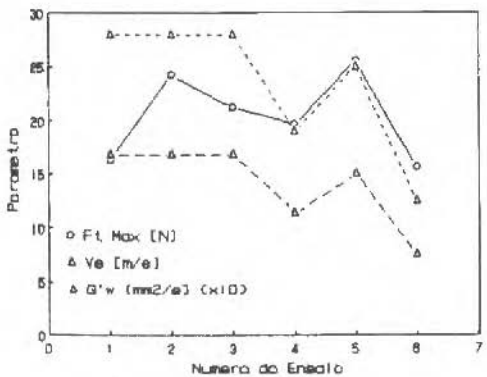

(a) Parâmetros $F_{t\ Max}$, V_e e Q'_w

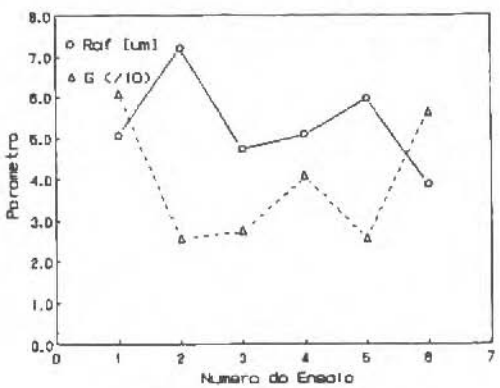

(b) Parâmetros R_a e G

Fig. 8 Comparação entre os Parâmetros de Saída para h_{eq} = 0,06 μm

Os melhores valores da relação G foram obtidos nos ensaios 1 e 6. No ensaio 1 a penetração do rebolo na peça é pequena; os cavacos arrancados são curtos e grossos, não exigindo grande esforço para a remoção de material e, consequentemente, desgastando menos o rebolo. No ensaio 6, embora a penetração seja pequena, a taxa de remoção específica de material no tempo é a menor entre todos os ensaios realizados tendo como conseqüência, um menor desgaste do rebolo.

Os ensaios realizados permitiram montar as Tabelas 1 e 2. Nestas, destacam-se os parâmetros de entrada relacionados ao acabamento superficial da peça R_{af} e relação G.

Tabela 1 Resultados Obtidos com o Rebolo Médio e Aço Frágil

Rebolo AA 46 K V e aço ABNT 1045 - 58 HRc - temperado, com h_{eq} = 0,02 μm

Ensaio	R_{af} [μm]	G	Q_w' [mm²/s]	a [μm]	V_w [mm/s]	V_s [m/s]
1	1.47	20.2	0.56	5	112	28
2	1.38	19.9	0.56	15	37.3	28
3	0.77	22.7	0.56	10	56	28
4	0.86	15.0	0.38	10	38	19
5	0.77	25.0	0.5	10	50	25
6	0.68	22.1	0.25	5	50	12.5

Tabela 2 Resultados Obtidos com o Rebolo Fino e Aço Dúctil

Rebolo AA 120 M6 V15 e aço ABNT 1020, com h_{eq} = 0,06 μm

Ensaio	R_{af} [μm]	G	Q_w' [mm²/s]	a [μm]	V_w [mm/s]	V_s [m/s]
1	5.07	60.7	1.68	15	112	28
2	7.22	25.7	1.68	45	37.3	28
3	4.75	27.6	1.68	30	56	28
4	5.10	40.7	1.14	30	38	19
5	5.98	25.6	1.5	30	50	25
6	3.87	56.3	0.75	15	50	12.5

A análise da Tabela 1 mostra que pode-se conseguir um bom acabamento superficial, conjugado com a melhor taxa de remoção específica de metal no tempo e com um valor alto para G (ensaio 3). Também pode-se conseguir um bom acabamento superficial conjugado com o valor mais alto para G e com um bom valor para a taxa de remoção específica de metal no tempo (ensaio 5).

Todavia, o melhor acabamento superficial está conjugado a um valor bom para G, mas ao pior valor para a taxa de remoção específica de metal no tempo (ensaio 6).

A análise da Tabela 2 mostra que pode-se conseguir um bom acabamento superficial, conjugado com um valor alto para G, porém com o pior valor para a taxa de remoção específica de metal no tempo (ensaio 6). Também pode-se conseguir o valor mais alto para G, conjugado com o melhor valor para a taxa de remoção específica de metal no tempo, porém com um valor ruim para o acabamento superficial (ensaio 1). Um bom acabamento superficial está conjugado com o melhor valor para a taxa de remoção específica de metal no tempo, porém com um valor muito baixo para G (ensaio 3).

Os valores de rugosidade superficial da peça apresentados nas Tabelas 1 e 2 são ligeiramente elevados por terem sido obtidos por rebolos com estrutura aberta, mais adequados para desbaste. O rebolo com granulometria fino apresentou elevada rugosidade da peça, pela geometria volumosa dos cavacos gerados, que entupiram as porosidade do rebolo, riscando mais a peça.

Como exemplo, pode-se imaginar uma empresa onde a necessidade básica é a de desgastar muito material, num tempo pequeno e com a máxima economia de rebolo. Neste caso, é desejável que se tenha uma elevada taxa de remoção específica de material no tempo e elevado valor para G, sem entretanto, muita exigência quanto ao acabamento superficial: ensaio 3, da Tabela 1 ou ensaio 1 da Tabela 2.

Conclusões

Deste trabalho pode-se concluir que na retificação de aços frágeis com rebolo macio e de granulometria média, a potência de corte média tendeu a crescer e estabilizar-se, pela renovação da superfície de corte do rebolo. Existiu, neste caso, o equilíbrio entre a capacidade de retenção do ligante sobre os grãos abrasivos e a potência de corte média necessária para a remoção do material. Durante os ensaios o rebolo permaneceu agressivo, ou seja, com capacidade de remover material.

A rugosidade superficial da peça foi decrescente em todos os casos e proporcional ao crescimento do número de grãos ativos. Assim, com um número maior de cavacos arrancados e de menor espessura teórica, estes riscam menos a superfície da peça. Portanto a geometria teórica do cavaco, que pode ser controlada pelas condições de usinagem, afeta diretamente o comportamento da rugosidade superficial da peça e os esforços de corte. Neste ensaios, não foi detectado entupimento significativo das porosidades do rebolo.

Nos ensaios de retificação de aços dúcteis com rebolo macio e de granulometria fina, a potência de corte média cresceu até um máximo e em seguida decresceu, tendendo a estabilizar-se. Neste caso, o rebolo perdeu sua agressividade até o momento em que houve a liberação dos grãos abrasivos da superfície de corte do rebolo (elevação da potência de corte média). A partir deste momento, o rebolo permaneceu agressivo, ou seja, a potência de corte média decresceu.

A rugosidade superficial da peça, em todos os ensaios, mostrou-se inicialmente baixa, pela pouca densidade de grãos ativos na região de contato. Porém, foi sempre crescente pelo aumento da densidade dos grãos abrasivos na região de contato e entupimento das porosidades do rebolo. A rugosidade superficial da peça apresentou um crescimento repentino no momento em que iniciou-se a brusca renovação da superfície de corte do rebolo.

Quanto aos parâmetros de entrada, pode-se verificar que a combinação entre estes proporcionou resultados diversos, principalmente com relação a rugosidade final da peça e relação **G**. A decisão sobre a escolha de uma determinada condição de usinagem deve levar em conta o que se pretende deste processo de usinagem. Cada empresa deve fazer a sua escolha específica. Para isto é fundamental que o engenheiro responsável conheça os conceitos básicos sobre a fenomenologia de corte, associada ao processo, e a tendência do comportamento do processo de retificação, para que possa intervir da forma mais adequada.

Agradecimentos

Manifestamos nossos agradecimentos a FAPESP pelo apoio financeiro concedido à realização desta pesquisa e as empresas KOHLBACH, CARBURUNDUM, WEG, EQUITRON e SIVAT pelo apoio na aquisição de ferramentas e equipamentos.

Referências

Bianchi, E. C., 1990, "Ação das Condições de Dressagem na Retificação de Precisão", São Carlos, EESC - USP, Dissertação (Mestrado em Engenharia Mecânica)

Bianchi, E.C., 1992, "Ação da Geometria Teórica do Cavaco no Desgaste de Rebolos de CBN com Ligante Resinóide", São Carlos: EESC - USP, Tese (Doutorado em Engenharia Mecânica).

Bianchi, E.C., Sanchez, L.E.A., Fernandes, O.C., Mogami, O., Silva Júnior, C.E., Aguiar, P.R., 1996, "Análise do Comportamento de Rebolos Convencionais na Retificação de Aços Frágeis", Congresso Norte Nordeste de Engenharia Mecânica, IV. Recife/PE, p. 335-340.

Bianchi, E.C., Sanchez, L.E.A., Fernandes, O.C., Mogami, O., Silva Júnior, C.E., Aguiar, P.R., 1996, "Avaliação do Comportamento de Rebolos Convencionais na Retificação de Aços Dúcteis", Congresso Norte Nordeste de Engenharia Mecânica, IV. Recife/PE, p 387-392.

Hahn, R.S., 1955, "The Effect of Wheel-Work Conformity in Precision Grinding", Transaction of the ASME, Vol. 77, pp.1325.

Kegg, R., 1983, "Industrial Problems in Grinding", Annals of the CIRP, Paris, 32 (2): 559-61.

König, W., 1980, "Fertigungsverfahren Band 2 - Schleifen, Honen, Laepten", VDI Verlag - Duesseldorf.

Malkin, S., 1979, "Negative Rake Cutting to Simulate Chip Formation in Grinding", IN: *Annals of the CIRP.*, Vol. 28.

Peters, J. and Decneut, A., 1975, "L'espaisseur de Coupe Equivalente, Parameter Determinate in Rectification", Mechaniques Materiaux Eletricité, Vol.58, No. 310, pp. 22-30.

Rowe, W.B. and Morgan, M.N., 1993, "The Effect of Deformation on the Contact Area in Grinding", IN: *Annals of the CIRP.*, Vol. 42/1.

Westkämper, E., Tönshoff H.K., 1993, "CBN or CD Grinding of Profiles", in: Annals of the CIRP., Vol. 42/1.

RBCM - J. of the Braz. Soc. Mechanical Sciences
Vol. XIX - No.3 - 1997 - pp. 426-437

ISSN 0100-7386
Printed in Brazil

Using Wavelet Transform to Analyze Tool Vibration Signals in Turning Operations

Roberto Fernandes Tavares Filho
Anselmo Eduardo Diniz
UNICAMP - Universidade Estadual de Campinas
Faculdade de Engenharia Mecânica
Departamento de Engenharia de Fabricação
13083-970 Campinas, SP Brasil
anselmo@fem.unicamp.br

Abstract

The main goal of this paper is to study the feasibility of using multiresolution analysis through the use of wavelet transform, to analyze the tool vibration signal, in order to indirectly establishing the end of turning tool life. To do so, several turning experiments were carried out with different cutting conditions and the tool vibration was measured using accelerometers. After the cuttings, the vibration signals were analyzed in time domain, frequency domain and time-frequency domain and their behaviors were compared with the workpiece surface roughnesses. As the tool wears, the workpiece roughness increases and the tool vibration signal change its features. So, it was necessary to extract from the signal the feature that follows the surface roughness behavior in order to establish the end of tool life based on the workpiece roughness criterion. The analysis was done on the acceleration (signal generated by the sensor), velocity (first integration of the signal) and displacement (second integration) of the tool. The main conclusion of this work is that, the best parameter of the tool vibration signal to follow the surface roughness behavior, is the second level inverse of the wavelet transform of the tool displacement signal.
Keywords: *Wavelet Transform, Turning Tool Vibration, Machining Monitoring.*

Introduction

The goal of signal processing is to analyze, to codify, to transmit and to reconstruct the signal as time goes by. Sometimes, the signal is generated directly from the original source of information, but, most of the times, it is necessary to get data from indirect measurements. Generally, the signal obtained from all the available sensors is a complex mix of many signals, each one related to several physical phenomena occurring simultaneously. So, it is necessary to apply some operations on the signal, to enhance the information coming from the phenomenon that is supposed to be measured.

There are a lot of procedures to process the data, each one suitable for a kind of signal. Basically, there are two major kinds of signals (Cohen, 1986). The random and the deterministic ones. The last ones can be described through mathematical expressions. The random signals, that are more important for the present work, are more difficult to be analyzed, due to the fact they can not be exactly expressed, but just using statistic parameters. A random signal with constant statistic properties is called stationary. A sample this kind of signal can be completely different of another sample, but their statistic features remain the same. An important class of random signals are the ergodic signals. For this kind of signals, the average of the whole set is equal to the average of any representative sampled segment of the signal.

When the random signals are stationary and ergodic, the conventional signal processing techniques can be used. It is more difficult, however, to process non stationary signals, what demands either complex techniques or to assume the ergodicity and so, to assume the risk of possible mistakes. In the case of tool vibration signals analyzed in this work, they have a non stationary random behavior, that can be determined through a windowed Fourier analysis as the tool life elapses. But, most of times, a spectral variation can be noted as time goes by and it is not possible to determine the exact frequency range that is influenced by the tool wear phenomenon. To analyze this kind of signal it is necessary to use techniques that can represent the signal behavior taking into account the frequency variation as time elapses. The study of non stationary signals, where transient events that can not be predicted occur, needs other techniques instead Fourier analysis. Among these techniques are the time-frequency and time-scale Wavelets. The time-frequency wavelets are more suitable for the analysis of quasi-stationary signals and the time-scale wavelets (used in this work) are more suitable to analyze signals with fractal structure (Meyer, 1993).

The wavelet development is recent (Willians and Amaratunga, 1994). Functions similar to wavelets have been known since the beginning of the century, but only recently the scattered available concepts were gathered and engineering applications began to be accomplished. The wavelet transform is a set of

Manuscript received: January 1997. Technical Editor: Leonardo Goldstein Jr.

functions that divide the data, functions or operators in different frequency components and, so, studies each component with a suitable resolution to its scale (Daubechies, 1992). Opposite to the Fourier analysis that can not locate in time the existence of a given frequency signal, the signal decomposition through wavelets allows the analysis of the signal behavior simultaneously, in time and frequency domain.

The windowed Fourier transform also can analyze signals in time-frequency domain. However, the basic difference between it and wavelets is that the high frequency wavelets are narrower than the low frequency ones. So, the wavelet transform is more able to capture signal transients than the windowed Fourier transform, what allows a better time localization of the different signal components. This capacity makes the wavelet transform usable in the non stationary signal analysis. This application is one of the main applications of wavelets (Rioul and Vetterli, 1991). Another advantage of wavelets comparing with the Fast Fourier Transform (FFT) is that the wavelets implementation (at least the Daubechies wavelets that will be applied in this work) demands a smaller number of multiplication for the many transformations.

The result of applying an orthogonal Daubechies D4 wavelet transform on a time series is a set of wavelet coefficients, with the same quantity of the number of elements in the time series. In order to have an easy visualization, together with fast computational implementation, it is proposed here a representation of the so called Wavelet Circles. This is made by a sequence of concentric circles, where each circle is related to a frequency range. The most inner circle represents the lowest frequency range and the range increases in direction to the most external circle which represents the highest frequency range. As the perimeter of each circle increases with the circle diameter, the space left to represent the coefficients also increases. This allows more coefficients to be represented without so many squeezing. Due to the wavelet transform characteristics there are a 2:1 relation of the coefficients quantity from one scale to another, i.e., if in one scale there are 4 coefficients, in the next scale there will be 8, and so on.

In the wavelet circle the coefficient value is squared. In this way, the energy value of that wavelet can be related to the segment length of the corresponding wavelet. The values are normalized having as reference the value of the biggest coefficient, that is represented by a line with length equal to 80% of the distance between the circles. In this representation, the time location is related to the angular displacement, having the time $t = 0$ (zero - beginning of the acquisition) as the rightest point of each circle. Going in the counterclockwise direction, 90 degrees corresponds to ¼ of the whole time, 180 degrees to ½ of the time and so on. The line representing the coefficient is placed in the beginning of the circular section corresponding to its range of time.

This representation does not show the signal average, that has to be shown in a non normalized way, out of the wavelet circle, to make easier the comparison between all the signals.

Practical Applications of Wavelets in Signal Processing

The use of time-scale wavelets is suitable for the kind of signals obtained in turning tool vibration monitoring, because these signals are full of transients. Next, it will be demonstrated with practical examples, the wavelet ability to identify typical situations found in signal analysis, that are not well identified by other methods. The main purpose of this work is to develop a method of feature extraction suitable to real time application in tool wear monitoring. In order to achieve this goal, different orthogonal wavelets (compact support) were tried. Among them, the Daubechies D4 showed to be the best to fulfill this purpose.

At first, a signal composed of two sinusoidal signals of different frequencies can be seen in the left corner of Fig. 1. The Fourier analysis (upper window in the right corner) shows the two frequencies that composes this signal. Looking at this figure, it is not possible to realize that the two harmonics are in different moments of time. The same spectrum would be obtained if the signal were periodic and composed of these two sine curves. The Daubechies D4 wavelet analysis however, shows a different distribution between the upper part of the circle, corresponding to the first part of the signal and the lower part of the circle, corresponding to the second half of the signal. The distribution is represented by the signs on the circles.

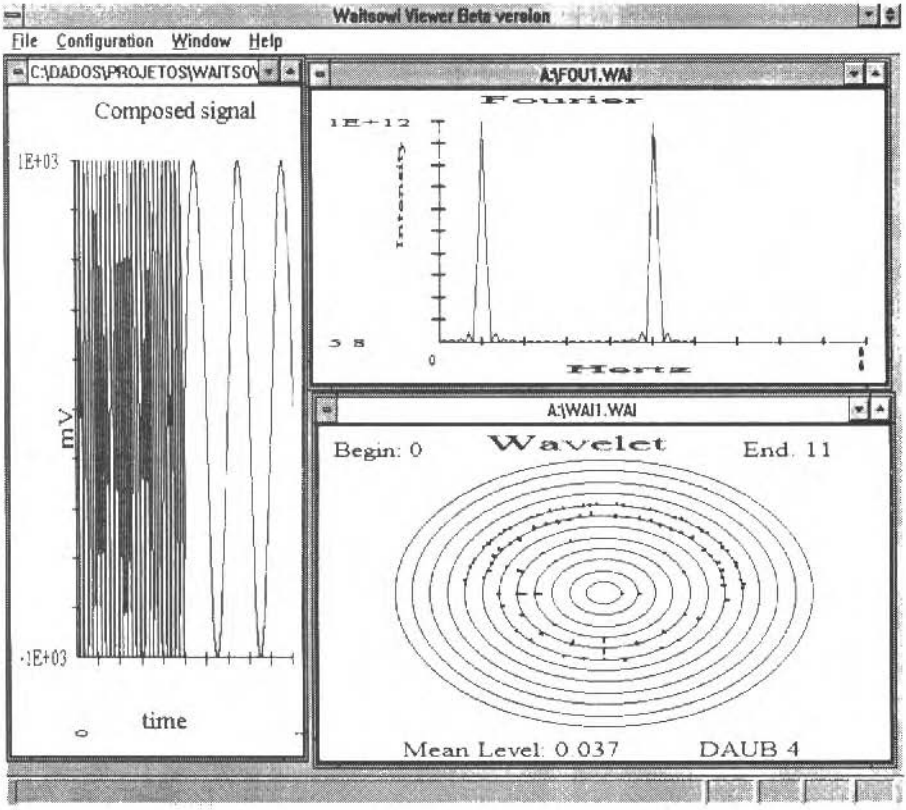

Fig. 1 Comparison between Wavelet and Fourier Analysis

Of course, in this simple example, the windowed Fourier transform would be able to detect the time variation, though with a bigger computational effort. However, if the frequency differences were too big (transient situation), even the windowed Fourier transform would not be able to correctly locate the high frequency components. This happens because the windowing functions have always the same width, regardless its time variation.

A second example of the wavelets capacity can be seen on Fig. 2. In this case a small transient is shown in a sinusoidal signal, in the left part of the figure. The upper right corner of this figure shows that the Fourier transform can not realize this transient, but the wavelet transform, shown in the lower right corner, can. In this analysis, the coefficient related to the time section reached by the transient increases its value, what can be seen by observing the slightly bigger coefficient in the figure.

This last situation leads to another way of analysis using D4 wavelets. Due to the fact that these wavelets are orthogonal and that there is the inverse of the wavelet transform, the coefficients related to the levels 0, 1 and 2 of Fig. 2 can be removed, because they are not important to the extraction of the desired features and the other ones can be inverted. This means that, in order to use this approach, it is necessary to have the signal signature without the disturbing transient, what makes the comparison between both coefficient sets, possible. The resulting signal, that corresponds to the time variation of the wavelet inverses of the levels different of zero (levels one and two), is shown on Fig. 3. The upper window corresponds to the signal without transient and the lower window to the signal with the transient. The difference between them is clear. The transient is clearly seen around the time $t = 2$ s. In this very simple example, the visual inspection of the waveform also give the information about the transient. In more complex situations, however, the transients are usually embedded in combinations that are difficult to be isolated in time domain. In these situations, the time-scale wavelets are more suitable to detect and isolate the small transients of the signal.

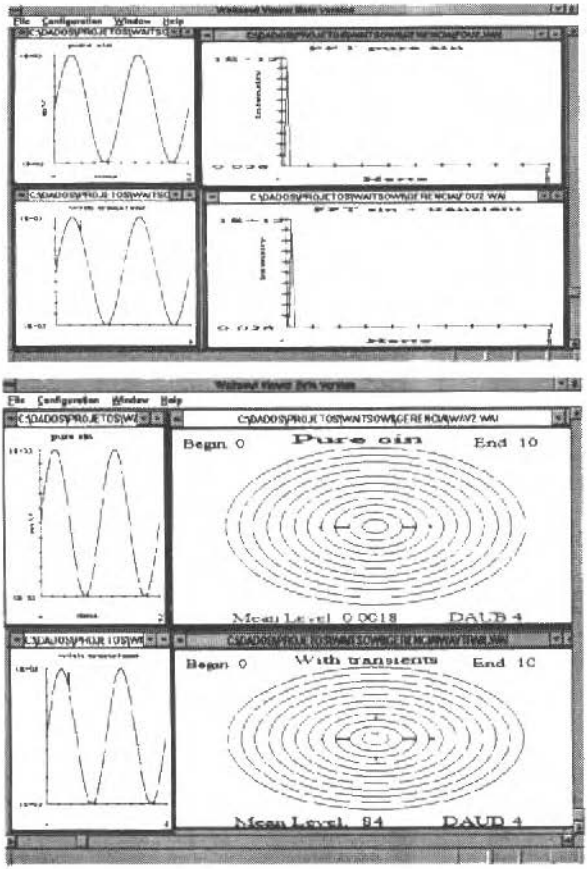

Fig. 2 Another Comparison Between Wavelets and Fourier Transform

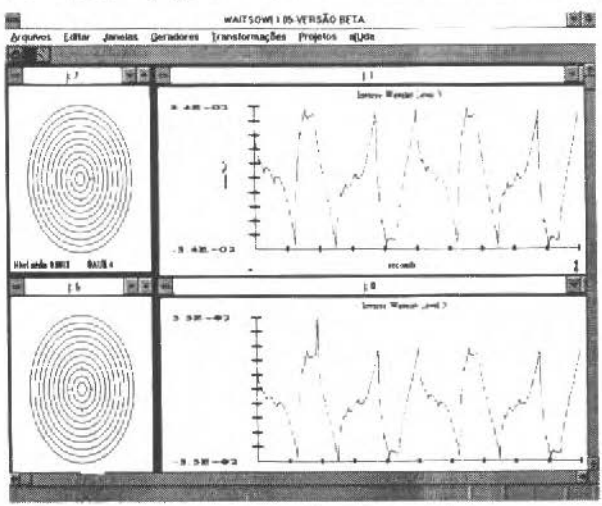

Fig. 3 Inverse of Wavelet Level 3

Monitoring the Machining Process

In a non automated machining process, usually a technician is present and is responsible, among other things, to monitor the tool condition. His (or her) tasks related with tool monitoring can be classified in four groups (Graham, 1989):

- Tool identification
- Establishing the tool reference
- Monitoring tool life
- Detecting tool fracture

When flexible and automatic manufacturing systems are used, the human intervention must be minimal. So, the tasks he (or she) usually accomplishes related to tool monitoring, now must be automated, using sensors and computers that are able to evaluate the tool condition. This work deals just with tool life monitoring through tool vibration signals, that is one of the most used systems in tool monitoring.

Monitoring Tool Life Through Vibration

As the cutting process occurs, the friction between chips and tool and between part and tool produce vibration, that can be monitored and used to detect tool wear and fracture (Bonifácio and Diniz, 1994 a, b).

The transducer is usually a small and cheap piezoelectric one, with frequency band between 100 Hz to 10 KHz. The signal conditioning system is simple and easily available. Due to the relatively low sample rate, the requirements of memory and speed needed for signal processing are suitable to the available PC computers.

One problem to use vibration in tool monitoring is the separation of wear information from the other physical phenomena that also produce vibration. The correlation between the acceleration signal (the vibration sensor measures the instantaneous acceleration of the point it is attached) and tool wear is just clearly visible in aggressive cutting conditions. Besides that, the frequencies generated by the wear are not constant neither for all the machine-tool-part systems nor through the whole tool life. This fact makes the design of a band-pass filter a difficult task, because the important frequency band for tool monitoring is not previously known. This situation is shown on the literature, when one compares the frequency band sensitive to tool wear detected for many authors, as can be seen on Table 1.

Table 1 Tool Vibration Frequency Bands Sensitive to Tool Wear According to Different Authors

Author	Frequency Band
Jiang and Xu (1987)	0 to 117 Hz and 510 Hz
Rao (1986)	1850 Hz and 3200 to 4800 Hz
Akihito and Fujita (1989)	500 to 800 Hz
Sokolowski and Kosmol (1991)	0 to 600 Hz and 5000 to 6000 Hz

Vibrations in a machining process can be classified in two types (Shaw, 1984): forced vibration and self-excited vibration. Forced vibration is induced by cyclic effects far from the resonance frequency. In turning processes, the main sources of this kind of vibration are unbalanced shafts, backlash in bearings and so on.

Self excited vibration happens when more energy is absorbed than released during a simple cycle. The sources of this kind of vibration in machining (Shaw, 1984) are, among others, tool wear, shocks between tool and hard particles in the workpiece, interrupted cutting, variable chip thickness and friction. This work is interested in detecting self excited vibration generated by tool wear. The challenge is to separate the signal generated by this source from other kind of vibrations. As the tool wears, the cutting forces increase, causing a growth on the vibration. Nevertheless, the resulting vibration does not

depend just on wear but also on cutting speed, feedrate, tool geometry, workpiece and tool material and so on.

Thus, tool vibration signal contains a lot of information besides tool wear information. Many techniques have been proposed to extracted the desired features from the signal. The processing can be done either directly on the acceleration signal or on the velocity and displacement signals (Sokolowski and Kosmol, 1991).

Nicolescu et al. (1995) used the Auto Regressive Moving Average (ARMA) technique to analyze tool vibration data. Due to the fact that the ARMA models take into account frequency spectrum change as time goes by, they can be used to compare the theoretical value (given by the model) and the actual value (acquired in a given moment). The difference between the two values is attributed to the tool wear increase. This procedure, however, is difficult to implement due to the complexity of the phenomenon being modeled. An alternative to the modeling of the system is the use of neural networks, combined or not with other techniques of feature extraction, as wavelet or FFT (McLaughlin et al., 1995), (Grabec and Susic, 1995). Still another alternative is the use of fuzzy logic to analyze the signals from different sensors (sensor fusion) (Lie et al., 1992).

A method easy to implement is the comparison of a given signal feature through the tool life with the value obtained with a fresh tool (Bonifácio and Diniz, 1994a). This kind of procedure attenuates the errors due to the sampling or pre-processing of the signal, because these errors tend to be roughly the same in all conditions. The comparison can be carried out in three domain: Time, frequency and time-scale domain.

The techniques on time domain are basically the extraction of the root mean square, that is proportional to the signal energy and the number of peaks above a given threshold. For the monitoring of poor in information signals, like the electrical current of the machine motor, this procedure is reasonable, but a lot of information is lost when the signal is more complex, like in tool vibration monitoring.

Frequency domain techniques usually use Fourier analysis and filters to detect the frequencies where the desired feature is enhanced. This way has been the most used one in this area due to the simplicity and facility to analyze the results. Nevertheless, due to the fact that the signals are non stationary, Fourier analysis can lead to wrong interpretations of the signal behavior, because it hides important local variations. Besides that, signals formed by complex combinations of other signals with frequency superposition, can not be separated by FFT and filters, what makes the information recognition more difficult.

Time-Scale or time-frequency domain techniques have been lately used as an alternative to the shortcomings found in Fourier analysis. These techniques allow the analysis of the signals even when they are non stationary and real time algorithm are already available (Tadao et al., 1994; Kasashima et al., 1994, Newland, 1994). In this work, a combination of scale-time domain (wavelets) and time domain (root mean square - RMS, integration) techniques is used. This combination proved to be efficient in tool wear information extracted from the tool vibration signal.

Experimental Procedures

Several turning experiments were carried out in AISI 4340 steel, using a coated carbide tool (code TNMG 160404-61 GC- 435 from Sandvik Coromant). Nine experiments were performed with cutting speed of 200, 250 and 300 m/min and feed rates of 0.13, 0.15 and 0.20 mm/rev. Besides these, 2 other experiments were carried out with $f = 0.15$ mm/rev and $v_c = 225$ and 275 m/min and depth of cut $a_p = 1$ mm. All these conditions are typical of finish turning operations. One experiment finished when the tool was so worn that the surface roughness (Ra - average roughness) of the workpiece exceeded 5 μm. The tool life was considered finished when Ra reached 3 μm. Therefore, the experiments always went further than the end of tool life. The experimental setup is shown on Fig. 4. The machine used was a CNC lathe with a main motor with 30 HP.

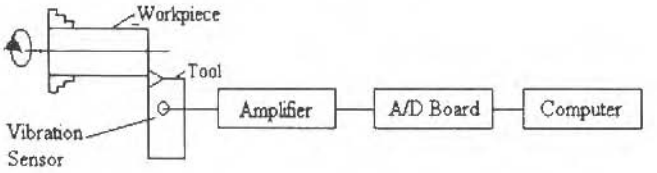

Fig. 4 Experimental Setup

The sensor measured the tool vibration in cutting direction. It is designed to measure signals up to 10 KHz and have its resonance frequency in 50 KHz. A low-pass filter with 10 KHz of cutting frequency was plugged in the amplifier. The sampling rate of the A/D board was 33 KHz.

After the experiments the surface roughness of all machined parts were measured. The roughness parameters measured were Ra and Rmax.

The signal obtained in the sensor was analyzed using some different techniques. At first, the following parameters of the acceleration signal were analyzed: Root mean square, spectral variation using fast Fourier transform, Daubecchies D4 wavelets and root mean square of some chosen levels of wavelets. Secondly, the acceleration signal was integrated and the same parameters were used to analyze the resulting velocity signal. Thirdly, a second integration was done and the same parameters of the displacement signal were analyzed. All these parameters were studied as the cutting time (or cutting length) elapsed and workpiece surface roughness was compared with the cutting length, since, in finish turning, the roughness of the part is the main criterion to establish the end of tool life and it increases as the tool wear increases.

The wavelet analysis of acceleration, velocity and displacement signals were done through the following steps:

- calculation of Daubecchies D4 wavelets;
- filtering out the wavelet coefficients that does not relate with tool wear;
- obtention of the inverse curve of the RMS of the other coefficients

Results and Discussions

All the analysis done with the acceleration and velocity signals did not show a good correlation between the parameters and the surface roughness, except when the cutting conditions were too heavy. Therefore, only the results involving the tool displacement signal will be discussed. These results should be expected, because one of the causes of the roughness left on the workpiece is the relative movement between tool and workpiece. The tool displacement, not the acceleration or velocity, is the best representation of this movement.

The typical surface roughness behavior with cutting length (see Fig. 5) is a small decrease when cutting length is short, a period when it remains almost constant, with some tendency to increase, followed by a sudden growth. When this happens, the tool is totally worn, in coated tools the coating is already consumed and the tool is performing the cut with its substrate.

The thinner line in all figures from now on, except in Fig. 6, represents the actual value of the parameter and the thicker one represents a sixth order polynomial curve made to approach the actual one. Sometimes the correlation between the polynomial regression and the actual values is not so good, but the purpose of the polynomial regression is just to show the trend of the parameter being measured.

The behavior of RMS of tool displacement did not show a good correlation with surface roughness behavior, except in some experiments. Figure 5 shows the curve of tool displacement against cutting length for the experiment that presented the best correlation with surface roughness (experiment with v_c = 200 m/min and f = 0.20 mm/rev). It can be seen on this figure a similar behavior to surface roughness behavior described previously. But even in this experiment, the tool displacement began to increase strongly later than surface roughness. (Lc = 4900 m for tool displacement and Lc = 4300 m for surface

roughness). So, this parameter is not good to establish the end of tool life having the roughness of the part as the criterion.

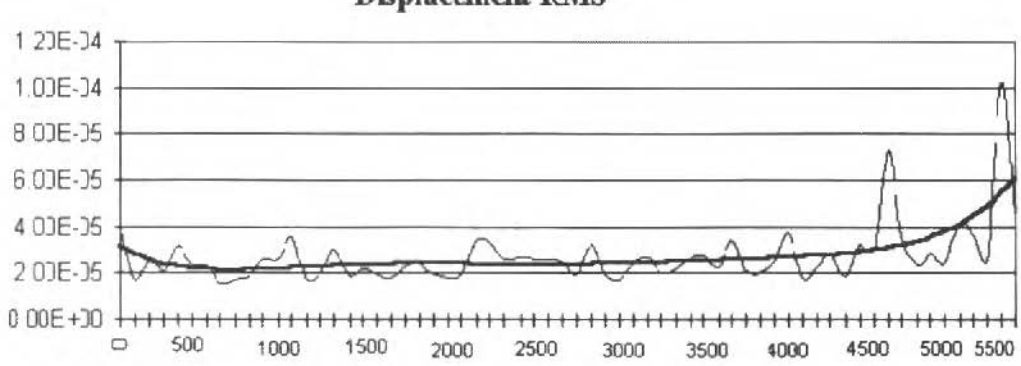

a)

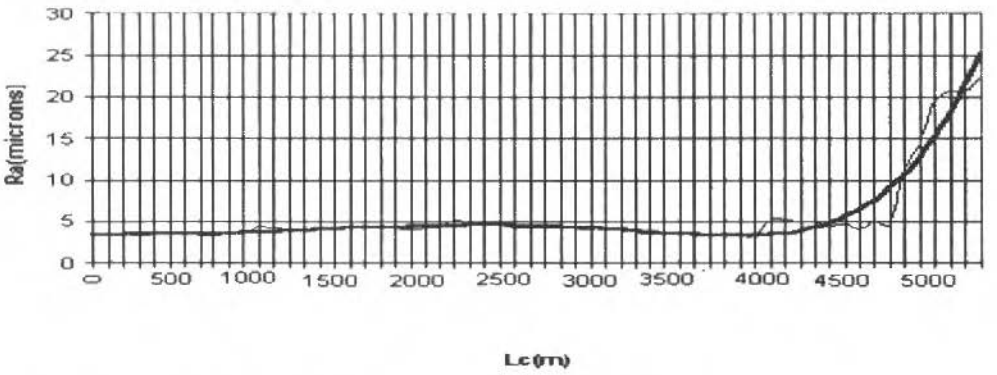

b)

Fig. 5 RMS of tool displacement - v_c = 200 m/min f = 0.20 mm/rev

The next attempt to find a correlation between tool displacement and workpiece roughness was through the spectral analysis. It can be seen on Fig. 6 that the frequency spectrum can not be correlated with surface roughness. It is clear that the energy is concentrated in the lower frequencies. However, it could not be seen any change of the signal amplitude through the whole experiment, in any frequency range, that could be correlated with surface roughness behavior. So, it is not through filtering the signal in any frequency band that will be possible to find a parameter that could be used to establish the end of tool life.

After trying all the conventional signal analysis, an extensive search for a solution started. It consisted in the decomposition of the tool displacement signals in wavelets of several forms, trying to find the best kind of wavelets for the purpose of this work. It was found that the Daubechies D4 wavelets were the best one. The RMS curves of the inverse of the third level of the D4 wavelets against cutting length presented a good correlation with surface roughness.

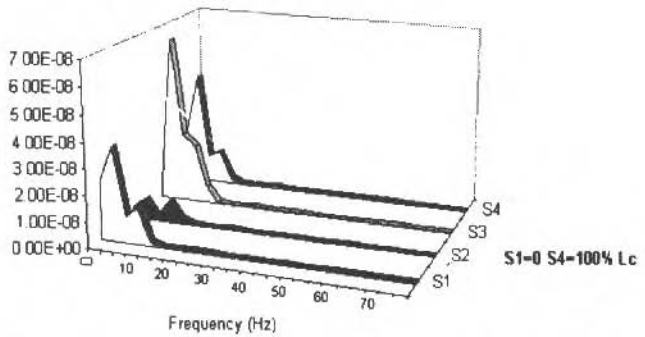

Fig. 6 Frequency Spectrum of tool displacement - v_c = 200 m/min and f = 0.13 mm/ver

Figures 7 and 8 show two examples of this good correlation. A visual analysis of these figures proves this good correlation, at least when the polynomial regressions of the RMS of wavelet inverse curve and roughness curve are compared. This means that the trends of the curves are similar. The curves of RMS X Lc presented a greater dispersion around the polynomial curves than the Ra X Lc curves, because the sampling of the tool displacement signal had much more points (10 samplings of 4096 points were sampled in each workpiece) than the roughness. Each point in the graphic

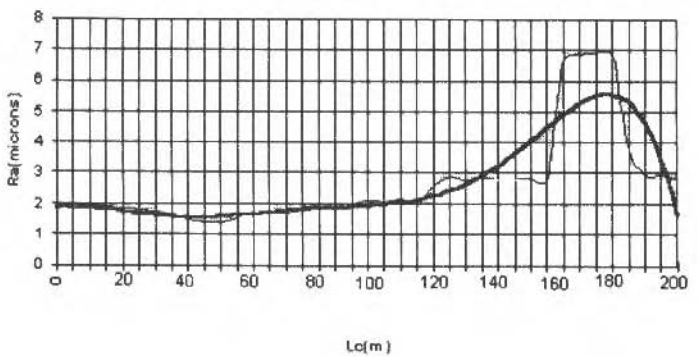

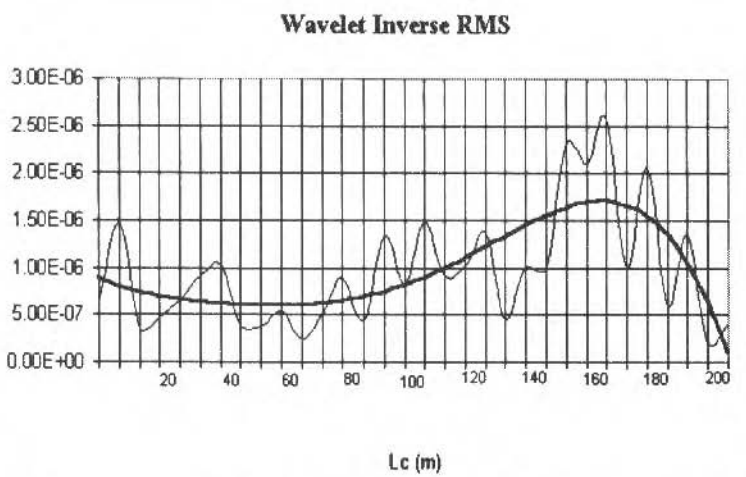

Fig. 7 Workpiece Roughness (Ra) and RMS wavelet inverse - v_c = 225 m/min and f = 0.15 mm/rev

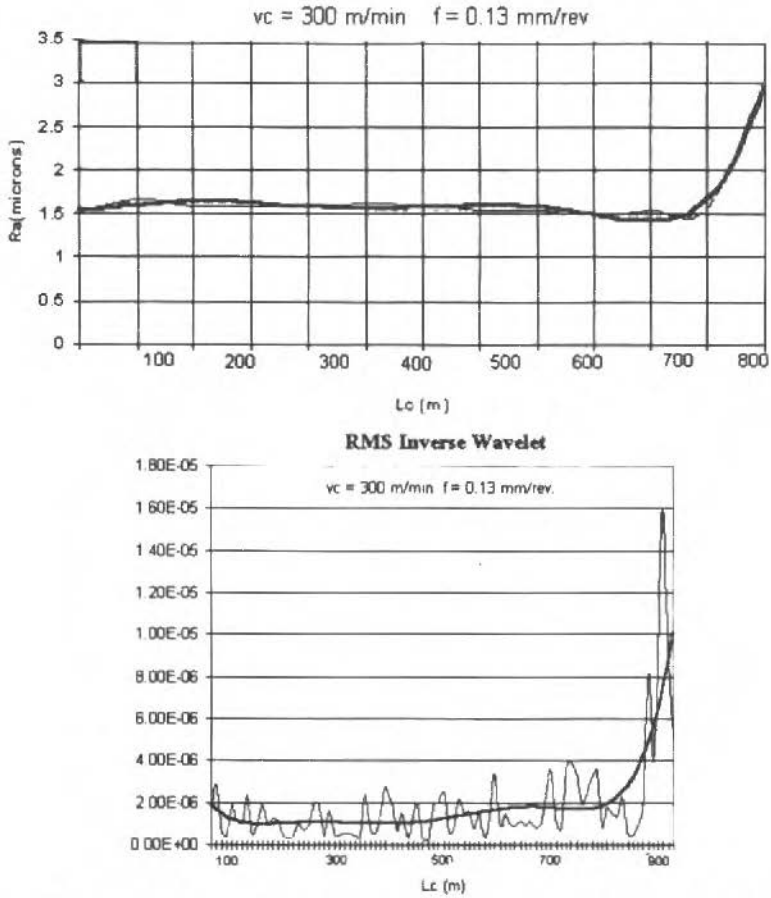

Fig. 8 Workpiece Roughness (Ra) and RMS wavelet inverse - v_c = 300 m/min and f = 0.13 mm/rev

corresponds to an average of three points measured in each workpiece, with 120^0 of difference between each measurement in the same feed position. Also, there are small differences between the inflection points of the RMS X Lc and Ra X Lc curves. This happens because, for each workpiece, there are 10 values of Lc for the RMS (tool displacement) curves and just one value of Lc for the Ra curves.

One thing that is worthy to be cited when Figs. 7 and 8 are compared is the different behavior of surface roughness. In Figure 7, it drops after reaching a maximum value, close to the end of tool life, while in Fig. 8, it only increases without dropping. The explanation for this fact may be related to the shape of the tool nose. In the experiment showed in Fig. 7, the tool may have chipped and found a better shape, similar to the initial shape, after having been worn heavily, what caused the increase of surface roughness. In Figure 8, the tool may have worn, without chipping and, therefore, the surface roughness just increased. The tool chipping is unpredictable when it is very worn and, consequently, the behavior of surface roughness. The wavelet inverse was able to follow the consequences in the process of the changing tool shape.

As the similarity between the behavior of RMS wavelet inverse and workpiece surface roughness was found, the next step was to find a way to establish the end of tool life using this parameter. It was previously established that the end of tool life would occur when the surface roughness value reached Ra = 3 μm. Sometimes, the surface roughness increased suddenly, passing from a value lower than 3 μm in a workpiece to a value very large, bigger than the equipment could measure, in the next machined

workpiece. It was found that the division between the value of Ra immediately before it reached 3 μm and the initial value was close to 1.5 (150% of the initial value).

Therefore, this value (1.5) was used to establish the end of tool life using the RMS wavelet inverse. The value of the initial RMS obtained in the polynomial regression was multiplied by 1.5 and, with this new value of RMS, still in the polynomial regression curve, the cutting length corresponding to the end of tool life was obtained.

Table 2 shows the values of tool life using the two criteria, Ra = 3 μm and RMS = 1.5 x initial RMS of wavelet inverse. It can be seen on this table, that the tool lives are very close using these two criteria. The difference between these two criteria is always smaller than the cutting length of one workpiece. It could not be reached better result than this one, once the cutting length of the roughness measurement is related to a point in the middle of the workpiece, while the tool vibration signals were sampled in ten moments during the workpiece cut. Therefore, it was found that the parameter RMS of the third level of the inverse of the Daubechies D4 wavelet extracted from the tool displacement signal is the best parameter to establish the end of tool life in finish turning operations, where the tool is replaced based on the workpiece surface roughness.

Table 2 End of Tool Lives for Both Criteria

Cutting Conditions v_c (m/min) f (mm/rev)	Tool Life (Criterion Ra = 3 μm) (m)	Tool Life (Criterion RMS = 1.5 x initial RMS) (m)
200 - 0.13	6500	6480
200 - 0.15	6100	5800
225 - 0.15	1440	1300
275 - 0.15	1240	1260
300 - 0.13	827	840
300 - 0.15	883	890

Final Remarks

Through the analysis of the results shown in this work, it could be realized that the tool displacement, obtained through double integration of the acceleration signal, allows the identification of a signal behavior that can be related to the machined workpiece roughness behavior. The use of wavelets together with conventional statistic techniques to determine "signatures" embedded in signals composed of many components with complex forms, proved to be an efficient tool to extract features from the signal. They are more suitable for this purpose than the conventional ways of analysis in either, frequency domain or time domain.

The reason why the tool displacement is a better alternative to extract the signal related to the roughness variation is that the acceleration signal has components of high amplitudes and frequencies, caused by other phenomena besides the tool wear, that cause the surface roughness increase. The double integration of these signals remove these components and allows the enhancement of the component due to the tool wear. Besides that, the integration narrowed the frequency band where the signal showed up, what allowed an optimization of the localization in frequency domain of the wavelet transform.

The use of wavelet transform instead of fast Fourier transform allowed the recovering of complex non stationary signals, what would not occur with the decomposition of the signal in sines and cosines, as in the Fourier analysis. It might be possible that another wavelet basis could better represent the signal due to the tool wear, what would improve the results obtained with the Daubechies D4 wavelet. To look for this other wavelet basis is out of the purpose of this work and will be the subject of a future work.

It can be concluded that a reliable procedure aiming to automatically establish the end of tool life in finish turning operations, can be described as follows:

- monitor the acceleration signal of the tool;
- extract the mean value and integrate twice the signal;
- calculate the Daubechies D4 wavelet coefficients;

- extract the wavelet third level;
- inverte this level of wavelet;
- calculate the root mean square value;
- calculate the sixth order polynomial regression;
- multiply the initial value (using the polynomial regression) by 1.5 (named limit value for tool life), and
- compare all the RMS values obtained in the polynomial regression with the value obtained in the previous step. When this value is bigger than the limit value for tool life, replace the tool.

This set of procedures can be implemented in real time.

References

Akihito, N. and Fujita, S., 1989, "Development of a Cutting Tool Failure Detector", Bulletin of the Japan Society of Precision Engineering, Vol. 32, pp. 134-139.

Bonifácio, M. E. R. and Diniz, A. E., 1994a, "Correlating Tool Wear, Tool Life, Surface Roughness and Tool Vibration in Finish Turning with Coated Carbide Tools", Wear, Vol. 173, pp. 137-144.

Bonifácio, M. E. R. and Diniz, A. E., 1994b, "Monitoring the Tool Life in Finish Turning Using Vibration Signals", Journal of the Brazilian Society of Mechanical Sciences", Vol. 16, pp. 56-71.

Cohen, A., 1986, "Biomedical Signal Processing", CRC Press, Florida, USA.

Daubechies, I., 1992, "Ten Lectures on Wavelets", SIAM, Philadelphia, USA.

Grabec, I. and Susic, E., 1995, "Application of a Neural Network to the Estimation of Surface Roughness from AE Signals Generated by Friction Process", International Journal of Machine Tools and Manufacture, Vol. 35(8), pp. 1077-1086.

Graham, T. S., 1989, "Monitoring the Unmanned Machining", FMS Magazine, Vol. 3(7), pp. 127-131

Jiang, Y. C. and Xu, J. H., 1987, "In Process Monitoring of Tool Wear Stage by the Frequency Band Energy Method", Annals of the CIRP, Vol. 36, pp. 45-48.

Kasashima, N., Mori, K. and Ruiz, G. H., 1994, "Diagnosing Cutting Tool Conditions in Milling Using Wavelet Transform", Bulletin of the Japan Society for Precision Engineering.

Lie, S., Elbestawi, M. A. and Du, R. X., 1992, "Tool Condition Monitoring in Turning Using fuzzy Set Theory", International Journal of Machine Tools and Manufacture, vol. 32(6), pp. 781-796.

Mc Laughlin, C., Tansel, I. N. and Mekdeci, C., 1995, "Detection of Tool Failure in End Milling with Wavelet Transformations and Neural Networks", International Journal of Machine Tools and Manufacture, Vol. 35(8), pp. 1137-1147

Meyer, Y., 1993, "Wavelets, Algorithms and Applications", SIAM, Philadelphia, USA.

Newland, D. E., 1993, "An Introduction to Random Vibrations, Spectral and Wavelet Analysis", Longman Scientific & Technical, England.

Nicolescu, M., Carlsson, T. and Bejhem, M., 1995, "The Use of Vibration Signal in cutting Process Monitoring", Proceedings of the 1st International Machining and Grinding Conference, Ann Arbor, Michigan.

Rao, S. B., 1986, "Tool Wear Monitoring Through the Dynamics of Stable Turning", ASME Journal of Engineering for Industry", Vol. 108, pp. 184-196.

Rioul, O. and Vetterli, M., 1991, "Wavelets and Signal Processing", IEEE Signal Processing Magazine, Vol. 91(10), pp. 14-38

Shaw, M. C., 1984, "Metal Cutting Principles", Clarendon Press, Oxford

Sokolowski, A. and Kosmol, J., 1991, "Utilization of Vibration Measurements of Machine Tool Elements in the Monitoring of the Cutting Tool Conditions", Proceedings of the 4th World Meeting on Acoustic Emission and 1st International Conference on AE in Manufacturing, pp. 327-333.

Tadao, K., Hiroshi, O. Akinori, N. and Eiji, K., 1994, "Application of Wavelet Analysis to Monitoring of Cutting Conditions in Milling", Bulletin of the Japan Society of Precision Engineering, pp. 345-350

Williams, J. and Amaratunga, K., 1994, "Introduction to Wavelets in Engineering", International Journal for Numerical Methods for Engineering, Vol. 37(6), pp. 2365-2388.

RBCM - J. of the Braz. Soc. Mechanical Sciences
Vol. XIX - No.3 - 1997

ISSN 0100-7386
Printed in Brazil

Abstracts

Moura, L. F. M., and Belo, F. B., 1997, "Two-Phase Flow Imaging by Electrical Capacitance Tomography: Numerical Simulation for Image Reconstruction Algorithm Development", RBCM - J. of the Braz. Soc. Mechanical Sciences, Vol. 19, No. 3, pp. 322-331.

This paper describes a capacitance system for tomographic imaging of two-phase flows. Numerical simulations based on the finite element method provided the capacitance values between the electrode pairs for different spatial flow distribution. A linear back projection algorithm was used to reconstruct the cross section image of the two-phase flow from the capacitance values. Some reconstructed flow images (stratified, annular and droplets) obtained using this algorithm are presented and discussed. Further efforts are undertaken to improve the filtering technique applied to the back projection algorithm. Limitations and possible future improvements of this technique are discussed.

Keywords: Two-Phase Flow, Tomography, Image Reconstruction Algorithm, Numerical Simulation

Soviero, P. A. O., and Lavagna, L. G. M., 1997, "A Numerical Model for Thin Airfoils in Unsteady Motion", RBCM - J. of the Braz. Soc. Mechanical Sciences, Vol. 19, No. 3, pp. 332-340.

A numerical model based on normal dipole panels with constant strength distributions is proposed in order to solve the linearized unsteady motion of the thin airfoil in incompressible inviscid flow. The direct relationship between vortices and normal dipole panels with constant strength distributions is employed, with the specific aim of simplifying the numerical implementation of circulation conservation, force calculation and vortex shedding. The suggested method is fast and general. Classical unsteady thin airfoil problems are solved by the present model and the results are shown to compare well with analytical results.

Keywords: Thin Airfoils, Unsteady Flow, Normal Dipole Panels.

Fonseca, G. F., Bodstein, G. C. R., and Hirata, M. H., 1997, "A Numerical Inviscid Vortex Model Applied to Parallel Blade-Vortex Interaction", RBCM - J. of the Braz. Soc. Mechanical Sciences, Vol. 19, No. 3, pp. 341-356.

In this paper a numerical inviscid vortex method is applied to the unsteady, two-dimensional and incompressible flow that occurs during a parallel blade-vortex interaction. We use a vorticity-panel method, where the airfoil bound vorticity is modeled as a discrete distribution of vortices having strength continuously and linearly distributed over the airfoil surface. The impermeability condition is satisfied on the airfoil surface, whereas the no-slip condition is not. The generation of the wake vorticity is accomplished with the equation of conservation of circulation and the application of the Kutta condition, which imposes the continuity of the pressure field at the airfoil trailing edge. The vortices shed into the flow to form the airfoil wake are convected downstream with the mean flow using a Lagrangian time-marching scheme. The main vortex that interacts with the airfoil is modeled as a potential vortex. The numerical results are compared to the experimental data of Straus et al. (1990), showing good agreement for the entire flow, except when the vortex is close enough to the trailing edge so that separation occurs.

Keywords: Aerodynamics, Airfoil, Blade-Vortex Interaction, Vortex Methods, Wakes.

Bortoli, A. L., 1997, "Convergence Acceleration Applied to Compressible and Incompressible Fluid Flow Calculations", RBCM - J. of the Braz. Soc. Mechanical Sciences, Vol. 19, No. 3, pp. 357-370.

Today, numerical flow simulation plays more and more important role in the design process of an aerodynamic body. To design a new mechanical device involving fluid dynamics, a numerical simulation is well accepted and justified. However, much work still remains to improve the numerical methods towards a fast, accurate and stable convergence. Techniques to accelerate the convergence, namely the local time-stepping, residual averaging and multigrid techniques are normally employed. This work employs acceleration techniques to solve compressible and incompressible fluid flows using a finite volume, explicit Runge-Kutta multistage scheme with central spatial discretization in combination with multigrid and preconditioning. Numerical results are presented for a three dimensional channel and the NACA 00012 airfoil for Mach-numbers ranging from 0.8 to 0.005 using the Euler equations.

Keywords: Numerical Simulation, Aerodynamics, Finite Volume, Multigrid, Compressible and Incompressible Flows, Runge-Kutta Method.

Figueiredo , J. R., 1997, "A Unified Finite-Volume Finite-Differencing Exponential-Type Scheme for Convective-Diffusive Fluid Transport Equations", RBCM - J. of the Braz. Soc. Mechanical Sciences, Vol. 19, No. 3, pp. 371-391.

This paper presents a new discretization scheme for the convective-diffusive transport equation of heat, mass or momentum in fluid media, constructed within the control-volume approach for both regular or irregularly spaced rectangular meshes. The present scheme shares with others, such as LOADS and Flux-Spline, the kind of exponential interpolating curve, obtained as the exact solution of an approximated equation that admits a so called source term. To compute this term the present scheme incorporates Allen's finite difference approach into the finite volume method. The resulting procedure was called Unified Finite Approach Exponential-Based Scheme, UNIFAES. It is a conservative form scheme much simpler than both LOADS and Flux-Spline. The scheme is submitted to a series of tests in the linear problem of convection and diffusion of a scalar in a parallel flow, where it is compared to the central differencing, to the exponential scheme and to LOADS, showing excellent accuracy for all function types and unconditional stability for all Peclet numbers.

Keywords: Convective-Diffusive Transport, CFD, UNIFAES, Finite Difference, Finite Volume.

Spim Junior, J. A., and Garcia, A., 1997, "An Optimization of the Finite Difference Method for Modeling Solidification of Complex Shaped Domains", RBCM - J. of the Braz. Soc. Mechanical Sciences, Vol. 19, No. 3, pp. 392-409.

The finite-difference method is widely used in the formulation of a mathematical representation of the solidification process in metal/mold systems. When complex geometries have to be analyzed, generally Finite-Elements Methods are preferred. The present work proposes a modification in the distribution of elements from the mesh, by using an analogy between electrical and thermal circuits, which permits greater versatility in discretizing regions of complex shape. The governing equation of electrical circuits theory is used by applying an explicit version of the Finite-Difference Method.

Keywords: Mathematical Modeling, Solidification, Simulation, Two-phase Systems.

Bianchi, E. C., Fernandes, O. C., Silva Júnior, C. E., Valarelli, I. D. and Aguiar, P. R., 1997, "Behavior Analysis of Conventional Grinding Wheel in Brittle and Ductile Steels Machining", RBCM - J. of the Braz. Soc. Mechanical Sciences, Vol. 19, No. 3, pp. 410-425 (In Portuguese).

The aim of this work is to study the behavior of the plan tangential grinding process with conventional grinding wheels, under several machining conditions and a selected dressing condition. The analysis of the grinding performance was done regarding the cutting surface wear behavior of the grinding wheel for brittle and ductile steels workpieces. The grinding input parameters, which were, cutting speed, workpiece speed and cutting feed, were chosen based on the grinding machine characteristics. The results discussion emphasized the wear mechanism of the grinding wheel cutting surface and the cutting phenomenology of the grinding process.

Keywords: Machining Conditions, Conventional Grinding Wheels, Grinding Wheel Wear.

Tavares Filho, R. F., and Diniz, A. E., 1997, "Using Wavelet Transform to Analyze Tool Vibration Signals in Turning Operations", RBCM - J. of the Braz. Soc. Mechanical Sciences, Vol. 19, No. 3, pp. 426-437.

The main goal of this paper is to study the feasibility of using multiresolution analysis through the use of wavelet transform, to analyze the tool vibration signal, in order to indirectly establishing the end of turning tool life. To do so, several turning experiments were carried out with different cutting conditions and the tool vibration was measured using accelerometers. After the cuttings, the vibration signals were analyzed in time domain, frequency domain and time-frequency domain and their behaviors were compared with the workpiece surface roughnesses. As the tool wears, the workpiece roughness increases and the tool vibration signal change its features. So, it was necessary to extract from the signal the feature that follows the surface roughness behavior in order to establish the end of tool life based on the workpiece roughness criterion. The analysis was done on the acceleration (signal generated by the sensor), velocity (first integration of the signal) and displacement (second integration) of the tool. The main conclusion of this work is that, the best parameter of the tool vibration signal to follow the surface roughness behavior, is the second level inverse of the wavelet transform of the tool displacement signal.

Keywords: Wavelet Transform, Turning Tool Vibration, Machining Monitoring.

Sixth Pan American Congress of Applied Mechanics
PACAM VI

to be held jointly with

8th International Conference on Dynamic Problems in Mechanics
DINAME 99
in
Rio de Janeiro
Brazil
4 - 8 January, 1999

PACAM I was held in 1989 in Rio de Janeiro. After ten years of successful meetings (Rio de Janeiro - BRAZIL, 1989; Valparaiso - CHILE, 1991; São Paulo - BRAZIL, 1993; Buenos Aires - ARGENTINA, 1995; San Juan - PUERTO RICO, 1997), we are pleased to announce that PACAM will return to Rio de Janeiro.

PACAM aims to bring together researchers, practicing engineers and students from South, Central, and North America. However, participants from all other continents have taken part in previous meetings and are welcome to PACAM VI. An unusual opportunity is provided for personal interaction between workers from different geographical areas and from different branches of mechanics.

Papers on all the usual, as well as unusual, topics of mechanics are welcome. We wish to highlight the social development: "Women in Mechanics" and the technical development: "Biomechanics".

Sponsors:

The American Academy of Mechanics
The Brazilian Academy of Engineering
The Brazilian Society of Mechanical Sciences

Technical Sessions:

Pontificia Universidade Católica
Rua Marques de São Vicente 225 Gávea
Rio de Janeiro, RJ Brasil

Accommodations:

Copacabana Beach or Ipanema Beach

Deadlines:

April 1, 1998 - Submission of 4-page abstract for the Congress.
April 1, 1998 - Application for travel grant for participants from the U.S. (Funding pending)
August 1, 1998 - Notification of acceptance of paper.

More information: pacam99@civ.puc.rio.br

RBCM - J. of the Braz. Soc. Mechanical Sciences
Vol. XIX - No 3 - 1997 - pp. 441-444

ISSN 0100-7386
Printed in Brazil

FORMULÁRIO DE AFILIAÇÃO

ASSOCIAÇÃO BRASILEIRA DE CIÊNCIAS MECÂNICAS
Av. Rio Branco, 124 - 18° andar - 20040-001 Rio de Janeiro - RJ
Tel.: (021) 221-0438 - Fax: (021) 222-7128
e-mail: abcmalfs@ omega.lncc.br
CGC 83.431 593/0001-78

INDIVIDUAL

Por favor, preencha os dois lados do formulário.

Nome _____

Endereço Residencial _____

CEP _____ Cidade _____ Estado _____

Pais _____ Tel.: ( )_____ Fax: ( ) _____

E-mail _____

Empresa _____

Dept./Divisão _____ Posição _____

Endereço Comercial _____

CEP _____ Cidade _____ Estado _____

Pais _____ Tel.: ( )_____ Fax: ( ) _____

E-mail _____

Candidato-me a: ☐ Admissão ☐ Mudança de Categoria

Na categoria de: ☐ Sócio efetivo ☐ Sócio Aspirante

Solicito enviar correspondência para o seguinte endereço:

☐ Comercial ☐ Residencial

Data _____ Assinatura _____

Para uso da ABCM

Aprovado _____ Data _____ Sócio n° _____

FORMAÇÃO E EXPERIÊNCIA PROFISSIONAL

Por favor, liste em ordem cronológica os dados completos de sua formação e experiência profissional. A falta desses dados impedirá o processo de admissão. Obrigado.

FORMAÇÃO ACADÊMICA

Graduação - Área _____ Anos _____ a _____
Instituição _____ País _____

Mestrado - Área _____ Anos _____ a _____
Instituição _____ País _____

Doutorado - Área _____ Anos _____ a _____
Instituição _____ País _____

Outro - Área _____ Anos _____ a _____
Instituição _____ País _____

EXPERIÊNCIA PROFISSIONAL

Empresa _____ Anos _____ a _____
Natureza da atividade _____ Posição _____

Empresa _____ Anos _____ a _____
Natureza da atividade _____ Posição _____

Empresa _____ Anos _____ a _____
Natureza da atividade _____ Posição _____

Indique até um máximo de 8 áreas de acordo com os códigos numéricos do Anexo.

Áreas de Especialização _____

Aplicação _____

Comentários _____

Área de Especialização

Especifique no Formulário de Afiliação os códigos numéricos das suas Áreas de Especialização e de Aplicação (verso).

1000 Fundamentos e Métodos Básicos em Mecânica Teórica e Aplicada
1010 Mecânica do Contínuo
1110 Método dos Elementos Finitos
1120 Método dos Elementos de Contorno
1130 Métodos Assintóticos
1140 Método das Diferenças Finitas
1150 Outro Métodos em Mec. Computacional
1210 Métodos Estocásticos e Estatísticos
1310 Modelagem
1410 Fundamentos de Análise Experimental
1510 Metrologia
1610 Gerência de Projetos
2000 Dinâmica e Vibrações
2110 Cinemática e Dinâmica
2210 Vibrações de Sólidos - Fundamentos
2310 Vibrações - Elementos de Estruturas
2320 Vibrações - Estruturas
2330 Propagação de Ondas em Sólidos
2340 Impacto em Sólidos
2350 Identificação de Parâmetros
2420 Propagação de Ondas em Fluidos
2510 Interação Fluido-Estrutura
2610 Astronáutica - Mec. Celeste e Orbital
2710 Explosão e Balística
2810 Acústica
3000 Controle e Otimização
3110 Projeto e Teoria de Sistemas Mecânicos
3210 Sistemas de Controle Ótimo
3220 Sistemas de Controle Adaptativo
3230 Aplicações em Sistemas e Controle
3310 Robótica
3410 Otimização de Sistemas e Processos
4000 Materiais
4110 Biomateriais
4120 Materiais Metálicos
4130 Materiais Cerâmicos
4140 Materiais Poliméricos
4150 Materiais Conjugados
4210 Conformação Mecânica
4300 Caracterização e Controle Microestrutural
4410 Comp. Mecânico dos Materiais
4420 Comp. Mec. Mat. - Baixas Temperaturas
4430 Comp. Mec. Mat. - Altas Temperaturas
4440 Comp. Mec. Mat. - Carregamto. Variável
4450 Comp. Mec. Mat. - Carregamto. Dinâm.
4500 Mecanismos de Fratura
4600 Mecânica da Fratura
4710 Ensaios Destrutivos
4720 Ensaios Não-Destrutivos
4800 Corrosão
5000 Mecânica dos Sólidos
5010 Elasticidade Linear
5020 Elasticidade Não-Linear
5030 Viscoelasticidade
5040 Plasticidade
5050 Visco-Plasticidade
5060 Mecânica dos Materiais Conjugados
5070 Mecânica dos Meios Porosos
5110 Reologia
5210 Cabos, Hastes e Vigas
5220 Membranas, Placas e Cascas
5230 Estruturas - Geral
5240 Estruturas - Contato com o Solo
5250 Estruturas - Submersas/Semi-submersas
5260 Estruturas - Móveis
5270 Estruturas - Vasos e Contenção
5310 Mecânica dos Solos - Básico
5320 Mecânica dos Solos - Aplicações
5330 Mecânica das Rochas
5410 Efeitos Eletro-Magnéticos em M. Sólidos
5420 Efeitos Térmicos em M. dos Sólidos
5510 Estabilidade de Estruturas
5520 Comportamento após a Flambagem
5530 Estados Limites e Cargas de Colapso
5540 Acomodação e Acúmulo de Dano
5610 Mecânica de Fratura
5650 Tribologia
5655 Atrito e Desgaste
5710 Componentes de Máquinas
5720 Acoplamentos e Juntas Não-Soldadas
5800 Análise Experimental de Tensões
6000 Mecânica dos Fluidos
6010 Reologia
6110 Hidráulica
6210 Escoamento Incompressível
6220 Escoamento Compressível
6230 Escoamento Rarefeito
6240 Escoamento em Meios Porosos
6250 Magneto-Hidrodinâmica e Plasma
6270 Escoamento Multifásico
6310 Camada Limite - Contorno Sólido
6320 Camada Limite - Contorno Livre
6410 Escoamento Interno - Dutos, Canais, etc.
6430 Escoamento com Superfície Livre
6510 Estabilidade de Escoamento
6520 Turbulência
6530 Hidrodinâmica - Veículo de Estrut. Naval
6540 Aerodinâmica
6610 Mec. Fluidos - Aplicações em Máquinas
6650 Lubrificação
6710 Transientes em Fluidos
6810 Téc. Experim. e Visualização Escoamento
7000 Termociências
7010 Termodinâmica
7110 Transp. de Calor - Convec. Monofásica
7120 Transp. de Calor - Convec. Bifásica
7130 Transp. de Calor - Condução
7140 Transp. de Calor - Radiação/Mod. Comb.
7150 Transp. de Calor - Dispositivos/Sistemas
7210 Termodinâmica dos Sólidos
7310 Transporte de Massa
7410 Combustão
7420 Combustão em Leito Fluidizado
7510 Acionadores e Dispositivos de Propulsão
8000 Geociências
8010 Micromeritics
8110 Meios Porosos
8210 Geomecânica
8310 Mecânica dos Abalos Sísmicos
8410 Hidrologia, Oceanografia, Meteorologia
9000 Energia e Meio Ambiente
9110 Combustíveis Fósseis
9120 Sistemas Nucleares - Fissão
9125 Sistemas Nucleares - Fusão
9130 Sistemas Geotérmicos
9140 Sistemas Solares
9150 Sistemas Eólicos
9160 Sistemas de Energia Oceânica
9210 Armazenamento de Energia
9220 Distribuição de Energia
9310 Mecânica dos Fluidos Ambiental
9410 Mecânica de Dispositivos de Armazenamento de Resíduo
10000 Biociências
10110 Biomecânica
10210 Ergonomia
10310 Reabilitação
10410 Mecânica nos Esportes

Áreas de Aplicação

Exemplo: um especialista em Mecânica dos Fluídos (família 6000) atuando na área de Turbulência (6520), deverá escolher a Área de Aplicação 350, se estiver trabalhando em Propulsão.

010 Acústica e Controle de Ruído
020 Aplicações em Biociências
030 CAD
040 CAM
050 Componentes de Máquinas
060 Controle Ambiental
070 Controle de Qualidade
080 Criogenia
090 Engenharia e Física de Reatores

100 Engenharia de Petróleo
110 Engenharia Oceanográfica
120 Equipamentos de Processos
130 Equipamentos Industriais
140 Fontes Alternativas de Energia
150 Forjamento
160 Fundição
170 Garantia de Qualidade
180 Indústria Têxtil e Tecnologia Correlata
190 Inspeção e Certificação

200 Instalações Industriais
210 Instrumentação
220 Lubrificação Industrial
230 Mancais e Rolamentos
240 Máquinas Ferramentas
250 Máquinas de Fluxo
260 Máquinas Motrizes
270 Mecânica Fina
280 Metalurgia Geral e Beneficiamento de Minério
290 Metrologia

300 Mineração e Metalurgia Extrativa
310 Óptica
320 Pontes e Barragens
330 Processos de Fabricação
340 Projeto de Estruturas
350 Propulsão
360 Prospecção e Propulsão
370 Servo Mecanismos e Controle
380 Siderurgia
390 Sistemas Hidráulicos

400 Sistemas Pneumáticos
410 Soldagem
420 Solicitações Acidentais - Efeitos de Vento, Sismo, Explosão, Fogo e Inundação
430 Tecnologia de Alimentos
440 Tecnologia Mineral
450 Transporte (excluído veículos)
460 Transmissão de Energia
470 Tratamento Térmico e Termoquímico
480 Tubulações Industriais e Nucleares
490 Usinas Hidrelétricas

500 Usinas Termoelétricas
510 Vácuo
520 Vasos de Pressão, Trocadores de Calor e Equipamentos Pesados
530 Veículos - Terrestres, Espaciais e Marítimos

Journal of the Brazilian Society of Mechanical Sciences

Information for Authors

SCOPE AND POLICY

- The purpose of the Journal of the Brazilian Society of Mechanical Sciences is to publish papers of permanent interest dealing with research, development and design related to science and technology in Mechanical Engineering, encompassing interfaces with Civil, Electrical, Chemical, Naval, Nuclear, Agricultural, Materials, Petroleum, Aerospace, Food, System Engineering, etc., as well as with Physics and Applied Mathematics.
- The Journal publishes Full-Length Papers, Review Papers and Letters to the Editor. Authors must agree not publish elsewhere a paper submitted to and accepted by the Journal. Exception can be made for papers previously published in proceedings of conferences. In this case it should be cited as a footnote on the title page. Copies of the conference referees reviews should be also included. Review articles should constitute a critical appraisal of published information.
- The decision of acceptance for publication lies with the Editors and is based on the recommendations of at least two ad hoc reviewers, and of the Editorial Board, if necessary.

SUBMISSION

- Manuscripts and all the correspondence should be sent to the Editor or, alternatively, to the appropriate Associate Editor.
- Four (4) copies of the manuscript are required. The author should submit the original figures, which will be returned if the paper is not accepted after the review process.
- Manuscripts should be submitted in English or Portuguese. Spanish will also be considered.
- A manuscript submitted for publication should be accompanied by a cover letter containing the full name(s) of author(s), mailing adresses, the author for contact, including phone and fax number, and, if the authors so wish, the names of up to five persons who could act as referees.

FORMAT

- Manuscripts should begin with the title, including the english title, the abstract and up to five key words. If the paper's language is not English, an extended summary of about 500 words should be included. The manuscript should not contain the author(s) name(s).
- In research papers, sufficient information should be provided in the text or by refering to papers in generally available Journals to permit the work to be repeated.
- Manuscripts should be typed double-spaced, on one side of the page, using A-4 sized paper, with 2 cm margins. The pages should be numbered and not to excess 24 pages, including tables and figures. The lead author of a RBCM paper which exceeds the standard length of pages will be assessed a excess page charge.
- All symbols should be defined in the text. A separate nomenclature section should list, in alphabetical order, the symbols used in the text and their definitions. The greek symbols follow the English symbols, and are followed by the subscripts and superscripts. Each dimensional symbol must have SI (Metric) units mentioned at the end. In addition, English units may be included parenthetically. Dimensionless groups and coefficients must be so indicated as dimensionless after their definition.
- Uncertainties should be specified for experimental and numerical results.

ILLUSTRATIONS AND TABLES

- Figures and Tables should be referred in consecutive arabic numerals. They should have a caption and be placed as close as possible to the text first reference.
- Line drawings should be prepared on tracing paper or vellum, using India ink; line work must be even and black. Laser print output is acceptable. The drawings with technical data/results should have a boundary on all four sides with scale indicators (tick marks) on all four sides. The legend for the data symbols should be put in the figure as well as labels for each curve wherever possible.
- Illustrations should not be larger than 12 x 17 cm. Lettering should be large enough to be clearly legible (1.5-2.0 mm).
- Photographs must be glossy prints.

REFERENCES

- References should be cited in the text by giving the last name of the author(s) and the year of publication of the reference: either "Recent work (Smith and Jones, 1985) ... or "Recently Smith and Jones (1985) With four or more names, use the form "Smith et al.(1985)" in the text. When two or more references would have the same text identification, distinguish them by appending "a", "b", etc., to the year of publication.
- Acceptable references include: journal articles,dissertations, published conference proceedings, numbered paper preprints from conferences, books, submitted articles if the journal is identified, and private communications.
- References should be listed in alphabetical order, according to the last name of the first author, at the end of paper. Some sample references follow:

Bordalo, S.N., Ferziger, J.H. and Kline, S.J., 1989, "The Development of Zonal Models for Turbulence", Proceedings, 10th ABCM - Mechanical Engineering Conference, Vol. I, Rio de Janeiro, Brazil, pp. 41-44.

Clark, J.A., 1986, Private Communication, University of Michigan, Ann Arbor, MI.

Coimbra, A.L., 1978, "Lessons of Continuum Mechanics", Editora Edgard Blucher Ltda, São Paulo, Brazil.

Kandlikar, S.G. and Shah, R.K., 1989, "Asymptotic Effectiveness - NTU Formulas for Multiphase Plate Heat Exchangers", ASME Journal of Heat Transfer, Vol. 111, pp. 314-321.

McCormak, R.W., 1988, "On the Development of Efficient Algorithms for Three Dimensional Fluid Flow", Journal of The Brazilian Society of Mechanical Sciences, Vol. 10, pp. 323-346.

Silva, L.H.M., 1988, "New Integral Formulation for Problems in Mechanics", (in portuguese), Ph.D Thesis, Federal University of Santa Catarina, Florianópolis, SC, Brazil.

Sparrow, E.M., 1980a, "Forced-Convection Heat Transfer in a Duct Having Spanwise-Periodic Rectangular Protuberances", Numerical Heat Transfer, Vol. 3, pp. 149-167.

Sparrow, E.M., 1980b, "Fluid-to-Fluid Conjugate Heat Transfer for a Vertical Pipe-Internal Forced Convection and External Natural Convection", ASME Journal of Heat Transfer, Vol. 102, pp. 402-407.

JOURNAL OF THE BRAZILIAN SOCIETY OF MECHANICAL SCIENCES
REVISTA BRASILEIRA DE CIÊNCIAS MECÂNICAS

VOL. XIX - Nr. 3 - SEPTEMBER 1997